August 2013

Density Functional Theory (DFT) Study on the Hydrolysis Behavior of Degradable Mg/Mg Alloys for Biomedical Applications

Marjan Nezafati
University of Wisconsin-Milwaukee

DENSITY FUNCTIONAL THEORY (DFT) STUDY ON THE HYDROLYSIS

BEHAVIOR OF DEGRADABLE MG/MG ALLOYS FOR BIOMEDICAL

APPLICATIONS

by

Marjan Nezafati

A Thesis Submitted in

Partial Fulfillment of the

Requirements for the Degree of

Master of Science

in Engineering

at

The University of Wisconsin-Milwaukee

August 2013

ABSTRACT

DENSITY FUNCTIONAL THEORY (DFT) STUDY ON THE HYDROLYSIS
BEHAVIOR OF DEGRADABLE MG/MG ALLOYS FOR BIOMEDICAL
APPLICATIONS

by

Marjan Nezafati

The University of Wisconsin-Milwaukee, 2013
Under the Supervision of Professor Chang-Soo Kim

Magnesium-based (Mg and/or Mg alloys) materials possess many advantageous
physicochemical/biological characteristics such as good biocompatibility and similarity
of the mechanical properties to the human bone tissue, which renders this material a
promising candidate for the biomedical and implant applications. One of the most
attractive features of Mg-based materials is the degradability in the physiological
environment. With the burst of research on the biodegradable materials for the healthcare
device applications, Mg and its alloys attracted a strong attention in the bioengineering
field in recent years. However, the major limitation of applying Mg-based materials to
biomedical applications is the fast degradation/corrosion rate with regards to the healing
process time-span. In the present thesis, an atomistic model employing the density-
functional theory (DFT) has been developed to study the hydrolysis process by
understanding the influences of commonly used alloying elements (zinc (Zn), calcium
(Ca), aluminum (Al), and yttrium (Y)) and the crystallographic orientation of the
dissolution surfaces (basal (0001), prism $(10\bar{1}0)$, and pyramidal $(\bar{1}01\bar{1})$ planes) on the
corrosion behavior. These parameters are known to strongly impact the initial hydrolysis

phenomena of Mg-based materials. To develop the atomistic computational model, we have implemented the Dmol3 software package in conjunction with PBE (Perdew, Burke and Ernzerhof) correlation energy functional in the GGA (generalized gradient approximation) scheme. Throughout the thesis, we performed three sets of calculations, i) surface energy, ii) dissolution potential, and iii) water adsorption computations, to examine the hydrolysis mechanism and the subsequent corrosion/degradation of Mg/Mg alloys. The total energy changes of various Mg-based systems in different conditions for these surface energies, dissolution behavior, and tendency of the system for adsorbing the water molecule were quantified. The results obtained from the atomistic model showed that these structural/compositional parameters (i.e., different types of alloying elements and surface planes) can considerably impact the stability of surfaces that are in contact with the corrosion media. The dissolution potential change computation predicted that Al can prevent the dissolution of Mg atoms from the surface of Mg-Al systems. In addition, it was found that the trend of water adsorption phenomena with different alloying elements/planes can be well-explained by the stability of corrosion surface.

To my family for their support

TABLE OF CONTENTS

LIST OF FIGURES

CHAPTER 2:

CHAPTER 4:

LIST OF TABLES

LIST OF ABBREVIATIONS

BZ_ Brillouin zone

DES_ Drug eluting stents

DFT_ Density functional theory

DFTD_ Density functional dispersion

E_ Elastic modulus

E_{Corr} _ Corrosion potential

FCC_ Face center cubic

GGA_ Generalized gradient approximation

HA_ Hydroxyapatite

HCP_ Hexagonal close packed

HF_ Hartree- Fock

KS_ Kohn and Sham

LDA_ Local density approximation

LSD_ Local spin density

MAO_ Micro-arc oxidation

MRI_ Magnetic resonance imaging

PBE_ Perdew- Burke- Ernzerhof

PCI_ Percutaneous coronary intervention

PES_ Potential energy surface

PLGA_ Poly lactide-co-glycolide

PCL_ Polycaprlactone

PLLA_ Poly-L lactic acid

SE_ Schrodinger equation

STS_ Stainless steels

TS_ Transition state

ACKNOWLEDGMENTS

I would like to express my deepest appreciation to all those who provided me the possibility to complete this work. I give a special gratitude to Dr Changsoo Kim whose stimulating suggestions, encouragement and support helped me to develop this project. Furthermore I would also like to acknowledge my committee members Dr. Abu- Zahra,

Dr. Chang and Dr. Church for their advices.

Lastly I would like to thank my family specially my brother and also my dearest friends

who have always supported me.

Chapter 1: Introduction

In this introductory chapter of thesis, an overview for the magnesium (Mg) and Mg alloys for the biomedical device applications, and the motivation and the objective of research project are provided.

1. Magnesium (Mg) alloys for biomedical applications: overview

There is a myriad number of material species that can be applied to develop medical devices, including various types of polymers, metals, and ceramics. Depending on the application and required properties, some materials possess more beneficial properties than the others. Some factors such as biocompatibility must be critically considered in the selection of materials for biomedical products, because the body reaction against some materials can cause irreparable problems for the patient. Chemical, physical, and mechanical properties, and even economical advantage should be considered, and the one that exhibit the optimum of these properties must be elaborately selected. However, the biocompatibility to physiological environment must be always confirmed prior to the application of biomaterials.

Among the three representative material types, i.e., metals, ceramics, and polymers, the metallic materials traditionally have been widely used in many biomedical applications due to their strong physical and mechanical properties. In the current thesis, we focus on the biomaterials made of metals/alloys. These biocompatible metallic materials include 316L stainless steels (STS), titanium (Ti) alloys, and cobalt-chromium (Co-Cr) alloys, but they do not degrade in the body fluid. On the other hand, there are some biodegradable metallic materials such as Mg and its alloys that spontaneously

disappear inside the human body. One of the most important trends in biomedical device technology is the incorporation of degradable materials to avoid complexities such as long-term adverse effects and secondary surgery, etc. By controlling the degradation/corrosion rate, these absorbable materials can be eliminated in a desired way after healing of injured sites. In addition, while most of the metallic materials have high strength that can consequently resist against the bone growth causing adverse problems in orthopedic applications, Mg alloys have similar elastic modulus (E) with natural bone material (the average E values of Mg alloys and natural bone are is 41-45 GPa and 3-20 GPa, respectively, which causes less damages. The density of Mg alloys (1.74-2 g/cm^3) is also close to natural bone density, which is 1.8-2.1g/cm^3 (1; 2; 3; 4). Therefore, Mg and Mg alloys are considered as one of the unique metals that feature the combination of biocompatibility, degradability, and mechanical strength for biomedical device applications.

Mg and its alloys have been used as medical device applications since the late 19th century. In 1878, Huse used an Mg wire ligature in radial artery and varicocele to stop bleeding vessels (5). First vessel connector made of Mg was tested on the femoral artery of dog in 1900 (6). The first use of Mg-based materials as an orthopedic implant was in 1907. Lambotte used a plate of pure Mg with gold (Au)-plated steel nails to secure a fracture involving the bones of the lower leg. The fast degradation (i.e., corrosion) of the implant, however, caused the failure of a complete support, and a considerable amount of gas amassed under the skin. In another trial in 1944, nine unsuccessful implantations were reported out of 34 cases for an Mg alloy containing a small amount of cadmium (Cd). The reasons for these failures were infection and also trapping of the gas

caused by mounted plaster cast. It was reported that these implants maintained their mechanical stability for 6-8 weeks and a complete desorption occurred after 10-12 months (4; 6; 7).

More recent studies on in vivo degradation of Mg alloys were performed comparing the corrosion tendency of different compositions. A trial by Witte et al. (8) investigated the impacts of AZ31 and AZ91 Mg alloys containing aluminum (Al) and zinc (Zn), WE43 alloys containing some rare earth (RE) elements such as neodymium (Nd), cerium (Ce), and dysprosium (Dy), and, also LAE442 alloys with a mixture of Ce, lanthanum (La), Nd, and praseodymium (Pr). The results showed a modest corrosion rate for alloys with RE elements.

One of the most important issues with Mg implants is the high rate of disruption, which is localized and unpredictable. It has been reported that high-purity Mg corrodes uniformly in vivo with an average rate of 0.1 g per 3-4 weeks. Of course, the total Mg corrosion depends on the exposed surface area of the material to the corrosive media. The type of tissue is also the important factor to determine the corrosion rate of the implanted material (6). In addition, the hydrogen (H_2) evolution causes the formation of gas packets that postpone the healing and cause to necrosis the tissue layers (9). It is thought that the research interest in Mg alloys for biomedical device applications is shifting toward investigating the effect of alloying elements on the formation of corrosion protective barrier in the interface of the alloy and the corrosive media (10).

2. Motivations

As addressed in the prior section, Mg and Mg alloys are promising candidate materials for medical products. This group of metals has shown reasonable mechanical

properties including high stiffness and strength, resistance to heat, and creeping and high fracture elongation, and it exhibits good vibration and shock absorption (2; 3). In general, another reason that makes Mg attractive is that, Mg has a high strength to weight ratio and high castability (2). In addition to all of these mechanical benefits, the primary advantage of using Mg alloys comes from that Mg^{+2} is a requisite ion in the human body system and it exists in a considerable amount in the body (Mg^{+2} is the fourth abundant cation found in the body. The human body usually contains about 35 grams Mg per 70Kg); a human adult is recommended to take 300-400 mg of Mg daily (2; 3). Mg is involved in many metabolic reactions and also physiological mechanisms as an essential material. Further, most importantly, Mg has a high biocompatibility, which is the vital property for implant materials (11). The presence of Mg in the body promotes the bone growth, and it shows non-toxic behavior and degrades in the body fluids (12). In addition, the extra amount of Mg has the possibility to be expelled through the urine after degradation.

Despite all of these advantages, the main problem with Mg is the elevated rate of corrosion (i.e., degradation), which strongly limits the use of Mg as a biomaterial. Mg would corrode at pH level of 7.4-7.6 and in the presence of high chloride environment of physiological system. Because the degradation rate of pure Mg is high, the mechanical properties will decrease before the healing process completes. The in vivo studies on corrosion resistance of Mg as medical implant material reported that the corrosion rate of 0.02 mm/y would be acceptable (13). However, it should be noted that the required degradation rate will vary depending on the location of implants. In some cases, fast degradation is needed while in others a modified rate of corrosion is demanded. In

general, the degradation rate should be coherent with the healing rate of the body tissue; for example, for medical devices intended to be used about 12 weeks in the physiological environment, the implant material must corrode after this period (11). Also, the amount of corrosion products released in the body should be low enough to be tolerated easily (14).

Mg is a metal that degrades very fast in biological media. The degradation rate must be controlled by different ways such as alloying or surface treatments, which will be comprehensively discussed in the next chapters. Note that, though there is a rich list of experimental efforts to improve the degradation rate of Mg alloys for the biomedical applications, theoretical understanding of the impacts of the types and contents of alloys, microstructures, and the degree of crystallinity on the Mg degradation behavior is still not clear.

3. Objective of Research

The ultimate goal of the current research is as follows.

• Understand the corrosion/degradation mechanisms of Mg and Mg alloys intended for biomedical applications.

Toward this ultimate goal, in the present thesis, we have developed an atomistic density-functional theory (DFT) computational model to study the impacts of alloying element on the corrosion behavior of Mg alloys. Computational modeling approach is frequently used to predict complicated physicochemical phenomena to decrease the expense of experimental measurements and to save the labors. Understanding of degradation/corrosion mechanism in the atomistic and/or molecular levels can be

accomplished through the development of atomistic computational model. In the current work, we focused majorly on the hydrolysis mechanism (i.e., one of the two primary degradation mechanisms of Mg materials) of Mg/Mg alloys to study the onset of the corrosion with various Mg alloy systems. It is expected that the obtained results can be used to understand and ameliorate the corrosion behavior of Mg alloys in the biological atmospheres.

The objective of the current work is, therefore, summarized as:

- Based on DFT, develop an atomistic computational model to quantitatively describe the initial degradation behavior of Mg/Mg alloys including the effects of alloying elements.

Using the developed DFT model, several physicochemical aspects, such as surface energies, water adsorption behaviors, and dissolution potentials, are studied and analyzed related to the degradation/corrosion mechanisms of Mg/Mg alloys. It is thought that the current work is one of the first attempts to understand the hydrolysis behavior of Mg/Mg alloy degradation for biomedical applications by using a DFT model. In following chapters, we will detail the background, computer model development, and results and discussion of the current work.

Chapter 2: Background

In this chapter, we will provide the detailed background and discuss some applications of Mg and Mg alloys in biomedical devices such as cardiovascular stents and bone replacement implants. Degradability, as the most important advantage of Mg based devices over permanent materials, is the main focus of this chapter. In this chapter, we will address the general introduction of Mg alloys, details of degradation mechanisms, factors to influence the degradation behavior, and recent efforts to improve degradation properties of Mg and/or Mg alloys.

1. Mg Alloys for Biomedical Applications

Proper implantation of external material in the body will require a variety of relevant physical, chemical, and mechanical properties; tissue-specific environment, the contact with blood, and the contact with different tissue-specific cell types should be adequately taken into account in the study of the material applicability in biomedical applications (15). In Table 2.1, some in-vivo physiological conditions that metallic implants should tolerate have been summarized. In addition to these conditions, implant metals should possess non-magnetic properties so that they can be tracked by magnetic resonance imaging MRI or X-ray imaging (1).

Table 2.1 Body physiological condition **(1)**

Condition	Parameters	Consequences
Body temperature	37º C	Effect the kinetic of the reaction
pH (16)		Even though the body fluids are buffered solutions,
Blood	7.15-7.35	close to the implantation site the pH can decrease to
Intercellular matrix	7.0	5.2

Cells	6.8	
Dissolved oxygen (17)		Corrosive environment
Arterial blood	100 mmHg	
Venous blood	40mmHg	
Intercellular matrix	2-40mmHg	
Chloride ion (16)		Corrosive environment
Serum	113mEq/l	
Interstitial fluid	117mEq/l	
Mechanical load (18)		Could lead to fracture or stress corrosion cracking
Cancellous bone	0-4MPa	
Cortical bone	0-40MPa	
Arterial wall	0.2-1MPa	
Myocardium	0-0.02MPa	
Muscle(Max)	40MPa	
Tendon(Max)	400MPa	
Load repetition (18)		Could lead to fatigue, wear and fretting
Myocardial	$5 \times 10^6 - 4 \times 10^7$ /year	
Contraction	$10^5 - 10^6$ /year	
Finger joint exercise	2×10^6 /year	
Ambulation		

Mg and/or Mg alloys have been advocated for several biomedical applications including cardiovascular stents and various forms of bone implants. Depending on required properties of different applications, different compositions can be applied to the Mg alloys. However, one of the major issues for development of biodegradable Mg alloys is the control of corrosion rate and the gap in understanding the relationship between alloy composition and the mechano-electrochemical behavior of the materials in vivo. Another limitation for these materials is that, the cytotoxicity standards developed for permanent materials (e.g., EN ISO Standards 10993:5) that can be applied to titanium (Ti) are not adequately applicable to Mg-based materials. Therefore, there is no established standard

for Mg alloys to evaluate their in vitro and in vivo corrosion behavior (19). In the following sub-sections, some examples of Mg alloys biomedical applications are introduced.

Table 2. 2 Application of different Mg alloys **(6)**

Magnesium (alloy)	Application	Human/animal model	year
Pure Mg	Wires as ligature	Humans	1878
High-purity Mg	Tubes(intestine, vessel, nerve connector), plates, arrows, wire, sheets, rods	Humans, guinea pigs, rabbits, dogs	1892-1905
Pure Mg	Mg cylinders as vessels connectors	Dogs	1903
High-purity Mg	Tubes, sheets and cylinder intestine connector	Humans, rabbits, dogs	1900-1905
Pure Mg (99.7%)	Rods, plates, screws	Humans	1906-1932
Metallic Mg	Ring-plates for anastomosis	Dogs	1910
Metallic Mg	Interamedullar pegs in bone	Rabbits	1913
Pure Mg mix. of eq. part: Mg/Al, Mg/Cd, Mg/Zn	Wires, clips as ligature, anastomosis	Dogs	1917
Pure Mg (99.99%), distilled in vacuum	Wires, strips, bands	Rabbits	1924
Pure Mg (99.8-99.9%)	Mg arrows	Humans, rats, cats	1925
Pure Mg	Mg arrows	Rabbits	1928
Dow metal: Mg-Al6-Zn3-Mn 0.2%-wt. Elektron Mg-Al 8%-wt.	Plates, bands, screws, pegs	Humans, dogs, rats, rabbits	1933-1937
Mg-Mn3%-wt., Mg-Al4-Mn 0.3%-wt.	Sheet, plate, band, screw, peg, wire	Human, dogs	1938
Elektron (alloy not specified)	Rods	Rabbits	1939
Mg-Cd	Plate, screws, rod-plate	Human	1948
Mg	Band, suture from woven Mg wires,	Human, rabbits	1940

	fusiform pins		
Mg-Al2%-wt. pure Mg	Wires for clotting aneurysms	Dogs	1951
Ind.-grade purity: Domal Mg (99.9%), T.I.H. Mg not reported lab-grade purity: "zone fondue " Mg, R69Mg, MgMn1.5%.wt, MgAl:GAZ8%,GAZ6%, GAZ3%	Pacemaker	Dogs	1975
Mg-Al2%.wt	Wires intravascular	Rats	1980
Pure Mg (99.8%)	Wires for hemangioma treatment	Rats, rabbits	1981
Pure Mg (99.8%)	Wires for hemangioma treatment	Humans	1981

1.1 Degradable stents

As a major medical device utilizing biodegradable materials, we introduce the cardiovascular stent applications in this section, as it is considered one of the most important medical devices due to the increased risk of cardiovascular disease in the modern era. The first coronary stent implantation was reported in 1985 (20). The use of stents has been widespread in recent years, and it has been constantly reported that the occurrence of some problems such as stent thrombosis (i.e., obstructing the blood vessel by blood clots formation on the surface of the stent) were reduced by using of thienopyridines an antiplatelet agent that prevents platelet activation and high pressure stent implantation (21).

Coronary stents are intended to replace complicated percutaneous coronary intervention (PCI) or angioplasty (i.e., non-surgical treatment for narrowed coronary arteries) by restricting the early and late recoil. When permanent (i.e., non-degradable)

stents are used, they may cause several clinical adverse effects including thrombogenicity (i.e., the tendency of material to produce thrombus during the contact with blood), permanent physical irritation, mismatches in mechanical behavior between stented and non-stented vessel areas, long term endothelial dysfunction (imbalance between products of blood vessel expansions), and chronic inflammatory local reactions. These permanent stents may increase the risk of injuries such as chronic inflammatory reaction or long-term endothelial dysfunction caused by continuous interaction between the stent and the surrounding tissue (22). In addition, in some cases (such as Lekton Magic stent), the stent is radiolucent that makes it difficult to be detected after implantation. To decrease the risk of embolism and blockage of the blood vessel by a detached intravascular mass, some sleeves on the delivery balloon at either side of the crimped stent are required (23).

To overcome these limitations, stents made of degradable materials were proposed. Such degradable stents have ability to offer more effective physiological repair, reconstitution of local vascular compliance, and they exhibit a temporary, limited, longitudinal, and radial strengthening effect (1; 24). Most importantly, the patients with permanent stent implantation often suffer from the long-term adverse effects. Comparing the permanent and bioabsorbable/biodegradable stents, there is indeed a need to design a bioabsorbable stent that disappears after healing (25).

The materials used for the components of these degradable stents must possess some necessary properties. For example, they must have enough radial strength during degradation period and also produce non-toxic and absorbable components during the corrosion (1). The local toxicity of biomaterials depends on the local concentration of elements over time (25). Further Colombo et al. (26) reported that a cardiovascular stent

endures a pressure of 1.0 to 1.4 MPa during its function. This pressure causes at least 20% deformation in the stent. Only limited types of materials meet these requirements. Some polymeric materials seem to be appropriate for this application, but polymeric materials have some issues including limited availability, and severe adaptation and/or deformation with radial forces. Another problem associated with these polymeric materials is their slow bioabsorption rate that may give rise to enhanced restenosis (25). For metallic materials, Fe and Mg provide degradation with a good adoption by the body without toxicity.

In Table 2.3, we display two examples of bioresorbable metallic stents from different manufacturers (25; 27; 28). As the table shows, peripheral Fe stent produced from iron tubes by Goodfellow Inc. (Hundington, UK). This stent is made of Fe with less than 0.5% of Al, Ca, Co, and other metallic impurities, and it has a design similar to the Saxx stent (CR Bard, Temp, AZ, USA). There are limited data available about this group of stents, but Waksman et al. (28) confirmed that the biocompatibility and mechanical properties of pure Fe seems to be reasonable but further studies are required for commercial application of these stents. Table 2.3 also shows the Mg stent (Biotronik, Erlangen, Germany) as an example of Mg based stents. The mechanical properties of Biotronik stent are similar to those of stainless steel stents, which provides enough support after implantation. It has been addressed that Biotronik also has acceptable biocompatibility (29).

Table 2.3 Bioabsorbable stent developments **(25; 27)**

Stent	Fe Based	Mg Based
Picture		
Composition	>99.5 mass% Fe	Mg Alloy/ Pimecrolimus
Features	Balloon expanding stent	Balloon expanding stent

It is understood that the recoil resulted from mechanical degradation (i.e., corrosion) is the primary cause of restenosis in applying Mg-based stents; therefore, the solution suggested for these problems is to increase the degradation time so that the stent can provide sufficient support to the vessel following intervention. The most recent development of these stents is in their alloying and design modifications to decrease the corrosion rate and to load an anti-proliferative drug on the stent surface that can slow down neointima formation (25). The coronary restenosis (i.e., re-narrowing of the blood vessel after implantation) after endovascular procedures is one of the issues in using stents. The neointimal hyperplasia (i.e., thickening of the neointima in the blood vessel during the reconstruction procedure) can be reduced to below 10% by using drug-eluting stents (DES) (30).

The stability and efficiency of the implanted stent are influenced by various material properties. Surface characteristics such as surface energies, surface textures, surface potentials, and the stability of the surface oxide layer impact the chance of occurring thrombosis and neointimal hyperplasia. The thrombogenicity of a material

surface can be increased with increasing surface energy. Experiments by Hehrlein et al. (31) on two different surface deposition methods, i.e., galvanization and ion implantation, showed higher thrombogenicity and neointimal hyperplasia for the galvanized stent, and the reason was explained by the existence of pores and cracks created during expansion. It is thought that the surface roughness of the stent is an important parameter in their clinical success. This should be concerned as new coatings are being developed, especially for drug elution, due to difference in surface texture and the bare metal (32).

1.2 Orthopedic applications

Metallic bone replacements and orthopedic implants are other common types of applications of Mg alloys. These implants are used to provide mechanical support during healing and fixation of broken bones. The benefit of using metallic materials compared to ceramics and polymeric materials is to have high mechanical strength and fracture toughness simultaneously (4). In 1878, Mg alloys were suggested as biomaterial in the shape of load-bearing implants for the first time (19). Permanent (non-degradable) materials such as stainless steels and titanium alloys were mostly used for these applications previously. To prevent osteopenia (i.e., decrease in the bone mineral density) resulted from long-term stress shielding, it is recommended to remove the material after recovery. A second surgery increases the risks and expenses for the patient. To avoid the health and financial costs, degradable materials such as Mg and Mg alloys were recommended (33). In addition, as addressed before, the mechanical properties of Mg and its alloys are similar to those of natural bone tissue material, which make Mg suitable for orthopedic applications (34). The orthopedic implant can be in different shapes such as plate, rod, or screw, as shown in Fig.2. 1.

Fig.2. 1 Mg based orthopedic implants **(35)**

The most essential requirement for a degradable implant is to provide sufficient mechanical support during healing. As the healing proceeds, the thickness of implant decreases and the bone grows, and due to this decrease in implant thickness, the mechanical stability drops. Considering this, selection of the initial thickness of the implants is critical. Higher thickness (larger volume) of materials will be needed in a highly corrosive media, but depending on the site of implantation, changing the size of implant thickness is not always possible (33). Fig.2.2 shows an image of implanted screw in the body illustrating the thread of the screw located in the hip and the head in contact with the soft tissue. In the figure, the hydroxide layer on the head is represented by white arrows which is thicker than the layer with the black arrow, emphasizing that the harder tissue around the thread slows down the corrosion rate while the material in contact with soft tissue corrode faster (36).
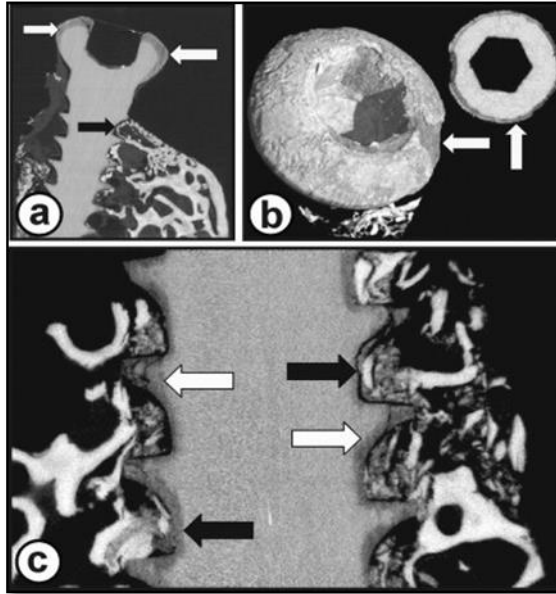
Fig.2. 2 different corrosion behavior for the screw depending on the implantation site **(36)**

1.3 Other applications

There are several other possibilities of using Mg-based materials in biomedical applications. Nerve guidance conduits (NGC) are another example. This device is effective for injuries with more than 5 mm gap to mechanically support the axonal spouting between nerves. Also it has been reported that during corrosion, ions such as Mg^{2+} and SO_4^{2-} form, and they result in the formation of $MgSO_4$, which can functions as a neuroprotective agent (37).

2. Degradation Mechanisms of Mg and Mg Alloys

As it was mentioned before, controlling the corrosion rate after implantation in the body is the most important and challenging issue with applying Mg as a biomaterial. Corrosion of Mg generally is described by the two mechanisms, i.e., hydrolysis and galvanic corrosion. In the following sub-sections, different types of corrosion mechanisms in Mg/Mg alloys are discussed.

2.1 Hydrolysis

Previous studies show that for all Mg alloys regardless of the corrosion types and compositions, the corrosion attack in aqueous environment can be described by the reaction given in Eq.2.1 (3; 38).

$$Mg + 2H_2O \rightarrow Mg\,(OH)_2 + H_2 \qquad\qquad Eq.2.1$$

The overall reaction consists of these partial reactions:

$$Mg \rightarrow Mg^{2+} + 2e^- \text{ (anodic reaction)} \qquad\qquad Eq.2.2$$
$$2H_2O + 2e^- \rightarrow H_2 + 2OH^- \text{ (cathodic reaction)} \qquad\qquad Eq.2.3$$
$$Mg^{2+} + 2OH^- \rightarrow Mg\,(OH)_2 \text{ (product formation)} \qquad\qquad Eq.2.4$$
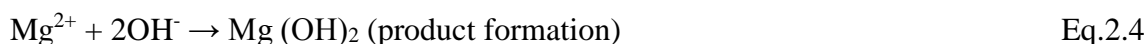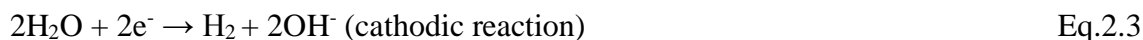
The overall reaction only considers the pure Mg systems (without any alloying elements). Song et al. (39) showed that during anodic dissolution on Mg-Al-Zn alloys, Mg is the main metallic element participating in the reaction, although the influence of alloying elements on the corrosion behavior of the alloy cannot be neglected. In general, therefore, the above four reactions are widely used to describe the hydrolysis corrosion process. However, when the thermodynamics of corrosion for Mg is considered, a difference between theoretical and actual standard potential values is observed, and this difference can be explained by the formation of a passive film consists of $Mg(OH)_2$ or MgO on the surface of the material. These films may contain some chlorides. When pH is greater than 9, a thick film of $Mg(OH)_2$ forms on top of the inner film and protects the metal from corrosion. The formation of this film can be described through Pourbaix diagram, the potential-pH diagram depicted in (40). This diagram shows that the region of immunity is much lower than the water stability region resulting in the evolution of

hydrogen (H_2) with dissolution in neutral and low pH conditions. In addition, it is seen that the passivation occurs by formation of Mg (OH) $_2$.
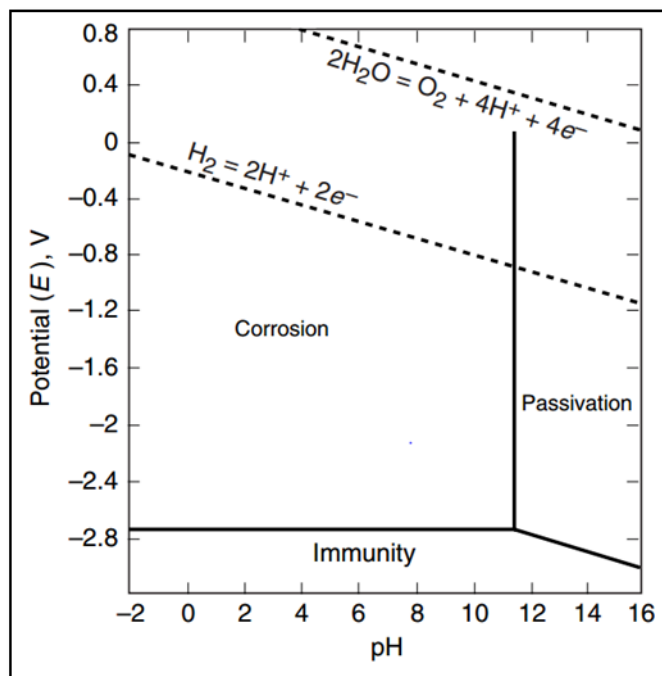
Fig.2. 3 Pourbaix potenial-pH diagram **(40)**

However, this diagram shown in Fig.2.3 is not complete due to lack of some other thermodynamic data for $Mg(OH)_2$ and Mg^+. To complement such deficiency, Perrault modified the diagram of Fig.2.3 and considered the formation of Mg^+ and some other components during the corrosion. The modified potential-pH diagram by Perrault's is shown in Fig.2.4 (41). Involving MgH_2 and Mg^+ in the mechanism, Perrault showed that a thermodynamic equilibrium does not occur for Mg electrode in contact with an aqueous solution. Fig.2.4 exhibits the potential and pH ranges where the different corrosion products are stable taking to account the formation of Mg^+ (42). Fig.2.3 (a) shows the Mg-H_2O system in the presence of H_2. As observed in Fig.2.4 (a), the formation of Mg^+ intermediate ion is apparent in a wide range of pH. The Immunity region is right below

the region of Mg$^+$ stability. From Fig.2.3 (b), when the hydrogen over potential is equal to 1 V, for the pH greater than 5 (point c), an equilibrium with existence of hydride is expected. In this case, the formation of a cathodic film is probable in the Mg electrode containing Mg(OH)$_2$ and MgH$_2$ (41). Eq.2.5-12 show relative reactions for each part of these two diagrams (3).
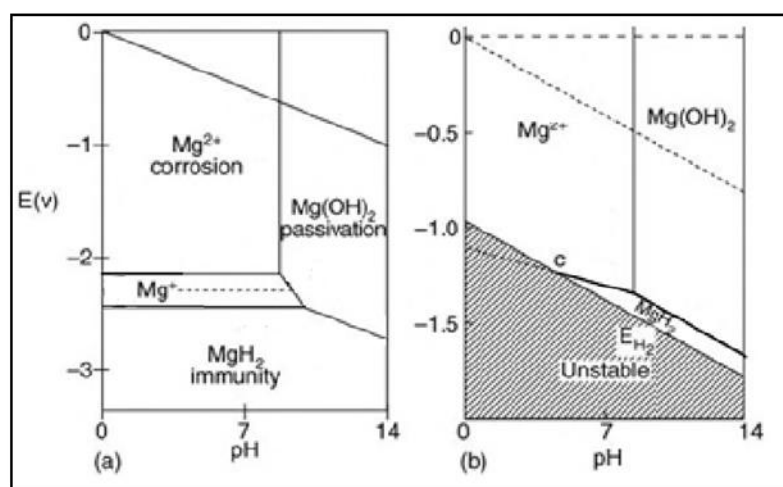
Fig.2. 4 (a) Perrault's Pourbaix diagram equilibrium in the Mg-H$_2$O system in the presence of H$_2$ molecules

(b) Range of stability for components containing Mg **(41)**

$2H^+ + 2e^- \rightarrow H_2$, E=-0.0592 pH   Eq.2. 5

$MgH_2 \rightarrow Mg^{2+} + H_2 + 2e^-$, E^0=-2.186V (NHE) (normal hydrogen electrode)   Eq.2. 6

$MgH_2 + 2OH^- \rightarrow Mg (OH)_2 + H_2 + 2e^-$, E^0=-2.512V (NHE)   Eq.2. 7

$Mg^{2+} + 2OH^- \rightarrow Mg (OH)_2$ Eq.2. 8

$Mg^+ \rightarrow Mg^{2+} + e^-$, E^0=-2.067V (NHE)   Eq.2. 9

$Mg^+ + 2OH^- \rightarrow Mg (OH)_2 + e^-$, E^0=-1.065V (NHE)   Eq.2. 10

$Mg^+ + 2OH^- \rightarrow Mg (OH)_2 + 2H^+ + e^-$, E0=-1.065V (NHE)   Eq.2. 11

$MgH_2 \rightarrow Mg^+ + H_2 + e^-$, E^0=-2.304V (NHE)   Eq.2. 12
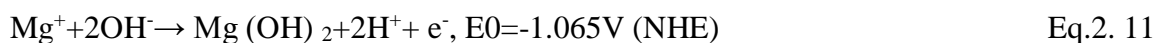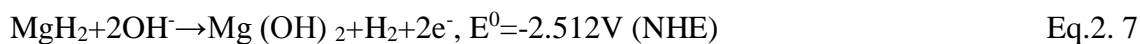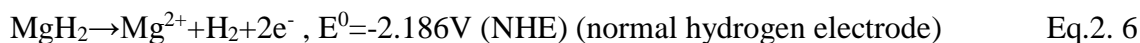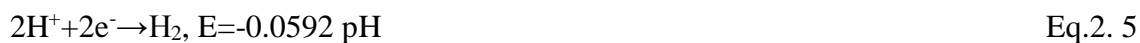
Experiments by Song et al. (43) on the anodic dissolution of Mg in $MgCl_2$ and $MgSO_4$ solutions showed that the intermediate ion Mg^+ can form in the primary step of the corrosion in the absence of a protective film. After the corrosion is developed, the intermediate species would react with the water and the products of this reaction are H_2 and Mg^{2+}. It should be noted that the intermediate ion Mg^+ forms only in the film free surfaces (3).
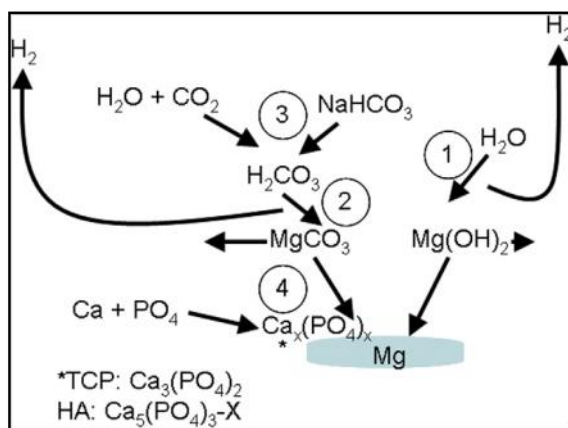
Fig.2. 5 Summary of some of the initial steps of corrosion under cell culture conditions (44)

The corrosion process in a biological environment occurs through several steps as illustrated in Fig.2.5, and it can be summarized as:

1. Release of Mg ions to the corrosion media and formation of $Mg(OH)_2$ caused by contact of the water molecules with Mg.

2. The Mg ions can interact with some species such as CO_2 in blood or form a deposition on the surface such as $MgCO_3$.

3. The corrosion slows down due to the formation of the passive layer on the surface. At this level, the interaction between amino acids and proteins takes place, which results in the formation of a less dense, second layer.

4. In the final step, the environment around the metallic Mg is shielded by two previously formed layers that would enable the cell to grow on the material. Biomineralization also occurs due to the insertion of Ca, and the possible products would be $Ca_3(PO_4)_2$ and $Ca5(PO_4)_3$. In the figure, X represents OH and/or Cl (44).

2.2 Micro-galvanic corrosion

Galvanic corrosion is another primary mechanism to account for the corrosion of metallic materials. It occurs when two dissimilar metals are coupled in an electrolyte. Similar condition applies in a micro-scale to the alloy when two different phases with different corrosion resistances coexist and one of them corrodes preferentially to another. As an example, because metals with low hydrogen overvoltage (e.g., Ni, Fe, and Cu) create efficient cathodic sites for Mg, they can easily cause galvanic corrosion. On the other hand, metals with high hydrogen overvoltage (e.g., Al, Zn) are relatively less damaging with reference to the degree of galvanic corrosion. This galvanic corrosion is influenced by several parameters; high conductivity of media, large potential difference between anode and cathode, large area ratio of cathode to anode and small distance from anode to cathode are the parameters enhancing the rate and degree of galvanic corrosion (3).

Song et al. (39) showed that the α-matrix (Mg-rich solid solution) in the absence of β-phase ($Mg_{17}Al_{12}$), initially undergoes a uniform oxidation and then after a few minutes the uniform corrosion is altered to pitting corrosion. Fig.2.6 illustrates schematically how micro and macro galvanic corrosion take place in Mg alloys. In Fig.2.6 (a) shows that the connection of an external metal with a higher potential forms a

galvanic cell and the potential difference between two metals would cause a galvanic effect. Fig.2.6 (b) describes an example of a micro-galvanic corrosion. In this case, the precipitated secondary phases play the role of the cathode and the Mg in the α-phase oxidizes as the anode of the galvanic cell (13).
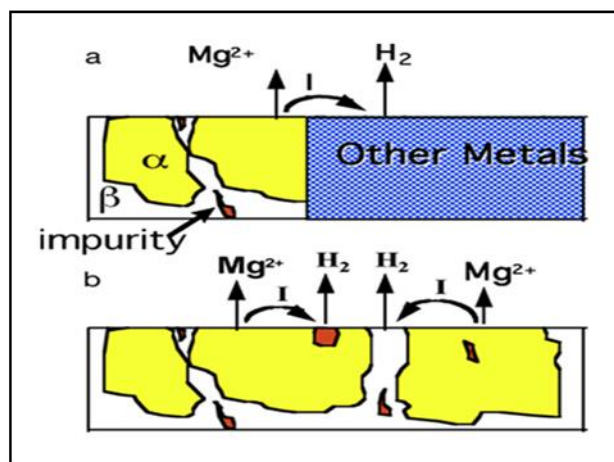
Fig. 2. 6 (a) Macro-galvanic corrosion, and (b) Micro-galvanic corrosion **(13)**

As mentioned earlier, the second phases form due to the presence of different alloying elements. These phases ordinarily have higher corrosion resistance compared to pure Mg (38). Table2.4 summarizes the corrosion potential of the intermetallic compounds existing in Mg alloys. From the table, it is clearly seen that the pure Mg has an anodic role and the seconadary phases are the cathode. Among these compounds, $Mg_{17}Al_{12}$ (β) phase is the most frequently observed secondary phase that accelerates the corrosion rate by serving strong cathodic areas (45).

Table2.4 Corrosion potential of Mg and common secondary phases containing Mg after 2 hours in deaerated 5% NaCl solution saturated with Mg (OH)$_2$ (pH equal to 10.5) **(38)**

Metal	E_{corr}, V_{SCE}
Mg	-1.65

Mg$_2$Si	-1.65
Al$_6$Mn	-1.52
Al$_4$Mn	-1.45
Al8Mn5	-1.25
Mg$_{17}$Al$_{12}$ (β)	-1.20
Al$_8$Mn$_5$ (Fe)	-1.20
Beta-Mn	-1.17
Al$_4$MM	-1.15
Al$_6$Mn(Fe)	-1.10
Al$_6$(MnFe)	-1.00
Al$_3$Fe(Mn)	-0.95
Al$_3$Fe	-1.74

In an overall view, the corrosion behavior of the Mg alloy is strongly dependent upon the composition of the alloy. The chart presented in Fig.2.8 shows the corrosion rate and corrosion type for different Mg alloys (9). In the chart, the symbol (G) stands for the general corrosion, (P) describes the pitting corrosion, and (X) refers to extremely localized corrosion, respectively. The detailed effect of different alloying elements will be discussed in this chapter, section 3.1.
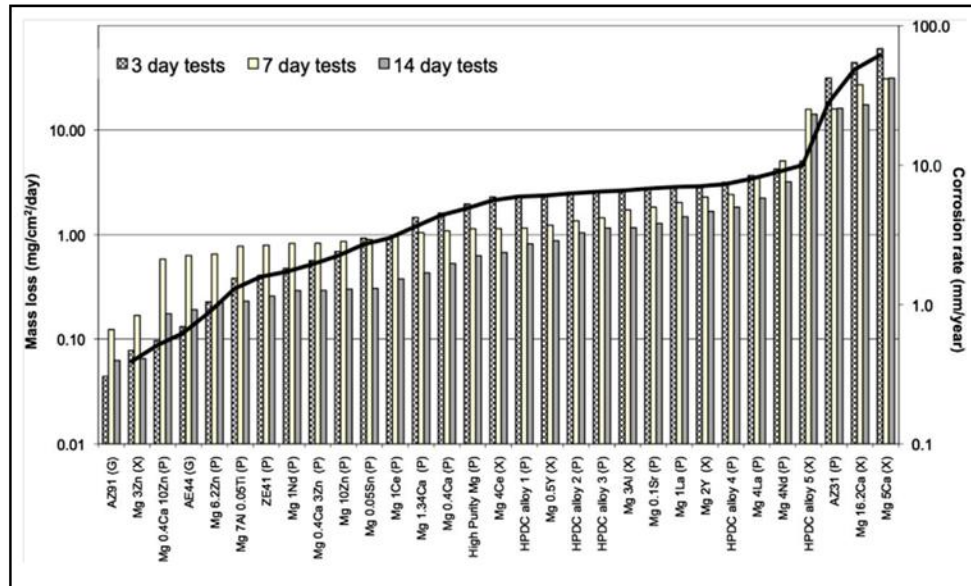
Fig.2. 7 Experimentally determined corrosion rate for Mg alloys at the temperature of 37˚C in Minimum

Essential Medium (13)

2.3 Negative difference effect (NDE)

During its corrosion process, Mg shows a strange behavior known as negative difference effect (NDE). NDE is described by an extremely high H_2 evolution rate with the applied potential. On the contrary, for most of metals, H_2 evolution decreases with increasing the applied potential. In this process, the current density increases in several orders of magnitude by a small differentiation of the potential above the threshold potential (3; 38; 46; 47; 48). Fig.2.9 presents the relationship between the potential and the current for corrosion of Mg. The solid lines in Fig.2.9 represent the cathodic and anodic partial reactions, I_c and I_a, respectively. It is assumed that the both cathodic and anodic parts obey the Tafel kinetic given in Eq.2.13.

$$i = nFk\exp\left(\pm\propto F\frac{\Delta V}{RT}\right)$$

Eq.2. 13

where n is the number of electrons involved in the reaction, F is the Faraday constant overpotential, k is the rate constant of the electrode reaction, α is the charge transfer coefficient, R is the universal gas constant, T is the absolute temperature and i is the current density. And, the plus and minus signs in the equation represent the anodic and cathodic reactions, respectively,

The corrosion rate for anode increases and the corrosion rate of the cathode decreases by increasing the current density in normal condition of corrosion for typical metals such as Fe, Zn, and etc. However, the behavior of Mg described by the potential difference graph in (49) Fig.2.9 shows an opposite trend. Dash lines in Fig.2.9 denoted by I_{Mg} and I_H indicate the Mg dissolution and H_2 evolution, respectively. For an applied potential of E_{app}, the hydrogen corrosion rate is given by $I_{H,m}$ and the corrosion rate of Mg is represented by $I_{mg,m}$. The value of Δ is negative for Mg corrosion, where $\Delta = I_0 - I_{H,m}$ and I_0 is the spontaneous H_2 evolution rate (HER) at the corrosion potential. NDE is a polarization phenomenon that occurs when $\Delta < 0$. But, this definition has some deficiencies; it does not cover HER behavior when the external applied current is cathodic. If the HER in cathodic region is always higher than their corresponding anodic HER, most of the normal electrodes with "positive difference effect" will show NDE (3; 38). To eliminate the defects of previous definition, a new definition has been suggested to describe NDE in both anodic and cathodic regions as $\Delta = (I_0 - I_c) \, I \, / \left| I \right|$ (3).
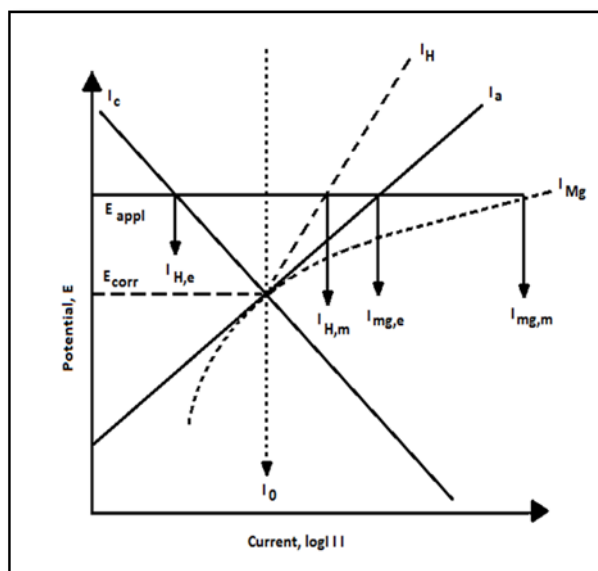
Fig.2.8 negative difference effects for Mg corrosion **(49)**

3. Factors impacting degradation of Mg alloys

3.1 Alloying materials

There are many other elements that can be added in Mg alloys. According to ASTM nomenclature principles of Mg alloys, 22 alloying elements have been used to enhance the properties of pure Mg, including Al, Bi, Cu, Cd, Fe, Th, Sr, Zr, Li, Mn, Ni, Pb, Ag, Cr, Si, Sn, Gd, Y, Ca, Sb, Zn and RE. These elements are generally categorized into 5 groups. The first group contains Fe, Cu, Ni, and Co elements that cause the high corrosion rate even in low concentrations. The second group elements are toxic metals including Pb, Cd, and Th. The third group belongs to nutrient elements in human such as Ca, Mn, Zn, Sn, Cr, and Si. The next group contains nutrient elements found in plants and animal including Al, Li, Ag, Sr, and Zr, and the last group contains other elements such as Sb, Gd, Y, and RE (rare-earth elements). If the additional element has a detrimental effect on Mg corrosion, it is considered as an impurity. Most of the impurities have a slight effect under specific concentration considering their tolerance limit. At impurity

concentrations above tolerance limit, the corrosion rate would accelerate. The graph in Fig.2.9 (3) shows the tolerance level of different alloying elements when they are combined with Mg.
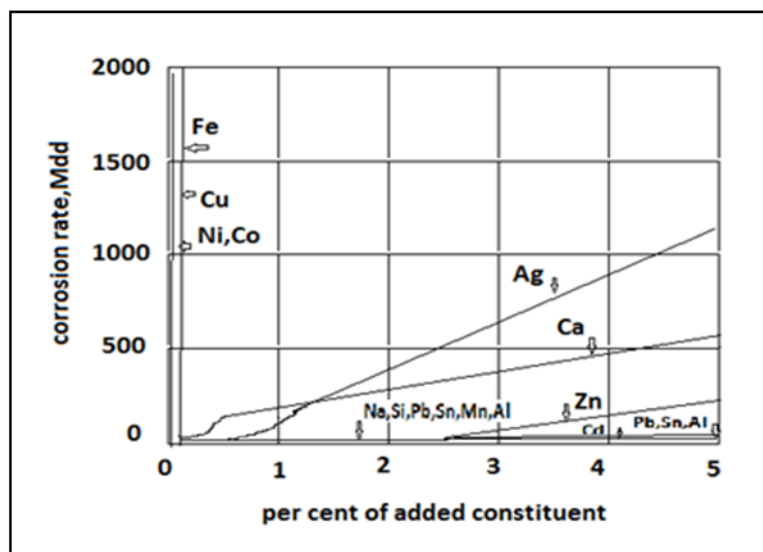
Fig.2. 9 Corrosion rate for binary alloys exposed during 16 weeks to immersion in 3% NaCl (30 s in solution; 2 min in air). Where Mdd is milli gram deci meter square per day (**3**)

3.1.1 Nutrient elements in human (Ca, Mn, and Zn)

Ca is one of the required elements in the body and is essential for chemical signaling within cells. Mg-Ca alloy density is close to bone which facilitates the incorporation of calcium to the bone. An Mg-Ca alloy with the composition of Mg-0.5Ca has been reported to be an acceptable alloy for biomedical implants due to the high corrosion resistance and low degradation rate (12; 13; 50). Hassel et al. (51) showed the improvement of mechanical and corrosion properties of Mg in NaCl solution by adding Ca. On the other hand, by addition of Ca, Mg_2Ca intermetallic phase formation is more probable. Kirkland et al. (52) reported that the newly formed phase is a stronger anode and more electrochemically active compared to α-Mg because of its chemistry, crystal

structure, and also the Pilling-Bedworth ratio (PBR) ≤1. Here, PBR is the volume of the elementary cell of the metal oxide divided by the volume of the elementary cell of the corresponding metal. This ratio basically indicates the tendency of the metal to passivate. If this ratio is less than one the coating layer is too thin that breaks and provides no protection. The values for a and c in hexagonal Mg are 0.32093 and 0.52107, respectively, whilst Mg_2Ca has a and c value of 0.623 and 1.012, respectively (greater than those of pure Mg). Ca increases the corrosion resistance of alloy but by passing the tolerance level the amount of Mg_2Ca phase increases so the anodic surface area ratio on the Mg matrix augments and the H_2 evolution rate increases, which can lead to a higher corrosion rate. Therefore, proper control of Mg_2Ca phase distribution will lead to improvement of corrosion resistance of the alloy (53; 54).

Mn is one of the tolerable elements in the body and it shows no toxic effect except after extreme exposure. The highest tolerable value for avoiding toxicity for Mn is 1.8±0.5 µM/L in binary Mg alloys, but other alloying elements such as Zn can aid to overcome this limitation; for instance, it was observed that an Mg-Mn-Zn alloy shows an acceptable behavior in vivo (12). Mn also demonstrates positive effect on the mechanical property of the alloy by refining the grains. The saltwater corrosion resistance of the alloy is possible by the support of the protective brucite layer with formation of manganese oxide (MgO) and its incorporation with $Mg(OH)_2$. Mn also eliminates the destructive effect of Fe and Ni; in these cases the Fe-Mn ratio is more critical rather than the absolute value of the Mg content. The tolerable value for this ratio is 0.032.

Zn in smaller amounts is tolerable and it increases the strength of the alloy due to solid solution strengthening (55; 56). Zn also decreases the harmful effect of Fe and Ni

on the corrosion of the alloy, but at the same time the hydroxide layer of this element is not stable (57). The most effective influence of zinc in the alloys modification is due to incorporation with other alloying elements such as Al, Ca and P. For concentrations higher than 2 wt% in combination with Al, it was found that Zn can lead to an embrittlement of the alloy (58). Formation of a protective layer of $Zn_3(PO_4)_2$ has been reported in the case of resolving of Mg-Zn-Mn alloy in Hank's solution (59; 60; 61). The combination of Ca and Zn modifies the degradation behavior of the alloy, but in presence of $Ca_3(PO_4)_2$ for higher than 2 wt% Zn, there is a chance for cytotoxicity (62).

3.1.2 Nutrient elements found in plants and animal (Al)

One of the most common alloying elements added to Mg is Al. There are numerous documentations to show that addition of Al to Mg alloys increases their corrosion resistance (49; 63; 64). The stabilization of the protective $Mg(OH)_2$ layer in the media containing Cl^- has been reported (8). The decrease in the corrosion rate is considerably rapid by addition of up to 4% Al and the rate would decrease modestly between 4 to 9%. Al is partially soluble in Mg alloys and also precipitates as $Mg_{17}Al_{12}$ in the grain boundaries forming a lamellar or a continuous structure. In some cases, other precipitations such as $Mg_2Al_3(Mg_5Al_8)$ form. $Mg_{17}Al_{12}$ is more corrosion resistant than pure Mg. Although the $Mg(OH)_2$ and MgO layers on the surface of Mg alloy are protective, they can be easily cracked. $Mg_{17}Al_{12}$ acts as a corrosion barrier and improves the corrosion behavior of the alloy compared to the pure Mg.

On the other hand, Al can cause a negative effect on the corrosion resistance of Mg alloy by decreasing the tolerance limit of Fe from 170 wt- ppm to 20 wt-ppm. This trend in the Fe tolerance limit appears to be consistent with the formation of a passive Fe-

Mn-Al intermetallic phase during solidification. In addition, Al can have different influences depending on its concentration. The Al-rich zones adjusted to the precipitates are more corrosion resistant than Al-depleted bulk matrix (3; 48). If the alloy contains both Al and Mn, the formation of intermetallic components can extract Fe from the alloy and modify the corrosion behavior of the alloy. Song et al. (49) observed a decrease in the corrosion rate of the alloys with Al concentration in the range of 2-9 wt% in 5% NaCl solution media. The most important concern in application of Mg alloys containing Al is the poor biocompatibility of Al. the combination of Al^{+3} ions with inorganic phosphates causes lack of PO_4^{3-} in the body and leads to neurological disorders such as dementia, senile dementia and Alzheimer's disease (12; 65). Due to the toxic effect of Al, elimination of this element in implants biomaterials has been sometimes suggested (10).

3.1.3 Other elements (Sb, Gd, Y, and RE)

Compounds of Sb, Gd, Y, and RE elements with Mg have not been mentioned to be essential for the body, and also they are not found in the body. RE ions form pores in the red blood cells even in low concentration and cause hemolytic effect which is the rupture of red blood cells and release of their contented to the surrounding area. In addition, RE elements can produce colloid in the blood but the colloidal components can be eliminated from the body by the phagocytic cells of liver and spleen. This group of alloying elements is not highly toxic and had been used to cure cancer and synovitis, still more studies are needed to discover the degree of toxicity of these elements (12). Y is one of the most frequently used RE alloying elements. Y increases the value of the corrosion potential (E_{corr}) and decreases the value of anodic current density, hence, it causes the reduction in the corrosion rate of the alloy. In the solid solution case, the

passive film thickness increases which seem to be more protective. Presence of Y in the surface composition causes the formation of a more protective layer (13; 50; 66). Although the formation of intermetallic phases such as $Mg_{24}Y_5$ increases the chance of micro-galvanic and filform corrosion (i.e., a form of corrosion that occurs under the coating and appears as a thread-like filament), but there are evidences that the surface film protection is high and the film retards the corrosion for a range of concentration of Y up to 3-7 wt%. Additionally, the formation of RE oxide film is known to be responsible for the passivation in alloys containing Y and Nd, also, Y has standard electrochemical potential equal to that of Mg (-2.372 V for both) (13; 66; 67; 68).

3.2 Microstructures

Previous experiments on Mg alloys emphasize on the effect of microstructure on corrosion behavior of Mg alloys (69; 70). Formation of secondary phases, grain size, and crystallographic orientation are features that influence the corrosion behavior of the alloy.

3.2.1 Formation of the secondary phases

When intermetallic compounds are adhesive enough to isolate the surface from corrosive media and if they have higher cathodic reaction activity compared with the matrix, they can function as corrosion barrier and protect the alloy surface against the corrosive media. On the other hand, formation of secondary phases increases the chance of galvanic corrosion. The protection by the surface film is strongly dependent on its homogeneity. If the protective film breaks down, due to the contact of the surface with the destructive media the corrosion accelerates. The second phase in the shape of small particles provides cathodic sites and increases the corrosion rate; for instance, even though the β-phase in AZ91 ($Mg_{17}Al_{12}$) has small size and homogeneous distribution, the

combination of solid solution matrix and secondary phase creates micro-galvanic cells and speeds up the corrosion (69; 71). In general, the presence of the second phases causes the acceleration of the corrosion rate in most of the Mg alloys such as AZ91 and ZE41. The formation of micro-galvanic cells between the matrix and intermetallic phases such as $Mg_{12}Ce$, $Mg_{12}La$ and Mg_3Nd is responsible for this high rate (11).

3.2.2 Grain size effect

Grain boundaries are defects in crystal structure. Due to the high concentration of dislocations (imperfection in crystal structure) and because of their high internal energy, grain boundaries often offer low corrosion resistance. Segregation of the alloying element in the grain depending on the alloying element type, and the solidification rate decreases the stability of the grain boundary. However, as for the segregation, the small grain structure is preferred because of less composition gradient. The combination of grain refining process and secondary phases (β phase) formation in some cases provides continuous and homogeneous precipitates around the finer solid solution of Mg and alloying elements (α phase). This may protects the alloy from pitting corrosion (13; 71). In general, to increase the corrosion resistance in the alloy due to the presence of grain boundaries and also to avoid great composition gradient inside the grain, the size of the grains should be optimized.

3.2.3 Crystallographic orientation

It is well understood that the crystallographic orientation and therefore the packing density of atoms on the surface is important to describe the corrosion behavior (72); a loosely packed crystallographic plane shows higher tendency for dissolution of metallic ions compare to densely packed planes. This variation in corrosion behavior is

due to the difference in atomic coordination and binding energies in unlike crystallographic orientations (73). For both of pure Mg or Mg alloys, the atomic density appears to have influence on the surface energy and accordingly on the corrosion rate of the alloy. Figs.2.11 (a) and (b) show the crystallographic orientation and Fig. 2.11 (c) shows corrosion behavior of AZ31 Mg alloy with two different surface orientations (70). From figures, it is clearly observed that the basal plane (0001) (i.e., crystallographic orientation of the rolled surface (RS)) is much more resistant to the corrosive media than the other surface comprised of the combination of $(10\bar{1}0)$ and $(2\bar{1}\bar{1}0)$ planes (70). The result of experimental work by Liu et al. (73) emphasizes on the stability of the basal plane by measuring the depth of corrosion in different grains. Calculating the surface energies of these planes clarified that surfaces with lower surface energy are more stable (70; 73; 74).
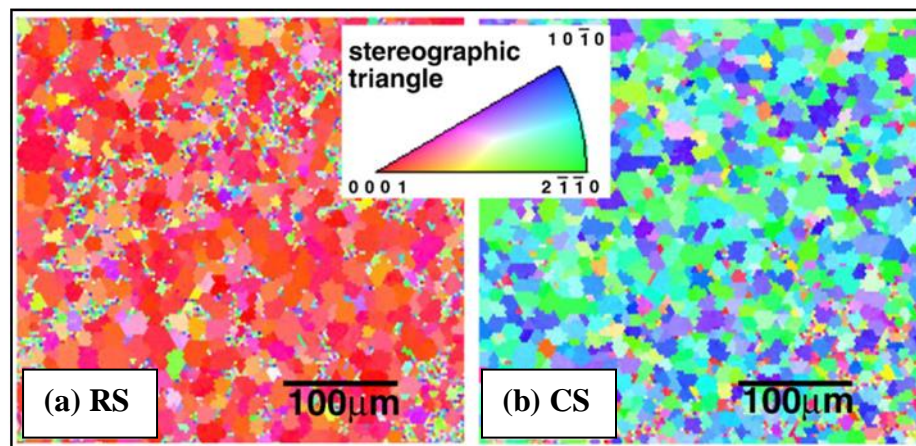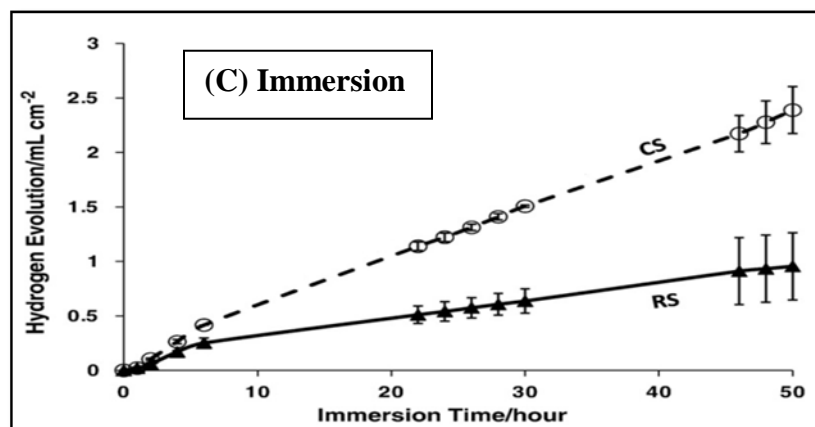
Fig.2.10 Crystallographic orientation and immersion corrosion behavior (a) rolling surface with dominant crystallographic orientation of (0001) basal plane, (b) cross-section surface with crystallographic orientation of $(10\bar{1}0)$ and $(2\bar{1}\bar{1}0)$, and (c) immersion result **(70)**

3.3 Corrosion media

Different environmental conditions affect the corrosion rate of the Mg alloys. For example, Mg is nearly resistant to alkaline media. For pHs higher than 10.5 that corresponds to saturated $Mg(OH)_2$, the corrosion resistant $Mg(OH)_2$ barrier protects the alloy from corrosion. NaCl solution attacks Mg alloys has a slow rate (13; 39), while Cl^- ions encourage corrosion in an aqueous neutral environment and even may break the thin protective hydroxide layer. The corrosion attack by SO_4^{2-} , NO_3^- , or PO_4^{3-}ions seems to be less destructive compared to Cl^- (43; 75). Some ions existing in the media such as fluoride have beneficial influence on the corrosion behavior of the Mg and provide corrosion resistant surface film on the alloy (34; 76). The dominant physiological characteristics of the body have been summarized in Table 2.1.

Even though the pH of the body fluid including blood, intercellular liquid, and cells' liquid are about 7, and they show buffered solution behavior, in some cases, the pH of the sites close to the implants drops to acidic pH (16). Oteyaka et al. (77), reported that in the

presence of Cl⁻ ions, the corrosion potential stops from increasing after 30 min and becomes constant caused by several phenomena called constant process of breakdown and repair of the passivation. In these phenomena the Cl⁻ ions interrupt the formation of the protective film and delay the production of the surface layer. In addition, the dissolved oxygen in the blood makes the media more corrosive (17).

4. Efforts to Improve Corrosion of Mg Alloys

In this section, we will introduce the recent efforts exerted to pure Mg to improve its corrosion behavior. Corrosion properties of the most common Mg alloys will be discussed and different forms of microstructure modifications will be suggested in this section.

4.1 Alloying

As it was mentioned in section 3.1, adding some alloying elements to pure Mg improves the mechanical properties and corrosion behavior. These effects will be discussed for commercially used Mg alloys in this subsection.

4.1.1 WE43

WE43 with composition of 4% Y, 2.25% Nd, and 0.15%Zr, and remaining Mg offers high mechanical properties combined with slow corrosion rate and low density. Although intermetallic components such as $Mg_{24}Y_5$ and $Mg_{12}Nd$ can function as cathodic sites and cause galvanic corrosion (12), Kalb et al. (78) reported that the chromatography of free Mg^{2+} shows less ion release for WE43 compared to pure Mg, which verifies the high corrosion resistance of this alloy. Due to its reasonable corrosion rate and high

biocompatibility, WE43 is applicable in biomedical devices such as bone fracture implants and Coronary stent (2; 11; 79).

4.1.2 AZ91

AZ91 has the composition of 90.04% Mg, 9.0% Al, 0.7% Zn, 0.04% Si, 0.22% Mn, and less than 0.02% of Cu, Fe, and Be. Even though the existence of intermetallic components in the composition of the alloy increases the risk of galvanic corrosion, depending on the size and distribution of the secondary phase particles, the galvanic corrosion may be avoided. For instance, AZ91 containing Al and Zn as main alloying elements provide tolerable corrosion resistance due to the formation of $Mg_{17}Al_{12}$ and Mg_4Al_3 in the shape of a non-porous protective layer (12; 39; 80). In vivo tests by Witte et al. (8) on AZ91 clarified that this alloy shows biocompatibility in the body. They suggested, although AZ91 contains 9% Al, but due to the low corrosion rate of the alloy, the existing amount of Al for a short length of time does not exceed the tolerance level.

4.1.3 AZ31

AZ31 has 96.23% Mg, 2.51% Al, 1.03% Zn, 0.2% Mn, 0.02 Si and less than 0.01% Cu, Ni and Fe. The low amount of alloying elements in AZ31 causes acceptable biocompatibility of this alloy. AZ31 is a good candidate for bone implant and biodegradable stent applications. In addition, due to small amount of secondary phases distributed in the structure, the alloy is considered almost single phase and shows negligible micro-galvanic coupling. Although formation of intermetallic corrosion barrier is not expected in AZ31, the hydroxide layer is still probable to form and protect the alloy (70; 81; 82).

4.1.4 MgCa0.8

Investigating corrosion behavior of Mg with different amount of Ca shows that the alloy containing 0.6-0.8 wt% Ca has the highest corrosion resistance (83; 84). MgCa0.8 is a binary alloy of Mg with high biocompatibility, reasonable degradation rate and acceptable mechanical behavior. This alloy is candidate for implant applications such as bone screws and cardiovascular stent (84; 85). In addition to improving corrosion behavior, Ca causes grain refinement and enhancement of mechanical behavior of the alloy.

4.2 Microstructure

Altering the microstructure of the alloy, minimizing the grain boundaries and phase separations, or reproducing the porous structure of the natural bone to increase the similarity with the body tissue might be effective to get better mechanical or corrosion behavior from the alloy.

4.2.1 Porous structure

Different methods have been used to produce porous structure in Mg alloy including powder metallurgy (86), casting in negative salt pattern molding process (87), thermal decomposition of pine wood using unidirection solidification (88), and supersaturating the melt with hydrogen and unidirectional upward solidification (89). The experimental work by Capek et al. (86) on Mg based porous materials for scaffold application produced by powder metallurgy showed lower corrosion resistance due to more contact area as a result of penetration of the corrosive media into the porous structure. The advantage of this structure is its close mechanical properties to the bone material. In another experiment, Witte et al. (87) used moistened NaCl to generate

negative salt pattern and casted the AZ91D Mg alloy. Fig.2.12 shows a scheme of their work. In part (a) of this image, the porous structure of the implant is obvious, the red rectangular in the right knee is the inserted cylinder implanted into the bonehole via a special pestle which has been shown in part (b). The Mg scaffold and the autologous bone implant site have been shown in part (c) and (d) of Fig.2.12, respectively. They concluded even with fast degradation rate of the porous Mg alloy, the material seems to be appropriate for biomedical applications due to elimination of the hydrogen evolution and no report for clinical infection. In another experiment by Gu et al. (89), the porous implants produced by the saturated melt with hydrogen and unidirectional solidification of pure Mg showed slower corrosion rate and better mechanical behavior compared to the compact pure Mg.
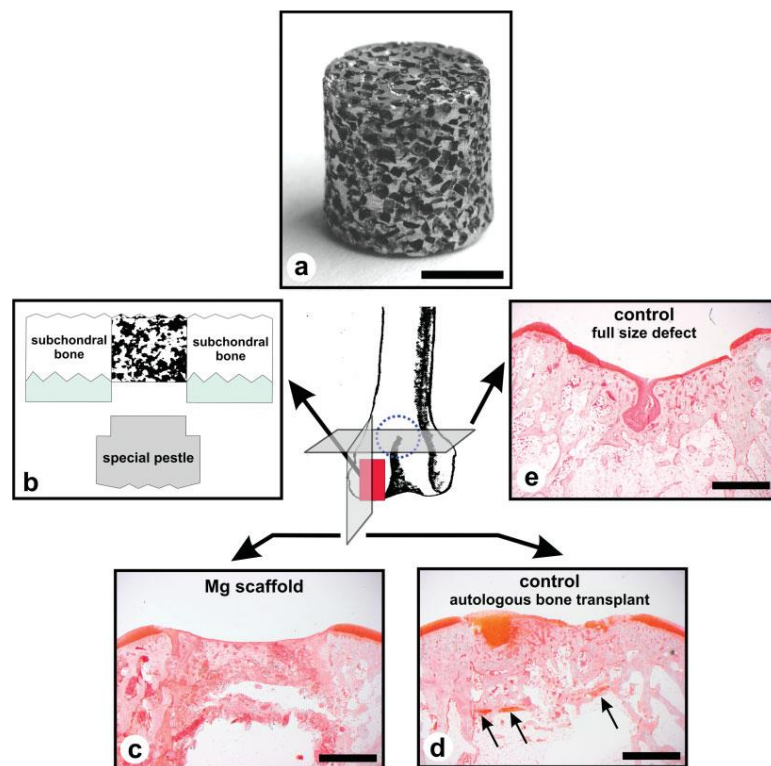
Fig.2. 11 Cylandrical implants of AZ91D magnesium alloy **(87)**.

4.2.2 Amorphous microstructure

Another way to ameliorate the corrosion behavior of Mg alloys is avoiding composition gradient and phase variation by formation of single phase amorphous structure (i.e., metallic glass). The amorphous structure of the alloy has a metastable phase with some tendency to crystallize. Rapid solidification is a method to produce a non-crystalline structure. The alloy with amorphous structure dissolves faster at the beginning of the corrosion process due to its higher corrosion activity, but as the anodic polarization potential increases, there is only one phase existing in the structure, therefore, galvanic corrosion is not expected to occur (90; 91).

Metallic glasses containing alloying elements such as Zn, Ca and Pd, show acceptable biocompatibility and moderated corrosion rate. Zberg et al. (90) reported that increasing the amount of Zn content of the $Mg_{60+x}Zn_{35-x}Ca_5$ where ($0 \leq x \leq 7$) improves corrosion protection of the biodegradable material by formation of a protective corrosion barrier. Gu et al. (91) emphasized on the promising behavior of Mg-Zn-Ca bulk metallic glasses in biomedical applications due to the single phase structure produced after solidification.

4.2.3 Coating and surface modification

Preventing the direct contact of the corrosive media with the metal and applying some barrier between the media and the implant may be effective to delay the initiation of the corrosion reaction (92). The first method of coating, known as chemical protection, is provided by removing the primary non protective oxide layer and producing a protective layer with strong chemical bonding between the surface film and the alloy. Etching the surface with some acids such as phosphoric acid causes the adhesive

corrosion resistance layer of $Mg_3(PO_4)_2$ to form. This film stops the corrosion reaction from progressing (93). Fluoride treatment is another useful method that takes advantage of formation of homogenous MgF_2 film. This layer is dense and does not dissolve in water easily (94). Other methods categorized as chemical processing include electron beam treatment, anodizing coating, and ion implantation (92).

Coating with organic polymers such as poly (lactide-co-glycolide) (PLGA) (95), polycaprolactone (PCL) (96), or apatite coatings, including hydroxyapatite (HA, $Ca_{10}(PO_4)_6(OH)_2$) (97) does not involve chemical bounding between the coating and the surface of the alloy. This group of coatings is known as physical coating. Combining physical and chemical methods has been recommended to gain a higher protection on the alloy. For instance, the protective behavior for combination of micro-arc oxidation (MAO) and poly-L lactic acid (PLLA) has been shown on WE42 alloy (92).

Chapter 3: Density Functional Theory (DFT) Model Development

Computations using the density-functional theory (DFT) have become a common tool for many-body problems in atomic and molecular solid state applications. It is used to calculate properties such as equilibrium geometries, activation energies, and reaction energies. In this chapter, we will briefly discuss the general theory and background about DFT. We will also define some important concepts in DFT. Then some previous examples of DFT calculations related to the current thesis will be introduced.

1. Density functional theories (DFT)

1.1 DFT: general

DFT is a method in quantum mechanical modeling that studies the behavior of the material by solving the Schrödinger equation (SE) and finding the ground state of the system. Ground state is defined as the state in which the system has the lowest possible energy. On the other hand, the excited state of a quantum mechanical system is any state that has energy greater than the ground state. This DFT theory applies to many-body systems and considers the interaction between electrons and nuclei (98). The ground state can be found by solving SE, which is a partial differential equation that describes the behavior of the quantum state of a physical system. This equation may be independent or dependent on time, and it has the general form of Eq.3.1.

$$\nabla^2 \psi + \frac{2m}{\hbar^2}(E - V)\psi = 0 \qquad \text{Eq.3. 1}$$

This function describes the position of electron. In Eq.3.1, ψ is the wave function that represents the behavior of the electron. In time dependent case, ψ is replaced by Ψ which is a function of time and position. And, m is the (rest) mass of electron, the reduce Planck constant $\hbar = \frac{h}{2\pi}$, where h is the Planck constant (6.626×10^{-34} m²kg/s), and E is the total energy that provides the allowed values for the energy of the system, which is typically defined as the sum of kinetic (T) and potential energy (V) as Eq.3.2.

$$E = T + V$$
<div align="right">Eq.3. 2</div>

In any atomistic and/or molecular type of computations, the background theory can be based on ab initio or semiempirical potentials. The ab initio type of methods does not use any extrapolated and/or interpolated data, or any empirical data. However, the semiempirical approach fits the approximation function calculations with the data from the system. Therefore, they are only accurate if the fitted data is similar to the exact data for the system. The pure ab initio DFT approximation is suitable for public users that use commercial packages but not ideal for software developers because it does not provide enough space for creativity. On the other hand, the semiempirical methods offer enough room for "anything that works", but, at the same time, the accuracy decreases by using these approximations. In general, all the practical computations are partly ab initio and partly empirical. In the following section, different ab initio and semiempirical DFT functionals and their applications will be discussed (99).

1.2 Parameters for DFT

For better understanding of DFT, some fundamental parameters need to be identified. In this section, we briefly introduce some required concepts, general principles of DFT, and some developments on the proposed solutions for SE.

Hartree-Fock (HF) approximation is a primitive solution for many-electron theory. This calculation finds the best spin orbitals to the ground state that minimize the electronic energy (100). On the other hand, Born-Oppenheimer approximation suggests that to solve the SE the Hamiltonian ($\hat{H}$) and the total energy (E) of the system must be identical as in Eq.3.3, where Ψ_i represents the eigenvalues or eigenfunctions for the system (i.e., values of energy that provide certain solution for the SE).

$$\hat{H}\,\psi_i = E\psi_i \qquad\qquad \text{Eq. 3. 3}$$

Following the quantum mechanical researches since 1920's, Hohenberg and Kohn (101) developed their model to describe the behavior and distribution of electrons in the material. They suggested that the mutual Coulomb repulsion and external potential, $v(r)$, provide a Hamiltonian which is the operator for the energy of the system in quantum mechanics and is defined as a functional containing the kinetic energy (T), the interaction with the external potential which is the interaction of electrons with the nuclei (V), and the electron-electron interaction (*U)* as it is given in Eqs.3.4-8.

$$H \equiv T + V + U \qquad\qquad \text{Eq.3. 4}$$

$$T \equiv \frac{1}{2}\int \nabla\psi^*(r)\nabla\psi(r)\,dr \qquad\qquad \text{Eq.3. 5}$$

$$V \equiv \int v(r)\psi^*(r)\psi(r)\,dr \qquad\qquad \text{Eq.3. 6}$$

$$U \equiv \frac{1}{2}\int \frac{1}{|r-r'|}\psi^*(r)\psi^*(r')\psi(r')\psi(r)drdr' \hspace{3cm} \text{Eq.3. 7}$$

$$n(r) \equiv (\Psi, \psi^*(r)\psi(r)\Psi) \hspace{3cm} \text{Eq.3. 8}$$

Where r is the particle's coordinate, and $\psi(r)$ is the state of the electron and $\psi(r)^*$ is the complex conjugate of $\psi(r)$, and they are related through Eq.3.9, showing the probability of finding a particle in space is one.

$$\int \psi\psi^* d\tau = \int |\psi|^2 d\tau = 1 \hspace{3cm} \text{Eq.3. 9}$$

Hohenberg and Kohn reported that the potential $\upsilon(r)$ is a unique functional of $n(r)$, which is the density of the ground state (Ψ). They also defined the universal functional, $F[n]$, valid for any number of particles and any external potential. As a result the energy functional can be expressed as Eq.3.10 given below. They proposed that the correct $n(r)$ gives the ground state energy $E_{\upsilon}[n]$ as given in Eq.3.10 (98; 101).

$$E_{\upsilon}[n] \equiv \int \upsilon(r)n(r)dr + F[n] \hspace{3cm} \text{Eq.3. 10}$$

1.2.1 Exchange-correlation function

In developing the Hohenberg and Kohn theory, two types of electron density approximations, i.e., localized and generalized, were considered (102; 103). Based on the theory proposed by Kohn and Sham (KS) (104) in real systems such as atoms and molecules in solid states, the electronic density is not uniform. The modern KS DFT defines self-consistent equations. These equations apply to the condition when orbitals have densities identical to the densities of real system (105), which is the basis of

developing the idea of local density approximation (LDA) (105). It defines the ground state energy of nonuniform electron gas considering a static potential $\upsilon(\mathbf{r})$ as Eq.3.11.

$$E = \int \upsilon(\mathbf{r})n(\mathbf{r})d\mathbf{r} + \frac{1}{2}\int\int \frac{n(\mathbf{r})n(\mathbf{r}')}{|\mathbf{r}-\mathbf{r}'|} d\mathbf{r}d\mathbf{r}' + G[n] \qquad\qquad \text{Eq.3. 11}$$

In this equation, $G(n)$ stands for a universal functional of the density. KS defined a local approximation for $G(n)$ which directs to the Hartree's method considering the effects of exchange and correlation energy for an interacting system. In this approximation, the energy depends only on the density at the specific point where the functional has been defined. Considering the exchange correlation energy (E_{XC}) containing the real space cutoff (E_X) and the reciprocal space cutoff (E_C), $E_{XC} = E_X + E_C$, as a function of spin densities, $n_\uparrow$ (density of electrons with upward spin) , $n_\downarrow$ (density of electrons with downward spin), $n = n_\uparrow + n_\downarrow$, the exchange local spin density $(E_{XC}^{LSD}[n_\uparrow, n_\downarrow])$ functional can be approximated (i.e., local spin approximation, LSA).

$$E_{XC}^{LSD}[n_\uparrow, n_\downarrow] = \int d^3 r n \epsilon_{XC}^{unif}(n_\uparrow, n_\downarrow) \qquad\qquad \text{Eq.3. 12}$$

Eq.3.12 describes the corresponding function for $E_{XC}^{LSD}[n_\uparrow, n_\downarrow]$, where $\epsilon_{XC}^{unif}(n_\uparrow, n_\downarrow)$ stands for the exchange correlation energy per particle of a uniform electron gas. However, it was found that the existing LDA underestimates the exchange energy of the system, therefore, aiming to improve the deficiencies of LDA theory such as unsuccessful respond to rapid changes in electrons density, generalized gradient approximation (GGA) was suggested by Perdew et al (103; 106).

Because this new functional depends on electron density and its gradient, it provides a better solution for the case of inhomogeneous electron densities. In general, it

is known that GGA can improve the computational accuracies for total energies, atomization energies, structural energy differences, and energy barriers compared to LDA. Eq.3.13 defines the exchange correlation energy for the GGA (103).

$$E_{XC}^{GGA}[n_\uparrow, n_\downarrow] = \int d^3 r f(n_\uparrow, n_\downarrow, \nabla n_\uparrow \nabla n_\downarrow)$$
Eq.3. 13

To simplify the practical calculation, $\epsilon_{XC}^{unif}(n_\uparrow, n_\downarrow)$ and f (i.e., the free energy of interacting electrons) must be well-defined. Although GGA in general offer more accurate approximations, there are some limitations in it, therefore, a development of newer functional was required for more complicated molecules and metals, when $f(n_\uparrow, n_\downarrow, 0,0) \neq n\epsilon_{XC}^{unif}(n_\uparrow, n_\downarrow)$. Perdew and Wang (107) suggested the PW91 analytical function to improve GGA calculations. PW91 keeps the positives features of LSD while applying to some inhomogeneity effects. However, there are still some limitations for PW91 including long complicated derivation that is dependent on mathematical details to be carefully defined, and the relationship between parameters are not clearly defined. The functional proposed by Perdew, Burke and Ernzerhof (PBE) correlation energy functional was the next functional proposed by Perdew et al. (103) to simplify the GGA. It is known that this PBE functional is efficient and it produces accurate results for structural properties, but it is less accurate for estimating other properties (101; 103; 108). Further development of the functional resulted in other exchange correlation energies such as B3LYP, meta-GGA, and B2PLYP. B3LYP is a hybrid DFT functional that combines GGA with HF. Meta-GGA is a recent version of the GGA functional to contain advanced higher derivatives. B2PLYP by Grimme et al. (109; 110) is considered as the most advanced functional that can improve the energetic

and spectroscopic properties. B2PLYP has not yet been employed in any commercialized DFT package, but it is claimed that it has a high potential to be applied for a wide range of material systems.

1.2.2 k-points

The calculation of ground state based on KS theory needs some simplifications and approximations. The system with electron-electron interactions can be mapped to non interacting electron system, and an infinite solid bulk may be considered periodic. Consequently, SE can be solved for finite number of electrons. It has been suggested that by choosing appropriate supercell the Bloch's theory may be applied even to aperiodic structures such as surfaces. A supercell in DFT consist of the vectors that show the cell volume that can be repeated in three dimensions and produces the required crystal structure and also the atom positions in the cell (111). Bloch's theorem states that the electrons in a periodic system have the work function as Eq.3.14.

$$\Psi_{kn} = U_{kn} \exp\left(ik.r\right)$$

Eq.3. 14

Where U_{kn} a periodic function and k is is the k-point that refers to all the values in the first Brillouin zone. The first Brillouin zone is the primitive cell in the reciprocal space, and it is given by the volume surrounded by the surfaces with the same distance from one element point of the lattice and its neighbors. The reciprocal space in solid-state physics stands for the array of reciprocal lattices. Fig.3.1 shows the first Brillouin zone of hcp structure (112). Table 3.1 shows the critical points of this structure in reciprocal space.
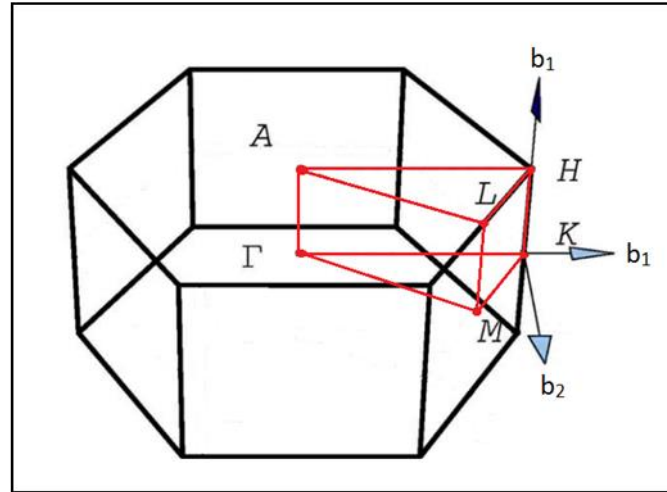
Fig.3. 1First Brillouin zone of hexagonal **(112)**

Table 3.1 Hexagonal critical parameters

Sign	Defenition
A	Center of a hexagonal face
Γ	Center of the crystal momentum space
H	Corner point
K	Middle of an edge joining two rectangular faces
L	Middle of an edge joining a hexagonal and rectangular face
M	Center of a rectangular face
b_1, b_2, b_3	Reciprocal vectors

In crystallography, reciprocal lattice is the encoded version of the real space by Fourier transforms. Eqs.3.15-17 represent the relationship between the real space unit vectors, a_1, a_2, a_3, and the reciprocal space unit vectors, b_1, b_2, and b_3. By using the relationships in Eqs.3.15-17, it is possible to convert the real space lattice vector ($\vec{R}$) defined in Eq.3.18 to reciprocal space lattice vector ($\vec{k}$) in Eq.3.19.

$$\vec{b_1} = 2\pi \frac{a_2 \times a_3}{a_1 \cdot (a_2 \times a_3)} \qquad \text{Eq.3. 15}$$

$$\vec{b_2} = 2\pi \frac{a_3 \times a_1}{a_2 \cdot (a_3 \times a_1)} \qquad \text{Eq.3. 16}$$

$$\vec{b_3} = 2\pi \frac{a_1 \times a_2}{a_1 \cdot (a_1 \times a_2)} \qquad \text{Eq.3. 17}$$

Knowing all these definitions now we are able to define k-point. The k-points appear in the wave function of the first Brillouin zone and are defined in Eq.3.19.

$$\vec{k} = x_1 b_1 + x_2 b_2 + x_3 b_3 \qquad \vec{R} = n_1 a_1 + n_2 a_2 + n_3 a_3$$

Eq.3. 18

$$\vec{k} = x_1 b_1 + x_2 b_2 + x_3 b_3 \qquad \text{Eq.3. 19}$$

Where n and x are the integers to produce the linear combination vectors in real and reciprocal space, respectively. In DFT, the k-point of each system must be carefully selected before performing the computation. As the number of k-point increases, it is in general known that the computational accuracy increases whereas the computation time increases. The total energy of different structures can be an important parameter to select the k-point of each system. To compare the stability of different systems, their total energies are computed and compared. In calculating the total energies of systems with same crystallographic structures and similar lattice parameters, it is important to apply consistent k-point values because the computed results can show some variations depending on the selected k-points (113).

1.2.3 Pseudo-potentials

In quantum mechanics, especially in DFT, considering all of the electrons in the computational system by calculating all available Coulombic potential is very expensive. When the pseudo-potential calculations are employed, we assume that the change in the surrounding atoms does not affect states of the nuclei and the core electrons (i.e., the electrons other than the valance electrons). Since valance electrons are the only electrons participating in the bonding, the pseudo-potential calculation solves the DFT equations based on the modified potential. Although the pseudo-potential does not give the exact result compared with the Coulomb potential, it is generally accepted that the plane wave basis set can represent both the pseudo-potentials and pseudo-wave functions. Also, there are fewer numbers of electronic states that can simplify the solid state calculations (114; 115).

1.3 DFT calculations

In any DFT calculations for polycrystalline materials, the crystal structure of the system must be identified. Then, the crystal structure needs to be optimized so as to be adapted to the computational condition of interest. Further calculations and studies on the system are based on this optimized crystal structure with the calculated total energy. Some of these important DFT calculation aspects related to the current thesis are discussed in this section.

1.3.1 Crystal structures

Empirical observations show that the size of atom is important for determining the crystal structure. The electronic configurations of material systems are important to determine the structural chemistry. Crystal structure is a unique arrangement of atoms. A

polycrystalline material is made up of repeating the unit cell which is the smallest set of atoms that represents the properties of bulk material. Stacking the unit cell in three dimensions generates a supercell. A supercell is the most frequently used unit of material for geometry optimization and other DFT calculations. Using DFT calculations, we can predict which crystal structure is more stable compared to the others. Thus, identification of the stable unit cell structure for polycrystals is considered as the first step in many DFT computations (98).

1.3.2 Total energy

DFT calculations can solve the many electron wave functions that can produce many useful results. The most useful information in our work calculated from DFT is the total energy of the system. The total energy is the energy value which is used in the ground state calculations and it is calculated from Eq.3.20 including the kinetic energy $T[n]$, the Hartree energy (electron-electron repulsion) $E^H[n]$, the exchange and correlation energy $E^{xc}[n]$, and the potential energy $V[n]$ (116). Hohenberg and Kohn (101) reported that the Hamiltonian and the total energy of the system both are unique functional of ground state electron density, n(r). This means that if there are two different external potentials for the ground state electron density, they are identical. As a result, if n(r) is known for the system, the external potential, the H, and also the total energy of the system of interacting electrons are known. In other words, by calculating the total energy, the system is sufficiently defined.

$$E[n] = T[n] + E^H[n] + E^{xc}[n] + V[n]$$
<div style="text-align: right">Eq.3. 20</div>

1.3.3 Geometry optimization

To calculate the ground state energy and to find the equilibrium configuration of the atoms, the structure of the system needs to be optimized. Geometry optimization is the scheme to find the most stable state of the system and other types of system energies such as the transition state (TS) energy and the reaction energy. Potential energy surfaces (PES) are one of the methods to represent the equilibrium state of the system based on the Born-Oppenheimer approximation. This approximation separates the motion of electrons from the nuclei and considers the nuclei to have fixed position due to its negligible movement compared to the electrons. It is known that solving the electronic structure of the system gives the corresponding PES. An example of PES has been presented in Fig.3.2 (18). As it was mentioned, the PES graph shows the stability of the materials based on their energy and their configurations and shapes. The vertical axis in most of PES graphs (Fig. 3. 2) shows the energy of the system while other axis represent different aspects of geometry such as distances and angles between system parts. Using this graph, the energy of the reaction can be calculated by finding the energy difference between the product and the reactant points (117).
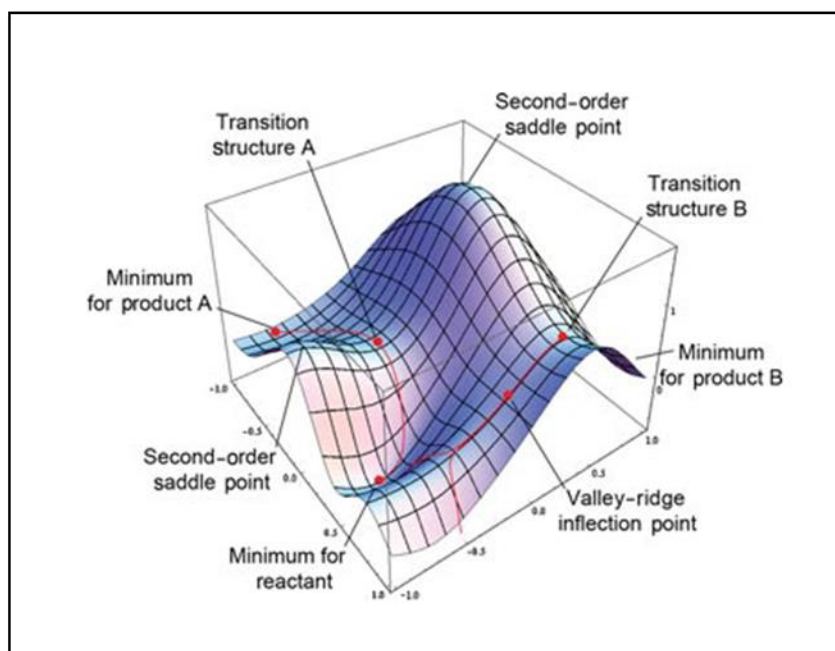
Fig.3. 2 PES with minima, transition structure and reaction paths **(117)**

Although DFT is a suitable theory to study the behavior of material, it has some limitations. One of the most important disadvantages of DFT is that, this theory is not able to describe the dispersion interactions (i.e., a long range energy contribution from the interaction of dipoles). To solve this problem, different approaches have been proposed, such as finding a truly non-local exchange-correlation functional or applying the symmetry-adapted perturbation theory to find the intermolecular potential. All these methods are known as density functional theory dispersion (DFTD) (118).

2. DFT computations: examples

In this section, some examples of DFT calculations that are closely related to the corrosion/degradation problems addresses in the current thesis will be presented. The DFT topic examples contained here include the interaction of polar molecules with metallic surfaces, the adsorption of water molecule on different surfaces, the dissolution

of surface atoms in presence of alloying elements, and the formation of hydroxides in Mg alloys.

2.1 Adsorption Models

Several DFT investigations have been conducted to study the interaction of a molecule with polycrystalline solid surface and the corresponding adsorption energy (119; 120; 121). Here, we introduce two examples by Akinaga et al. (119) and Zhao et al. (121; 122).

2.1.1 Akinaga et al., 2001 (119)

Akinaga et al. (119) studied the adsorption of SCH_3 on the (111) surfaces of noble metals. It is well-known that SCH_3 is a polar molecule, and the system was modeled to study the interaction of polar molecules and the adsorption behavior of metallic surfaces. The authors considered a variety of molecule configurations with the surface and concluded that the position of the SCH_3 molecule and the orientation of the molecule in addition to the nature of the surface atoms influence the adsorption energy.

In their work, the (111) surface was chosen due to the highest stability compared to other planes in the face centered cubic (fcc) crystal structure. The adsorption energy for Cu, Ag, and Au showed that the most inert element (Au) has the lowest adsorption energy, and the Ag and Cu have higher adsorption energy, respectively. The highest adsorption energy for Cu clarified that the low atomic radius of Cu causes more interaction of these atoms with the SCH_3 molecule.

2.1.2 Zhao et al., 2011 and 2012 (121; 122)

The DFT calculation done by Zhao et al. (121; 122) concentrated on the interaction of the water molecule and the TiO_2 surface. Interaction with the (101) TiO_2 surface was discussed in this work as the primary habitual orientation for the anatase TiO_2 phase. The first concern of the research was to find the most stable state for water adsorption configuration. The PES was calculated considering the oxygen atom coordinate. Fig.3.3 shows the computed and fitted results for the relative energies with the molecular and dissociative adsorptions.
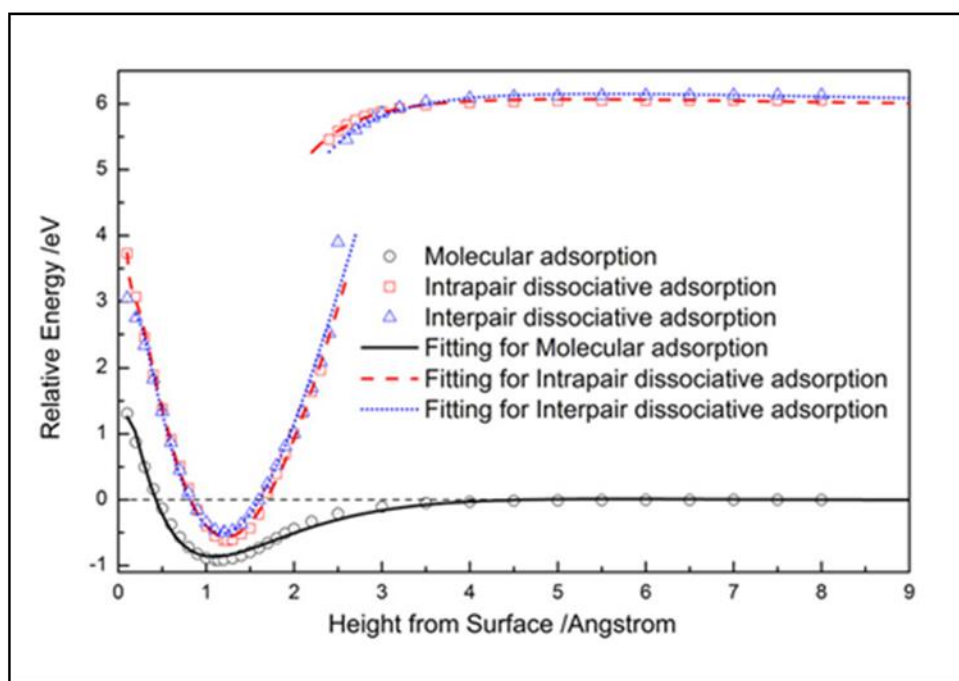
Fig.3. 3 The interaction of the water molecule with the TiO2 surface **(121)**.

In another work (122), the authors concentrated on the transition state and the energy path during the adsorption and dissociation processes of water molecule. Fig.3.4 shows the energy changes with different states for the system during the reaction. In the figure, SS stands for the separate state, IS denotes the initial state, TS is the transition

state, and FS stands for final state, respectively. The result of their work illuminated that the bridge site between Ti and O is the most stable site for molecular adsorption. In addition to (101) surface, they studied the behavior of other surfaces such as (103), (100), and (001), and for each case, they found the activation energy as the barrier required to overcome the transition state.
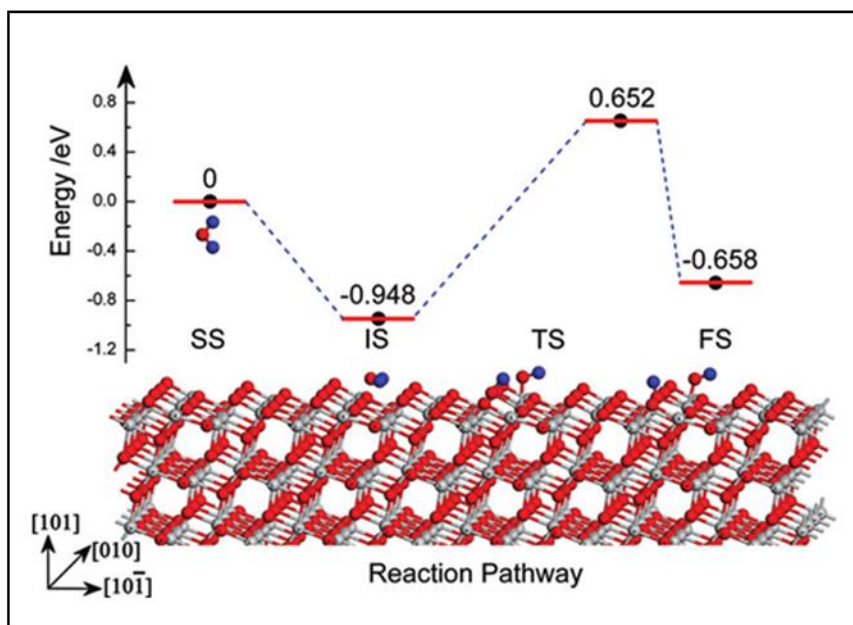
Fig.3. 4 Reaction pathway and the energy state for water adsorption and decomposition on TiO2 surface

(**122**).

2.2 Effect of alloying elements models

Addition of alloying elements can significantly alter the physical properties of metallic materials. There were many DFT computation efforts to reveal the fundamentals of alloying effect on such physical property behaviors. In this subsection, we introduce a couple of previous DFT models regarding the effect of alloying elements on the corrosion behavior of metals.

2.2.1 Liu et al. 2011 (123)

The DFT study by Liu et al. (123) focused on the surface dissolution behavior of Al (100) surface including the effect of different alloying elements such as Zn, Ga, In, Sn, and Pb. In the calculation, they tested the Al (100) surface with different coverage by adding alloying elements and also by producing cavity as shown in the images of Fig.3.5.
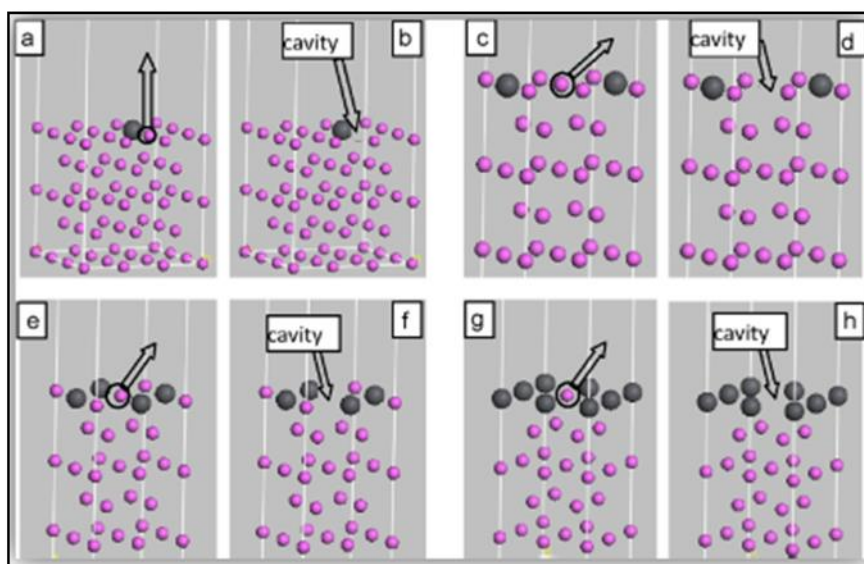
Fig.3. 5 Aluminum surface with different coverages 1/9 ML (a and b), 1/4 ML (c and d), 1/2 ML (e and f) and 3/4 ML (g and h) **(123)**

Alloying elements were doped on the surface with coverage of 1/9, 1/4, 1/2, and 3/4 monolayer (ML). By comparing the surface energies for pure Al and the Al alloy, it has been shown that the systems including alloying elements have lower surface energy. The authors explained this by the lower surface energy of alloying elements compared to that of pure Al. Consequently, the surface energies were calculated to decrease by increasing the number of doped atoms on the surface. An exception of this trend is the system containing Zn. The surface energy in this case decreases for a small number of

doped atoms, but by increasing the number of atoms higher than 1/2 ML, the surface energy of the system increases. They related this different behavior to the nature of Zn as a transition metal compared to the other alloying elements which are sp metals. Thus, this strange behavior might be explained by the different valance for Zn. Fig.3.6 shows the summary results of the surface energies for Al (100) containing Zn, Ga, In, Sn, and Pb impurities.
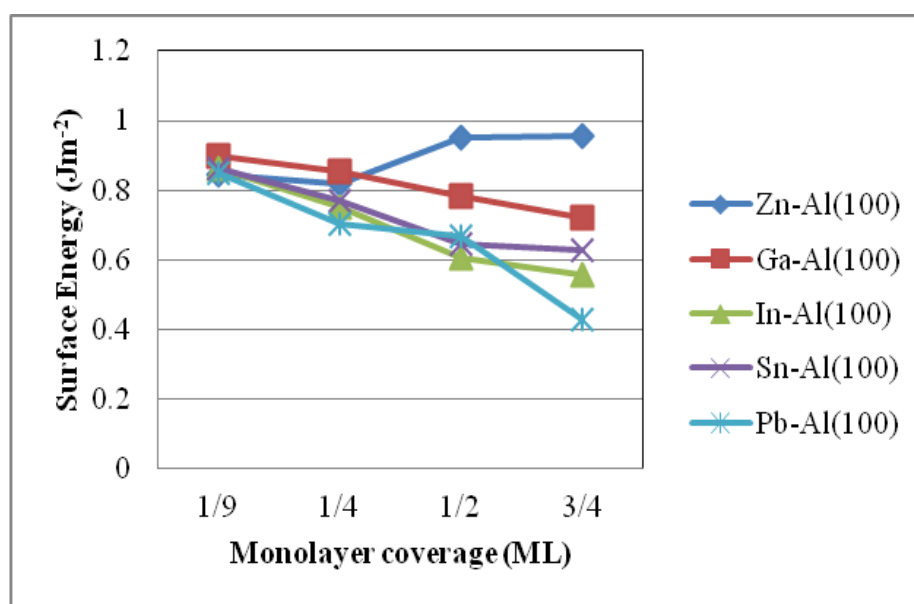
Fig.3. 6 Surface energy for the Me-Al (100) surface (data adapted from **(123)**).

2.2.2 Velikokhatnyi and Kumta, 2010 (57)

Using DFT, Velikokhatnyi and Kumta (57) studied the thermodynamics of hydrolysis and the effect of different alloying elements on the stability of the Mg hydroxides. In developing their model, they compared the free energies of the hydrolysis from the pure Mg and binary Mg alloys as given in Eqs.20-26.

$$Mg_{(s)} + 2H_2O_{(l)} \Leftrightarrow Mg(OH)_{2\,(s)} + H_{2\,(g)} \qquad\qquad \text{Eq.3. 21}$$

$$Mg_{1-x}Ca_{x(s)} + 2H_2O_{(l)} \Leftrightarrow Mg_{1-x}Ca_x(OH)_{2(s)} + H_{2(g)}$$

Eq.3. 22

$$Mg_{1-x}Zn_{x(s)} + 2H_2O_{(l)} \Leftrightarrow Mg_{1-x}Zn_x(OH)_{2(s)} + H_{2(g)}$$

Eq.3. 23

$$Mg_{1-x}Fe_{x(s)} + 2H_2O_{(l)} \Leftrightarrow Mg_{1-x}Fe_x(OH)_{2(s)} + H_{2(g)}$$

Eq.3. 24

$$Mg_{1-x}Fe_{x(s)} + (2+x)H_2O_{(l)} \Leftrightarrow Mg_{1-x}Fe_x(OH)_{2+x(s)} + \left(1+\frac{x}{2}\right)H_{2(g)}$$

Eq.3. 25

$$Mg_{1-x}Al_{x(s)} + (2+x)H_2O_{(l)} \Leftrightarrow Mg_{1-x}Al_x(OH)_{2+x(s)} + \left(1+\frac{x}{2}\right)H_{2(g)}$$

Eq.3. 26

$$Mg_{1-x}Y_{x(s)} + (2+x)H_2O_{(l)} \Leftrightarrow Mg_{1-x}Y_x(OH)_{2+x(s)} + \left(1+\frac{x}{2}\right)H_{2(g)}$$

Eq.3. 27
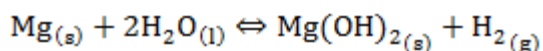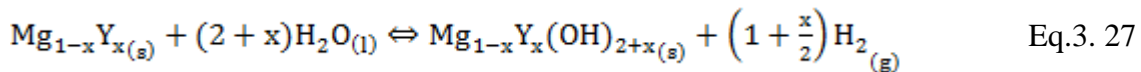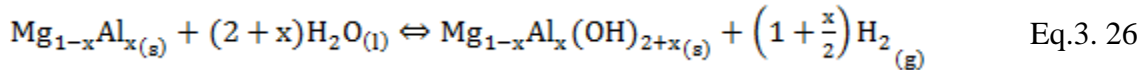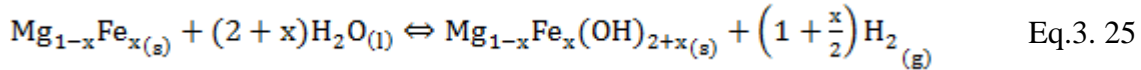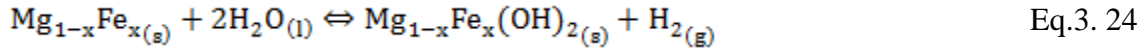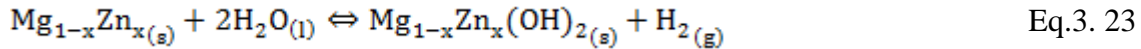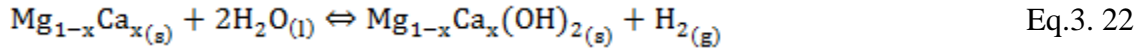
Where we consider that G^{II} is the free energy of the products and G^{I} is the free energy of reactants of pure Mg in Eq. 3. 21, respectively, the free energy change of the reaction (ΔG^R) can be calculated from the following Eq. 3. 28:

$$\Delta G^R = G^{II} - G^{I}$$

Eq.3. 28

And for Mg alloys in Eq.3.22-27, when the G^{IV} represents the free energy of the products and G^{III} represents the free energy of reactants, then the free energy change of the reaction can be given by Eq. 3. 29:

$$\Delta G^R = G^{IV} - G^{III}$$

Eq.3. 29

In Eq.3.29, the more negative the ΔG^R, the more probable the reaction. Additionally, they suggested that if $\delta \Delta G^R_{dop} = \Delta G^R_{alloy} - \Delta G^R_{pure}$ is a positive value, then the alloying element delays the hydroxide formation. Considering G=H-TS, they assumed that the temperature for their calculation is absolute zero which means the Gibbs free energy is equivalent to the formation enthalpy (ΔH^{form}). To complete the first

principle study of total energy calculation, they found the formation energy of the possible compounds including Mg^{hcp}, $Mg_{1-x}Ca_x$, $Mg_{1-x}Zn_x$, $Mg_{1-x}Y_x$, $Mg_{17}Al_{12}$, etc., where x takes the values between 1-10 at.%. Using Eqs.3.20-26 and calculating the formation energy of each phase, the authors proposed that either of solid solution or phase separation is favorable. For instance, the formation energy (E^{form}) of $Mg_{1-x}Ca_x$ is presented in Eq.3.30. In this case, the positive values of E^{form} result in phase separation.

$$E^{form}[Mg_{1-x}Ca_x] = E_{el}[Mg_{1-x}Ca_x] - (1-3x)E_{el}[Mg^{hcp}] - xE_{el}[Mg_2Ca] \qquad Eq.3.\ 30$$
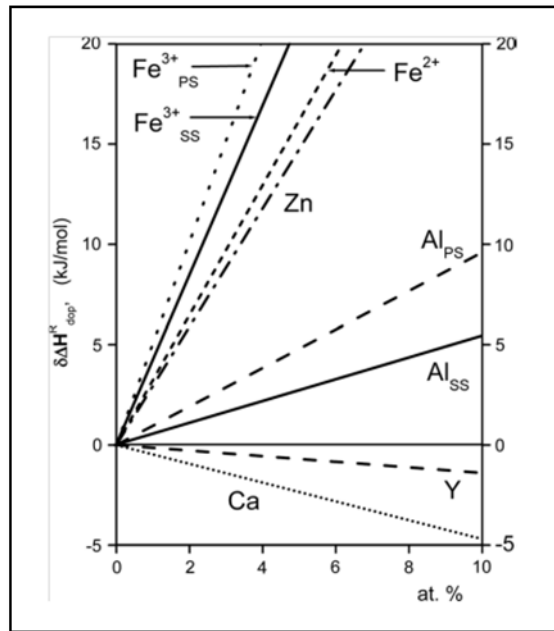
Fig.3. 7 Tendency of hydrolysis for different percentage of alloying elements doping **(57)**.

Their computations ended with the results presented in Fig.3.7. The values of $\delta\Delta H^R_{dop}$ (i.e., the change in the ΔH^R_{dop}) in this graph represent the chemical affinity of Mg alloys for hydrolysis. The negative enthalpies and the resultant free energies for Ca and Y are evidences for the higher thermodynamic driving force for the hydrolysis. On the other

hand, addition of Al, Fe, and/or Zn decelerates the hydrolysis reaction compared with the pure Mg system since they exhibit positive values for $\delta\Delta G^R$.
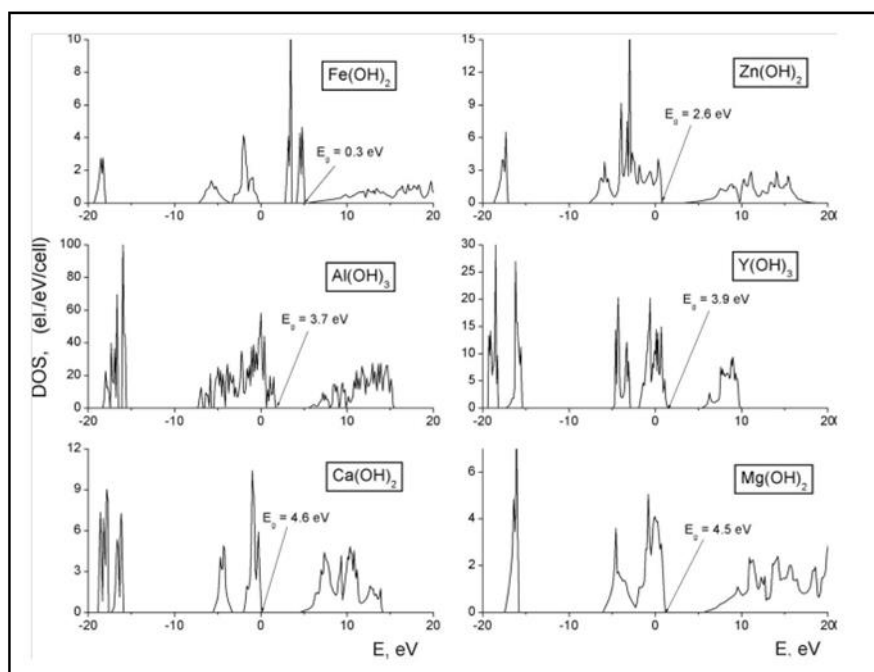
Fig.3. 8 DOS for pure hydroxides (57).

In their work, the authors reported another aspect that might be helpful for better understanding of the phase stability, the density of electronic states (DOS). The result of DOS as a function of energy for hydroxides is shown in Fig.3.8. In these graphs, E_g stands for the band gap, i.e., the energy difference between conduction band and valence band, and the arrows show the Fermi energy (E_F) position. Comparing E_g of different hydroxides, it was demonstrated that materials with higher ΔH^{form} have wide band gaps, including $Ca(OH)_2$, $Mg(OH)_2$, $Y(OH)_3$, and $Al(OH)_3$. It is considered that the large band gap will contain a higher cohesive energy, and consequently it will generate a more stable hydroxide.

3. DFT model development in our work

The DMOL3 package, i.e., local density functional calculations on molecules, implementing DFT was used throughout this work (102). The exchange-correlation energy was treated with PBE functional in the GGA scheme (107). The ground state energy of the system is defined to be functional of the charge density and it can be calculated using minimization of the functional (102). The basis set used in this calculation was double numerical basis set developed by polarization function (DNP) (124). The charge density of self-consistent iteration tolerance was set as 10^{-6}. To speed up the self consistent field (SCF) convergence, direct inversion in the iterative subspace (DIIS) with the size of 6 and 0.005 Ha smearing were used in our calculations. The k-points was set to 2x2x1 for 3x3x2 supercells and 1x1x1 for larger (4x4x2) supercells, and all of the electrons were involved in the calculations. Using the mentioned parameters, we firstly optimized pure Mg structure. The optimized cell lattice parameters were a=b=3.2246 Å and c=4.9657 Å, which shows a consistent results with experimental values a=b=3.2095±0.0002 Å and c=5.2107±0.0002 Å (125). Fig.3.9 shows the unit cell of Mg which contains two atoms.
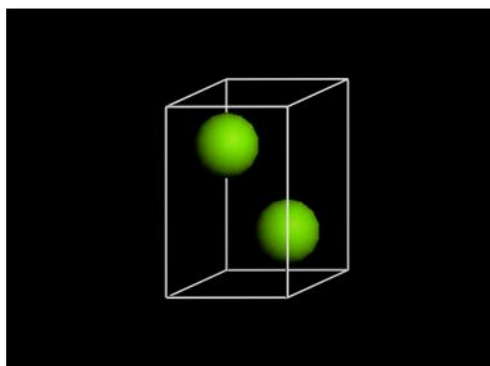
Fig.3. 9 Unit cell of Mg

We then optimized the unit cell to (3x3x2) or (4x4x2) (x, y, and z directions, respectively) super-cells, and cleaved them to the basal (0001), prism $(10\bar{1}0)$ planes and to a pyramidal plane $(\bar{1}01\bar{1})$. The vacuum slab thickness was chosen to be 30 Å. Structural images for the 3x3x2 supercell and cleaved slab models are shown in Fig3.10 and Fig.3.11, respectively. In these calculations, the position of bottom layer was fixed to represent the bulk region, and the top three layers were relaxed. A 3x3x2 slab model of Mg with one doped atom was used to study the effect of alloying elements. The doped impurity atom was either of Al, Zn, Ca, or Y.
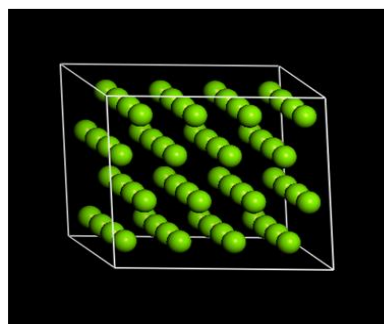
Fig.3. 10 3x3x2 supercell of Mg
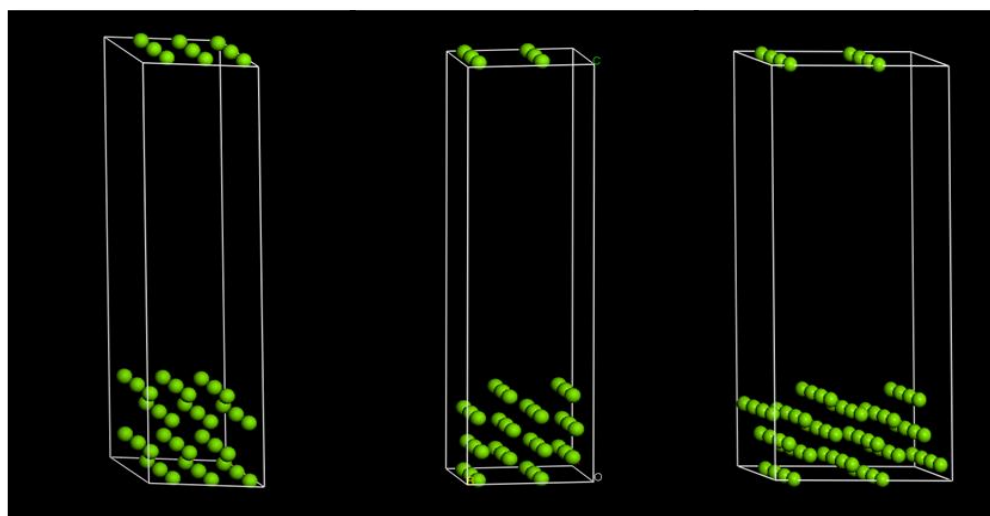
Fig.3. 11 Crystallographic orientation of Mg slab. From the left to the right, the slabs contain the basal (0001), prism $(10\bar{1}0)$ and pyramidal $(\bar{1}01\bar{1})$ planes.

Another set of computations in this work was the dissolution potential calculation. Same computation parameters were used to perform the dissolution potential computations. Based on these computations, the chemical potential and the changes in dissolution potential were obtained. For this set of calculations, dissolution of Mg atoms was simulated by creating a vacancy and removing the atoms from the surface layer. The change of the energy from the perfect suppercell to the supercell with vacancies provides the chemical potential, and the comparison of the chemical potentials for the pure and alloyed Mg results in the prediction of dissolution potential. Using these data, the tendency of material for corrosion can be estimated.

The final set of calculations focused on the adsorption energy of the water molecule on the surfaces of pure Mg and Mg with one impurity atom doped on the surface layer. The optimum potential energy and the equilibrium configuration were calculated by changing the position of water molecule on top of the metal surface. To calculate the adsorption energy, we have set the locations of the water molecule on top of the alloying element as position one (P_1) and above the Mg atom as position two (P_2). For P_3 position, an arbitrary position between the alloying element and the Mg atom was chosen. Fig.3.12 shows the positions of water molecule on top of the Mg alloy surface in three different cases. The equilibrium distances/configurations of a water molecule for these positions (P1, P2, and P3 as shown in Fig.3.12) by minimizing the potential energy were calculated. The density of states (DOS) of the system before and after the interaction was also examined. The details of all of these results including analyses will be provided in the next chapter.
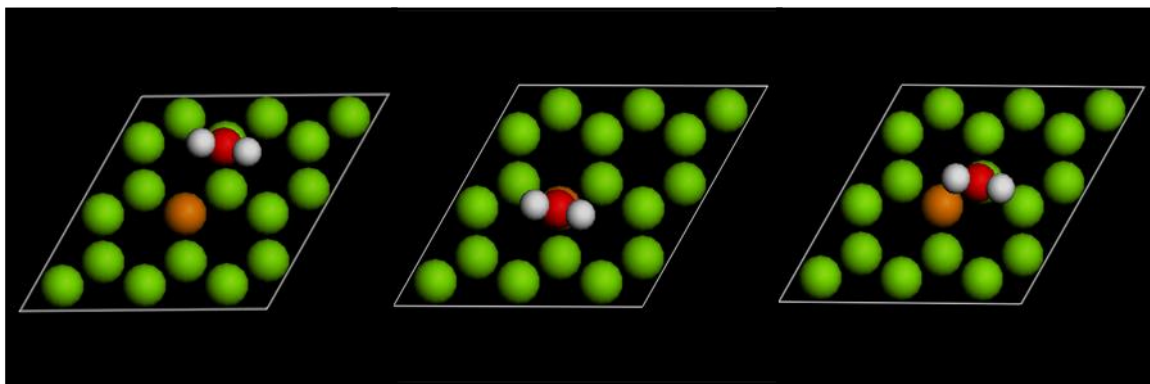
Fig.3. 12 Water molecule position on top of the Mg alloy surface From Left to right P1 the water molecule is located on top of the Mg atom, P2 the water molecule is on top of the alloying element and P3 the water molecule is in between the Mg and the alloying atom.

Chapter 4: Results and Discussion

In this chapter, the results from the developed DFT models are presented and discussed. The results consist of three parts, i) surface energy calculation, ii) dissolution potential calculation, and iii) water molecule adsorption calculation of Mg based alloys. These are the most important aspects of Hydrolysis mechanisms closely related to the corrosion/degradation behavior of Mg/Mg alloys.

1. Surface energies of Mg and Mg alloys

As it was mentioned before, surface energy of Mg/Mg alloys can play an important role in the corrosion behaviors. It is claimed that sometimes, the surface energy of different alloys can assist the estimation of their corrosion resistance. Eq.4.1 given below is the DFT formula to calculate the surface energy of Mg alloys.

$$\gamma = \frac{E^{Slab}_{Mg-Alloy} - 0.5 n_{Mg} E^{Bulk}_{Mg} - 0.5 n_{Alloy} E^{Bulk}_{Alloy} - 0.5 E^{unrel}_{Mg-Alloy}}{A} \qquad \text{Eq.4. 1}$$

In this equation, the slab energy of the alloyed Mg (0001), $E^{slab}_{Mg-Alloy}$, is the total energy of the system when the three top layers are free for optimization and one bottom layer is fixed. n_{Mg} and n_{Alloy} are the numbers of Mg atoms and the alloying atoms, and E^{Bulk}_{Mg} and E^{Bulk}_{Alloy}, are their corresponding bulk energies, respectively. E^{unrel} is the energy of the system when all the atoms are fixed in their Cartesian and fractional positions. The factor 0.5 comes from the freedom of the upper part of the slab for relaxation and fixation of the lower portion, and A is the surface area of the slab model. In the pure Mg system,

there are no alloying atoms in the composition, therefore, n_{Alloy} is equal to zero, which reduces Eq.4.1 to Eq.4.2.

$$\gamma = \frac{E_{Mg}^{Slab} - 0.5 n_{Mg} E_{Mg}^{Bulk} - 0.5 E_{Mg}^{unrel}}{A}$$ Eq.4. 2

1.1 Surface energy of different crystallographic orientations

It has been shown that pure Mg and Mg alloys such as AZ31 exhibit different corrosion behaviors depending on the crystallographic orientation of the surface in contact with corrosive media (70; 72; 126). To study this effect, the pure Mg slab was cleaved to contain the basal (0001), prism $(10\bar{1}0)$, and pyramidal $(\bar{1}01\bar{1})$ planes. The cleaved slabs were separated from each other by a vacuum space to avoid the interaction of the layers resulted from periodic boundary condition along the vertical direction. The thickness of this vacuum space was 30 Å in the slab thickness direction (z-direction), as shown in the previous chapter (see Fig.3.11). The structures were optimized and their total energies were converged to the lowest possible values. For the first set of calculations, all of the three models were pure Mg. Therefore, Eq.4.2 was used to calculate their surface energies. Fig.4.1 shows the visualization of the surface atoms for three different crystallographic planes. Surface atoms are indicated as gray spheres in this image while the bulk atoms are colored as bright green.
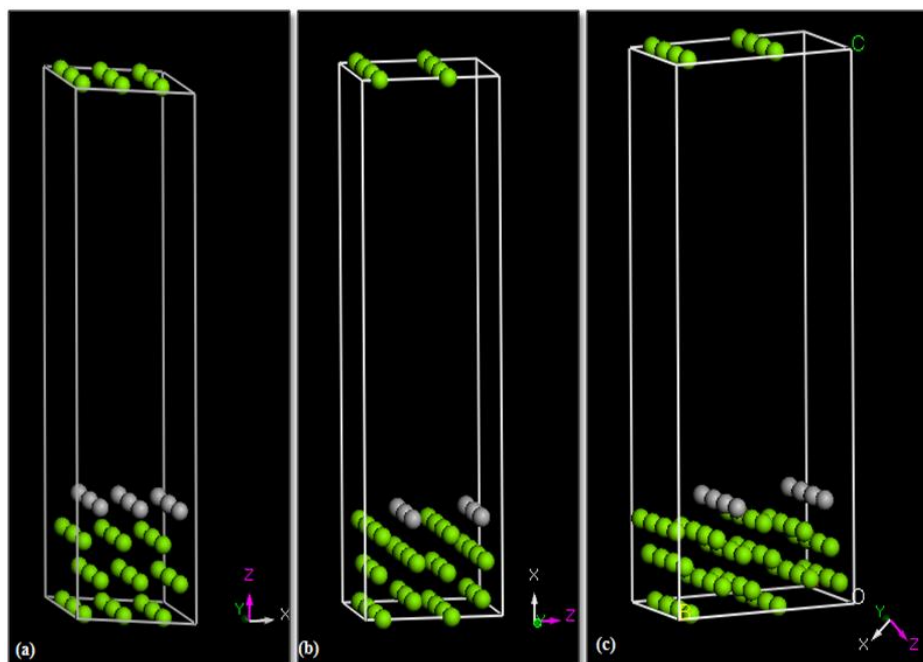
Fig.4.1 DFT vacuum slab models to show the surface atomic layer of Mg with (a) basal, (b) prism, and (c)

pyramidal planes

Fig.4.1 shows that there are different number densities of atoms on the surface for each crystallographic orientation, and also it shows unequal lattice parameters for each of these systems. We calculated the density of atoms for these surfaces by dividing the number of atoms to the corresponding surface area. Fig.4.2 shows the density of atoms in selected surfaces. Basal plane has the highest atomic density among these three surfaces followed by prism and pyramidal planes. Later we can use these data to verify if there is any relationship between the density of atoms in the surface and the surface energy.
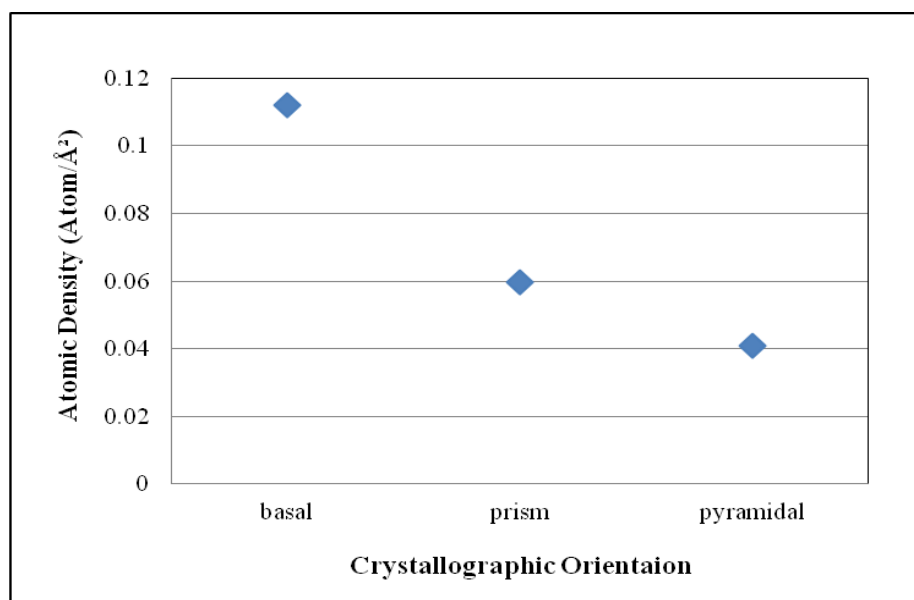
Fig.4. 2 Density of atoms per unit of area for selected crystallographic planes

Fig.4.3 presents the surface energies calculated from DFT computations in this work. It was found that the lowest energy for the Mg surfaces is associated with the basal plane. The numerical value calculated from Eq.4.2 for this plane was 0.75 J/m^2, which is consistent with the reported experimental surface energy, 0.76 J/m^2 for pure Mg (127). From Fig.4.2 and Fig.4.3, the well-known reverse relationship between the density of atoms on the surface and the surface energy is clearly seen. It shows that the system with highest packing density provides lowest surface energy and highest stability. In other words, the closely packed surface for the metal is more stable compared to the loosely packed surfaces. The higher stability comes from the fact that the closed packed surface encloses higher binding energy and higher atomic coordination resulting in lower surface energy. As Fig.4.2 and Fig.4.3 show, the basal plane has the highest atomic density and the lowest surface energy resulting in the highest stability, followed by the prism plane. The least stable plane among these three planes is the pyramidal plane. This plane has an atomic density less than half of the basal plane. The small number of atoms on the

surface in this plane means that each atom has less number of neighbors and consequently there is less attraction for the surface atoms from their surrounding atoms, resulting on instability of the surface.
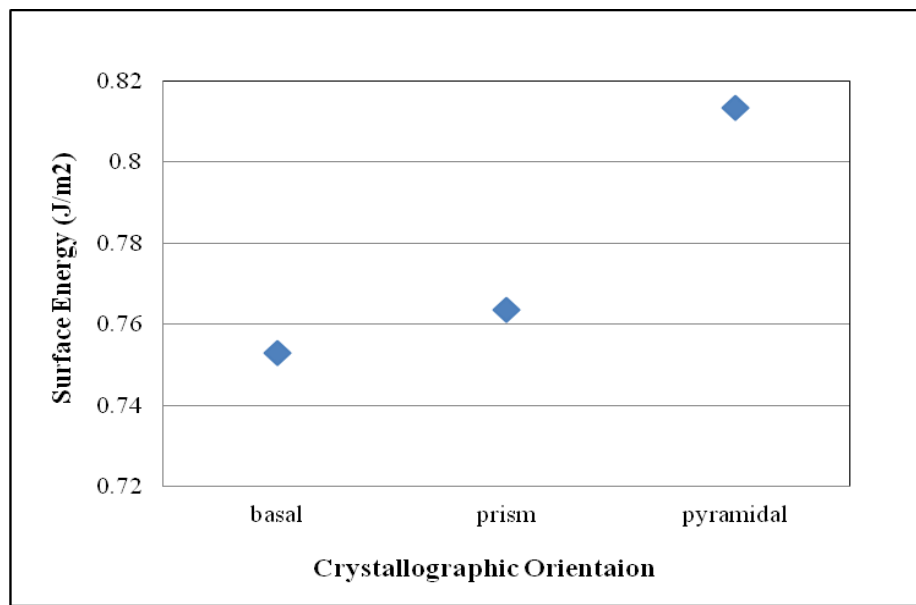
Fig.4. 3Surface energy of surfaces with different orientations

As it was mentioned the corrosion rate depends on the surface behavior and specially the surface energy of the system. Sometimes, it is thought that the packing density has a direct relationship with the activation energy for dissolution rate of metal surface. In general, due to the higher stability of the surface with high packing density, the activation energy of stable surface is higher and removing metallic ions from the surface is more difficult. Such relationship can be proved by applying Tafel equation and by comparing the dissolution rate for different planes. Tafel equation is widely used expression to quantify the dissolution/electrochemical reaction rates of metallic materials, as given in Eq.4.3 (128).

$$I_a = nFk \exp\left(\frac{Q + \alpha nFE}{RT}\right) \qquad \text{Eq.4. 3}$$

In this equation, n is the number of electrons, F is the Faraday constant, k is the reaction constant, Q is the activation energy to remove a metallic ion from the lattice and dissolve in the solution, E is the surface energy, R is the gas constant, and T is the absolute temperature. Calculating the ratio of corrosion rates for two different planes in the form of $\frac{I_0^{(klmn)}}{I_0^{(0001)}}$ provides an estimation of the effect of crystallographic orientation on the corrosion rate with reference to the basal plane. This ratio can be calculated from Eq.4.4 (128).

$$\frac{I_0^{(klmn)}}{I_0^{(0001)}} = \exp\left\{\frac{\alpha\left[Q^{(klmn)} - Q^{(0001)}\right]}{RT}\right\} \qquad \text{Eq.4. 4}$$

Where α is the proportionality coefficient when the surface energy is used instead of the activation energy in this Arrhenius type of equations. The surface energy of basal, prism, and pyramidal planes are calculated as 0.75, 0.76, and 0.81 J/m^2, respectively, which can be converted to 40430, 76879 and 119749 J/mol. The body temperature is considered to be 310 K and R is 8.314$\frac{J}{mol.K}$. If these values are plugged in Eq.4.4, based on the 1.1-2 range for dissolution ratio of prism over basal planes ($\frac{I_0^{(10\bar{1}0)}}{I_0^{(0001)}}$) from the experimental results from (128; 126) the proportionality coefficient α is obtained as 0.007-0.049. In this calculation, we assumed the average value of 0.028 for α, then the $\frac{I_0^{(klmn)}}{I_0^{(0001)}}$ ratio for $\frac{I_0^{(10\bar{1}0)}}{I_0^{(0001)}}$ and $\frac{I_0^{(\bar{1}01\bar{1})}}{I_0^{(0001)}}$ then become 1.486 and 2.367 respectively. These are considered as the approximated prediction value for the dissolution rate ratios of prism to

basal and pyramidal to basal planes, respectively. Note that it is based on the assumption that the surface energy is primarily determining the dissolution rate and the proportionality coefficient α is constant regardless of the surface orientation. Later we will apply the same proportionality coefficient to provide similar calculations using the Tafel equation to estimate the impacts of alloying elements on the dissolution potential.

Considering that the surface energy of Mg with basal plane is the lowest, the primary focus of the rest of calculations in the present study is on the results from the systems with the basal (0001) plane orientation.

1.2 Effects of alloying elements on surface energy

Alloying elements were presented as one of the effective factors to influence the corrosion behavior of Mg alloys in chapter 2, section 3.1. Our computations for the surface energy of selected binary alloys including Mg-Al, Mg-Ca, Mg-Zn, and Mg-Y shows that the surface energy of Mg varies with doping a substitutional atom to the surface. In these calculations, one atomic position of Mg on the surface was occupied by the alloying atom. The interaction between the doped atom and the Mg matrix and the electron exchange among them determine the stability of the surface. To estimate the effect of present alloying element on the improvement of the surface stability, the surface energy of basal plane of pure Mg was set as the reference.

Fig.4.4 shows the calculated surface energies of Mg alloys with each of the impurity elements using Eq.4.1. As it is obvious in the data presented in Fig.4.4, doping Zn on the surface of the Mg slightly decreases the surface energy of the alloy resulting in small improvement on the stability of the system. On the other hand, incorporation of Ca, Al, and Y shows negative effect on the stability of the surface. The destructive effect of

Al and Y is more considerable, while doping the Ca atom on the surface does not seem to cause a critical change in the surface energy. This trend can be explained by the fact that the surfaces including alloying atoms (Zn^{2+} and Ca^{2+}) that have identical number of valance electrons with Mg metals (Mg^{2+}) can maintain their stability and show slight difference in their energy. However, as the doped atom varies to an atom with different number of valence electrons, the surface energy increases and causes instability in the system. In this case, Al and Y have respectively incomplete p and d orbitals while Zn, Ca, and Mg have their valance electrons in orbital s Therefore, doping Ca or Zn on the Mg surface does not influence on the density of electrons of other orbitals rather than s. In other words, since the shared electrons for Zn and Ca are from the same orbinal as Mg, the electrons density for the surface does not change considerably. However, the presence of Al and Y on the surface changes the density of electrons in p and d orbitals respectively. It is thought that this change in the density of electrons in other orbitals than the pure Mg (i. e., the s orbital) can cause the instability for the surface. The involved orbital and the number of valance electrons in system are the most important factors influencing the surface energy and independent of the atomic size may result in a vulnerable surface. In other words, same number of valence electrons in the outer shell orbital of the atoms of Mg, Zn, and Ca causes homogenous distribution of electrons in the system, and differences in the number of valance between Mg and Y/Al can cause less stable surfaces and decrease the stability of the system.
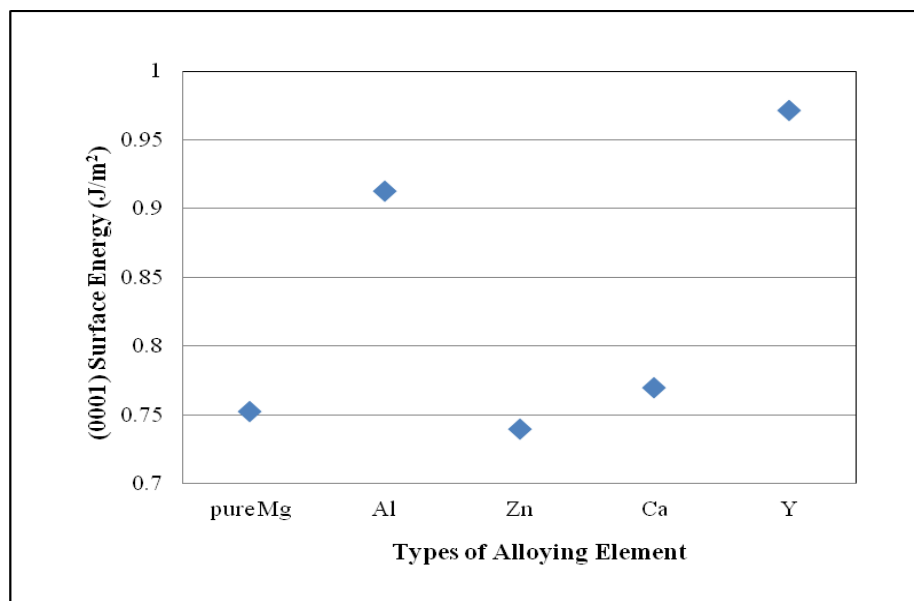
Fig.4. 4 Surface energy of Mg alloyed with different doping elements.

Comparison of the ionic radius of the metallic elements from Table 4.1 shows the dependence of the surface energy on the size of the doped atom (129). The results show that larger atomic radius of Ca shifts the surface energy of the alloy slightly toward higher values and decreases the stability of the surface by causing distortion in the structure, whereas the presence of Zn in the same position stabilizes the surface and shifts the surface energy toward lower values due to its similar ionic radius to Mg^{2+}. Similar scenario is true for Y and Al. In other words, the Y atom causes more instability in the surface than Al due to its higher atomic radius. As a result, the difference in size of atoms is another factor and the valance number seems to be more important. Organizing the data, Y with highest surface energy affects the steadiness of Mg due to variant number of valance electrons and larger atomic radius, followed by Al with only different number of electrons in valance band and even smaller atomic radius. Although Ca has same number of electrons in the valance band as Mg but the larger atomic radius results in a slight raise in the surface energy. Finally the least destructive alloying element from the surface

energy point of view seems to be Zn with smaller atomic size compared to Mg and similar number of valance electrons.

Table 4.1 Ionic radius of some metals **(129)**

Metal	Mg^{2+}	Ca^{2+}	Zn^{2+}	Y^{3+}	Al^{3+}
Ionic radius (nm)	0.072	0.100	0.074	0.090	0.054

The surface energy of pure alloying elements is the third parameter that can influence the surface energy of Mg alloys. Table 4.2 presents the surface energy of these pure metals (127). Comparing the data from this table for Mg and the alloying elements shows that the alloying elements such as Y and Al that have considerably larger surface energies compared to pure Mg, increase the surface energy of the alloy. On the other hand, Ca and Zn with smaller difference in surface energy with the pure Mg do not cause significant changes in the surface energy of the Mg alloy. Although the surface energy of pure Zn is higher than the pure Mg, doping of Zn to the Mg surface decreases the surface energy of the system the reason for this unusual change may be the small difference between the ionic radius of the Zn^{2+} and Mg^{2+}. In conclusion, several parameters influence the surface energy of the Mg alloy, and among them, it is thought that the most important one is the similarity in the number of electrons in the last orbital of the elements. The ionic radius and the surface energy of the alloying elements are also important, but their influence is not as important as the valency.

Table 4.2 Surface energy of pure metals **(127)**.

Metal	Mg	Ca	Zn	Y	Al
Surface energy (J/m^2)	0.76	0.49	0.99	1.125	1.160

Fig.4.5 shows the effect of percentage of alloying element on the surface energy of the alloy. The doping of the alloying element on the surface of the alloy is based on the assumption that there are $\frac{1}{9}$ alloying atoms on the surface of the alloy and that the surface energy is not strongly influenced by the inner (bulk) composition of Mg alloys. Consequently, it can be approximated that we have 11.1% (i.e., 1/9) alloying atoms on the surface layer. Using this data, the effect of different amounts of alloying elements on the surface energy of Mg alloys can be estimated. For this, we have also assumed that the surface energy changes are linearly proportional to the contents of alloying element. In other words, there are no interactions between impurity atoms on the surface and the impurity atoms are majorly surrounded by the Mg matrix atoms. These are not unrealistic approximations when the contents of impurity elements are sufficiently small (i.e., dilute solution situation) as in Fig.4.5. Based on these assumptions, we have plotted the estimated surface energies of Mg alloys with % contents of impurities. In the figure, the symbols represent the surface energies at 1, 2, 3, 4, and 5 at. % additions of alloying elements and the dotted lines are the trend lines for the four alloying systems. As it is shown in Fig.4.5, increasing the amount of alloying elements from zero to 5% highlights the influence of each alloying element on the surface energy. As expected, among these results, the effect of Y and Al is more obvious while adding higher amount of Zn or Ca does not affect the surface energy significantly.
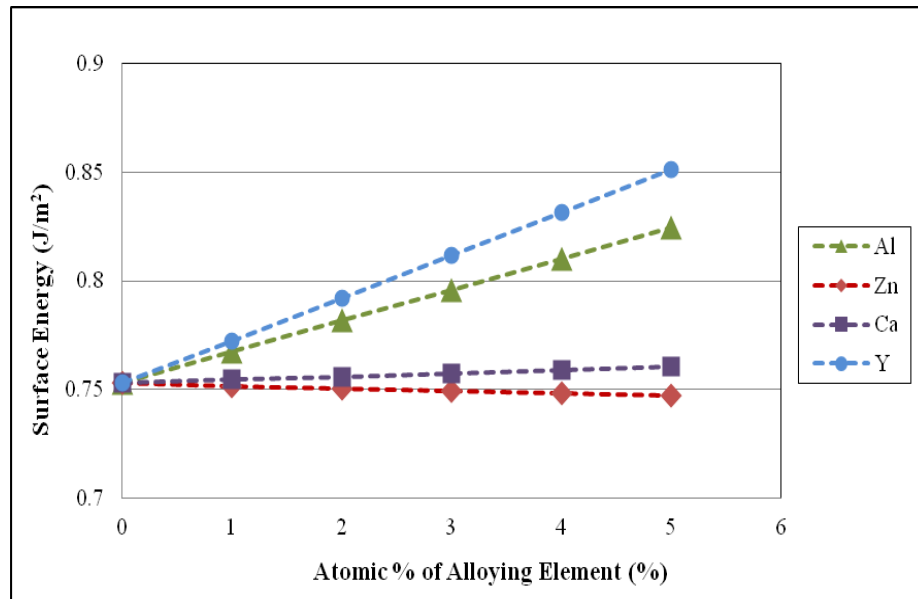
Fig.4. 5 Amount of alloying elements and the surface energy of Mg alloys

Next, we explored the impact of alloying elements on the Mg surface using the Tafel equation. As it was mentioned before an equation similar to Eq.4.4 (i.e., Tafel equation) can be used to study the effect of alloying elements and compare the corrosion rate for different compositions of Mg alloys. Here, Eq.4.5 given below can be applied to quantify the dissolution rate ratios of alloys to the pure Mg system.

$$\frac{I_0^{Alloy}}{I_0^{Pure}} = \exp\left\{\frac{\alpha[Q^{Alloy} - Q^{Pure}]}{RT}\right\} \qquad \text{Eq.4. 5}$$

In applying Eq.4.5, the proportionality coefficient (α) must be specified again. Here, we assumed that this proportionality coefficient is similar to the value approximated through the previous analysis. In other words, when the surface energy difference is used to measure the dissolution rates in Mg/Mg alloys (low alloying contents), we assume that the proportionality coefficient in the Tafel expression obtained in the pure Mg can be applied to the Mg alloys. In our following analysis, we have used

0.028 as the coefficient value of α in Eq.4.5. With this, Fig.4.6 shows the ratio of dissolution potential for pure Mg and the Mg alloys. As it is obvious in this graph, for small amounts of alloying elements and up to 3%, the dissolution rate ratio is approximately calculated as 1, which means that the alloying elements have relatively minor effects on the dissolution rate. Also for the case of Zn and Ca, the ratio stays in the same range even for up to 5% of alloying elements. On the other hand, the influence of amount of alloying elements is more highlighted for Al and Y.

As a comparison, it is thought that stability of the system is more influenced by the crystallographic orientation rather than the composition at least for the surface energy and resultant dissolution rate perspective. Note that this is based upon the dissolution rate analysis dependent only on the surface energy differences. However, it is considered that the macroscopic hydrolysis and corrosion behavior are influenced by many other factors and/or mechanisms such as galvanic corrosion, formation and fracture of hydroxide films, and other microstructures.
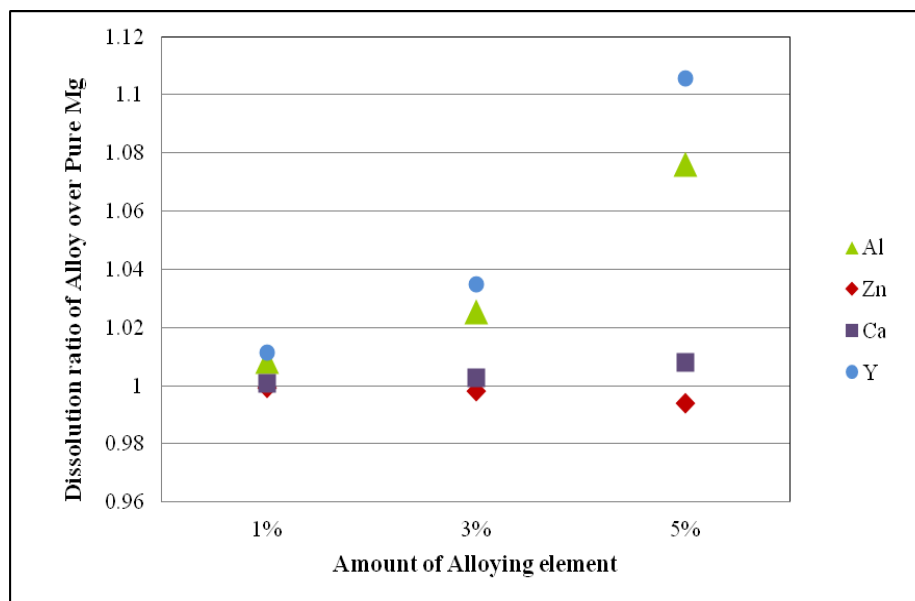
Fig.4. 6 Effect of alloying elements on the dissolution rate of Mg

1.3 Enthalpy of mixing

In the previous section, the effect of surface energy was examined. In the surface energy calculations, the bulk material is assumed to be pure Mg. In this sub-section, we study the bulk behavior of Mg, when other alloying elements are present in it. In these computations, the enthalpy of mixing with respect to the bulk energy is calculated. The results of these calculations (i.e., the changes in the total energies) are presented in Fig.4.6. The changes in the total energies for all of the systems are positive, considering the minor effect for the entropy changes in their solid states. From Fig.4.7, it is seen that the lowest mixing energy belongs to Al due to its small ionic radius, and Ca with the largest ionic radius has the highest enthalpy of mixing. Zn and Y have intermediate values for the enthalpy of mixing. Checking the ionic radius of Zn and Y (shown in Table 4.1) clarifies that although the atomic radius is an important factor but it is not the only parameter influencing the mixing of alloying elements in the matrix. However, by comparing the Figs.4.4 and 4.7, it is certain that the effects of allying elements on the Mg

surface and Mg bulk energy changes are different. Also, the electron valency argument used in describing the surface energy changes does not apply to the bulk energy changes. Comparing Fig.4.5 and Fig.4.8 gives an idea if adding different amounts of alloying elements has the same influence on the bulk energy as on the surface energy. These two graphs show that although adding alloying elements to the composition of the alloy causes changes in both bulk and the surface, but depending on the position of alloying element (bulk or surface) it may increase or decrease the stability of the system.
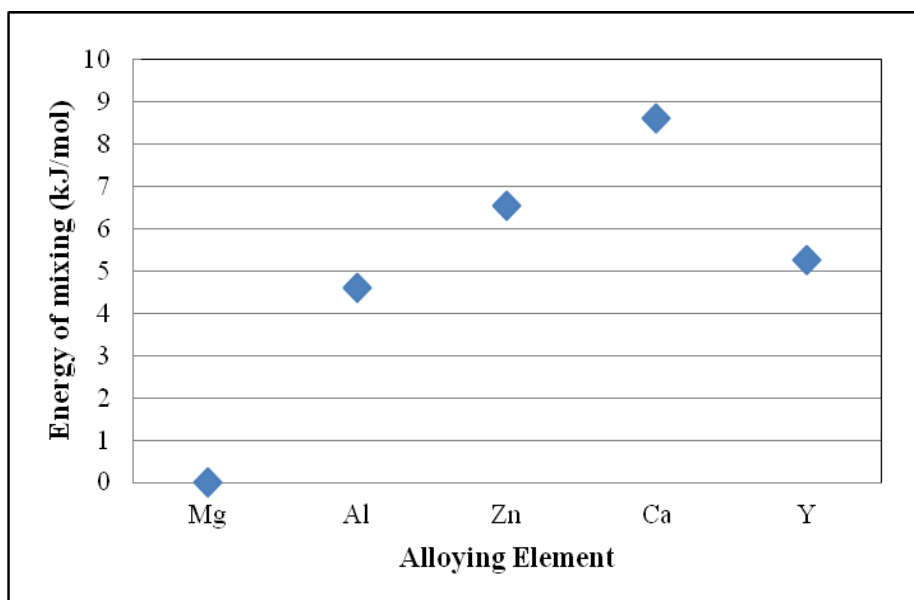
Fig.4. 7 Enthalpy of mixing for different Mg alloys

We performed a similar analysis to the Fig. 4.5, to estimate the total bulk energy changes through the mixing of alloying element with at. %. Again, it must be noted that we assumed a linear relationship between the mixing energy changes and the contents of alloying element by ignoring the interactions of alloying elements themselves at these lower impurity levels.
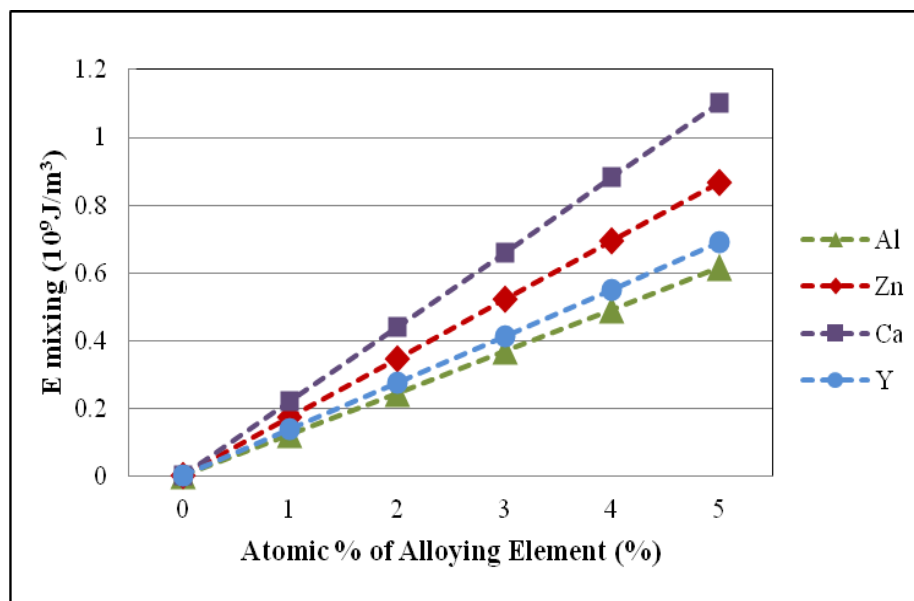
Fig.4. 8 Enthalpy of mixing and alloying elements effect

Apparently, there must be other factors other than the surface energy that will influence the corrosion rate of the metal. In the following sections, some of these factors such as the dissolution potential and the water molecule adsorption energy will be discussed.

2. Electrochemical Potential Shift of the Me-Mg (0001) Surfaces

From Fig.4.4, it was found that the presence of some alloying atoms (Ca, Al, Y) on the surface of pure Mg will make the alloys more active in corrosive media. To study the behavior of the alloy system, an anodic polarization curve is often used. This curve describes the electrochemical behavior of the surface and the dissolution of the ions. Dissolution potential is a measurement of dissolution progress calculated from the difference in the rate of detachment of cations and anions (130). Thus, the electrode potential for pure Mg and Mg alloys are unequal. Keeping this in mind and assuming that the electrochemical reactions shown in Eq.4.6 and Eq.4.10 are the electrode reactions for

dissolutions of pure Mg and Mg alloys, respectively, the chemical potential of different systems can be calculated. Eq.4.7 represents the change in Gibb's free energy over the number of dissolved atoms in constant pressure and temperature. Such free energy change (i.e., chemical potential) can be approximated to the form of Eq.4.8 where E_{slab} is the energy of slab with perfect surface and E'_{slab} is the energy of the same system with one vacancy on the surface, respectively.

$$Mg^{2+} + H_2 \leftrightarrow Mg_{pure} + H^+ \qquad \text{Eq.4. 6}$$

$$\mu_i = \left(\frac{dG}{dn_i}\right)_{T,P,n_j} \qquad \text{Eq.4. 7}$$

$$\mu \approx \frac{E_{slab} - E'_{slab}}{\Delta n} \qquad \text{Eq.4. 8}$$

$$\mu_{Mg^{2+}} + \mu_{H_2}^0 - 2\mu_{H^+}^0 - \mu_{Mg,pure}^{surf} = 2eU_{Mg,pure} \qquad \text{Eq.4. 9}$$

The chemical potential changes of the components in Eq.4.6 are presented in Eq.4.9, where $\mu_{H^+}^0$, $\mu_{H_2}^0$, $\mu_{Mg,pure}^{surf}$ and $\mu_{Mg^{2+}}$ are the chemical potentials of H^+ and H_2 at standard condition, the chemical potential of pure metal Mg atom dissolving from the surface, and the chemical potential of the dissolved ions, respectively, and $U_{Mg,alloy}$ is the electrode potential. Fig.4.9 shows the schematics of perfect slab and also the position of vacancy on the surface of pure Mg (0001).
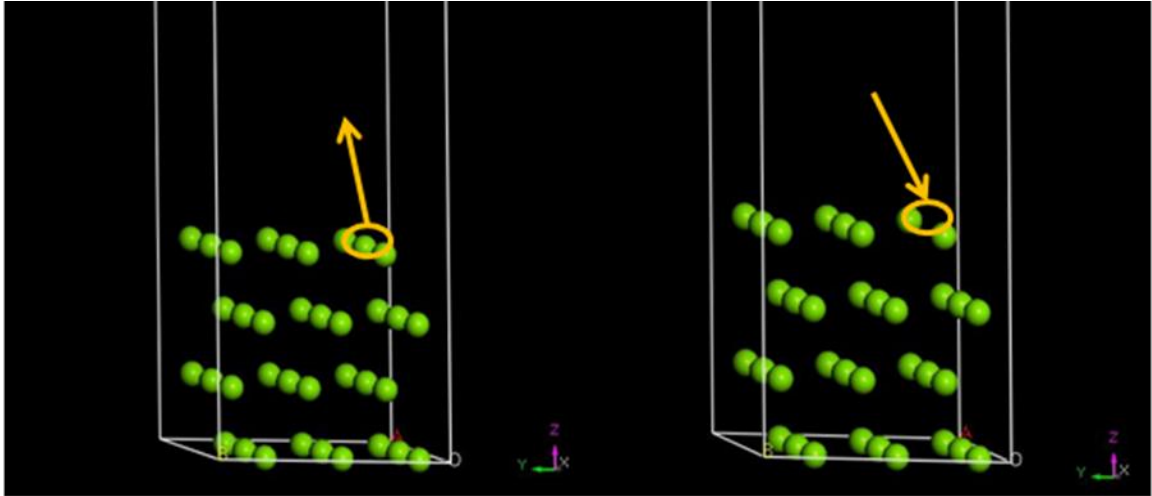
Fig.4. 9 Dissolution of pure Mg

Taking the same path, similar equations for the estimation of the electrochemical potential changes can be derived for Mg alloys, as given in Eqs.4.10 and 4.11.

$$Mg^{2+} + H_2 \leftrightarrow Mg_{alloy} + 2H^+ \qquad \text{Eq.4. 10}$$

$$\mu_{Mg^{2+}} + \mu_{H_2}^0 - 2\mu_{H^+}^0 - \mu_{Mg,alloy}^{surf} = 2eU_{Mg,alloy} \qquad \text{Eq.4. 11}$$

Combining Eq.4.9 and Eq.4.11, the dissolution potential difference (i.e., electrochemical potential difference) between the pure Mg and Mg alloys can be obtained using Eq.4.12.

$$U_{Mg,alloy} - U_{Mg,pure} = \frac{\mu_{Mg,pure}^{surf} - \mu_{Mg,alloy}^{surf}}{2e} \qquad \text{Eq.4. 12}$$

The dissolution potential difference with reference to the pure Mg for different Mg alloys has been presented in Fig.4.10. The results show positive dissolution potential difference for Mg-Al system. The values are negative for three other alloying elements; the difference is negligible for Mg-Zn alloy and relatively small for Mg-Ca alloy, but the dissolution potential difference is considerably large (-0.45 V) for alloy containing Y atoms. Comparing the data from Fig4.10, adding Al to the pure Mg increases the stability

of the material surface and avoids dissolution. It can be interpreted that once an Al atom is positioned on the surface of Mg system, the chance of losing the neighbor Mg is smaller than other systems. On the other hand, it is predicted that, some alloying elements such as Y, increase the tendency for dissolution of the metal. Zn and Ca seem to be less effective from a dissolution behavior point of view since they do not have a significant difference with the pure case, though they impose a negative influence on the dissolution of Mg atoms.

To have a better understanding of the dissolution process, Mg- Al system was used to study the dissolution process. The dissolution potential was calculated for different cases to test the total energy differences for different situations in atomic sites for Mg corrosion. The atomic positions for the vacancies are shown with cross (X) symbols in Fig.4.11. As represented in the figure, we first tested dissolution scenarios of losing Mg and Al atoms (middle column in Fig. 4.11), and we investigated the three more cases for losing second atoms when the Mg atom is initially removed (right-hand side column in Fig. 4.11). Because the system consists of two types of elements (binary system), the first choice for dissolution sites can be either the alloying atom or one of the Mg atoms. When the alloying atom dissolves, the system becomes essentially identical to the pure Mg case, but if the first option is the Mg atom, three different cases are possible in our supercell structure for the second dissolving atom as shown in Fig.4.11. When an Mg atom was initially removed (bottom image in the middle column in Fig. 4.11), we considered three different situations for the second surface atoms to dissolve during corrosion.
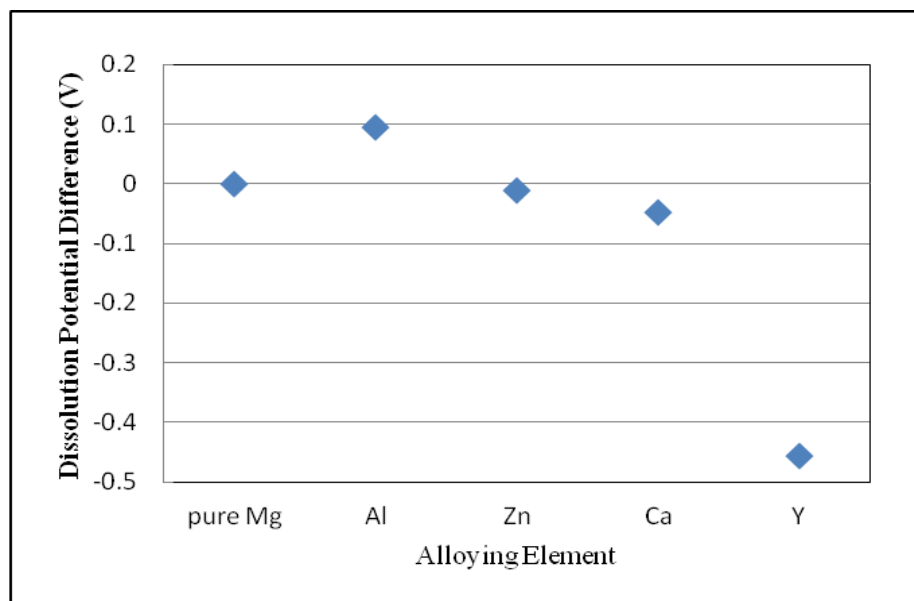
Fig.4. 10 Dissolution potential difference of Mg alloys with pure Mg
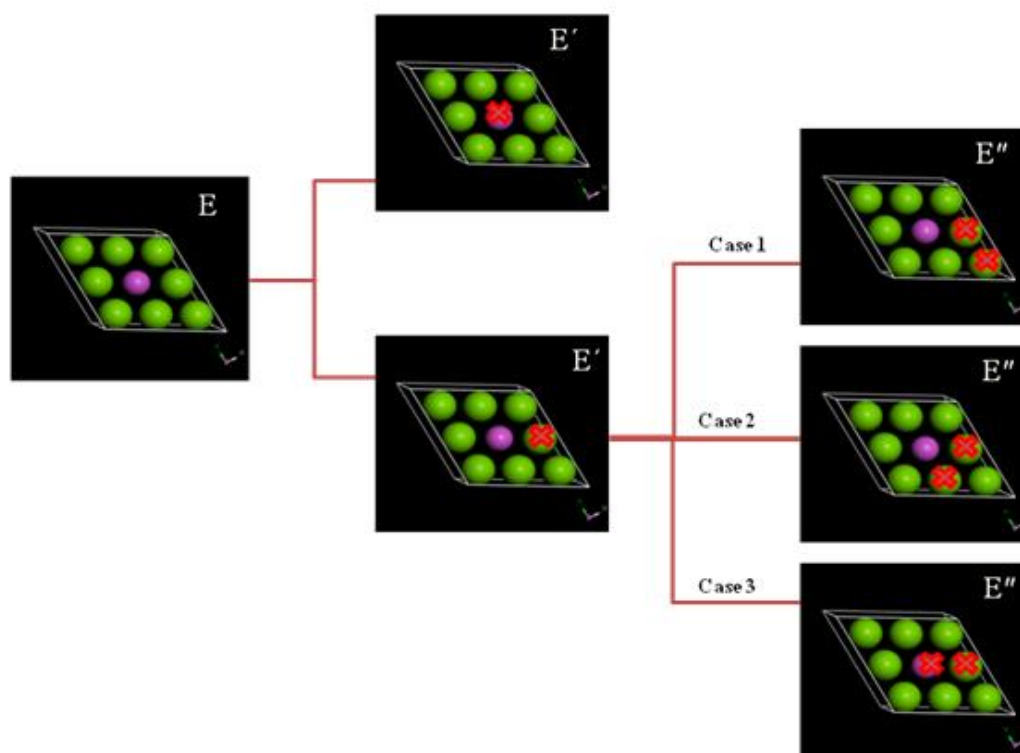
Fig.4. 11 Dissolution sites 3x3x2 Mg-Al alloy
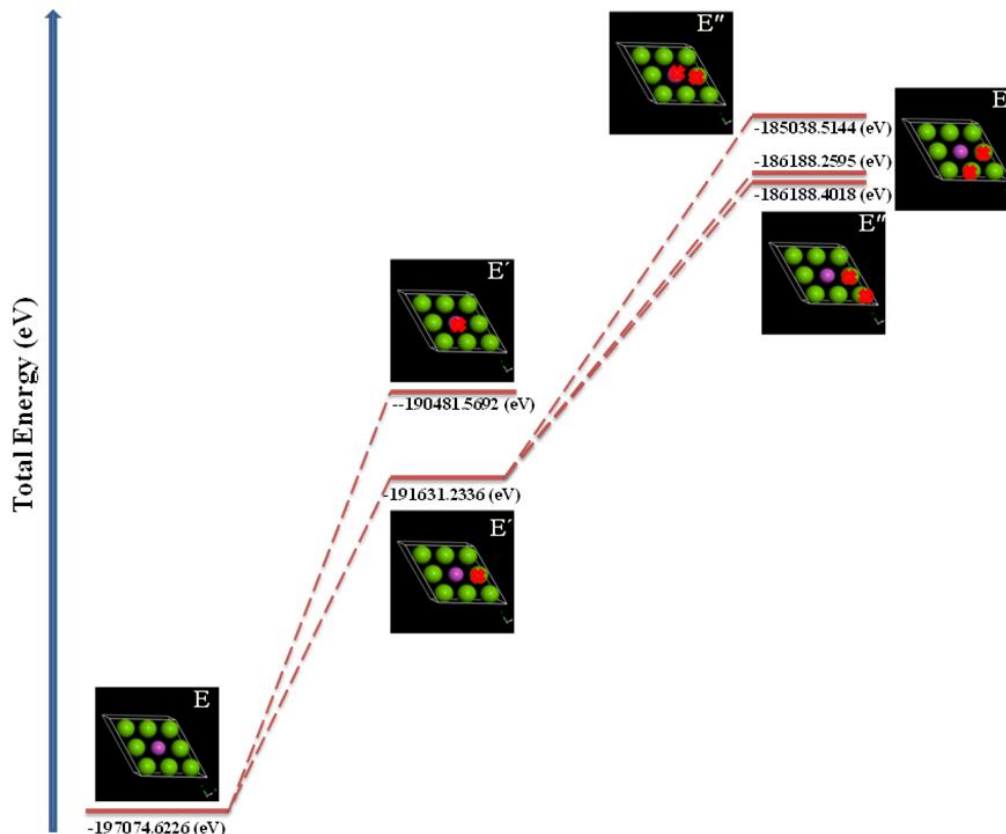
Fig.4. 12 Total energy level for different dissolution cases

The dissolution potential for different atomic sites presented in Fig.4.11 has been calculated using Eq.4.12, and the results from each case are presented in Fig.4.12. In the results of Fig.4.12, the energy levels of the systems are given by the horizontal bar in the diagram. These results show that by dissolving the atoms from the surface, the total energy of the system increases irrespective of the dissolving position. As it can be seen in this diagram, the perfect system has the lowest total energy (left bottom image). The total energy of the system (E) increases to (E´) when one atom is dissolved from the surface. Here, E' and E" in general represent the total energies when the first and second atoms are removed from the surface, respectively. From the results, it is seen that E´ is higher when the alloying atom is removed which means that the dissolution of the alloying atom (i. e.,

Al atom) causes more instability compared to the dissolution of the Mg atoms. Next, three cases were studied to find the most probable choice for dissolution of the second atom. The energy of the system increases to E″ by removing the second atom. It was predicted that this energy value for E″ depends on the position of the second removed atom (the three images on the top right corner). Results show that the highest energy and consequently the least stable condition belong to the case when the Al atom is removed (Case 3 in Fig. 4. 11), which means that dissolution of Al as the second atom is not favorable. On the other hand, the total energies of the system show small difference between the case 1 and case 2 with a slightly higher chance for the case2. Later, we will compare these two positions in a larger system to verify their differences. The dissolution potential calculation results from these three cases in Fig. 4.13 show that, after the first Mg atom is removed, dissolution of an atom in the position similar to case 1 is easier than case 2, because the dissolution potential is more negative for case 1 compared to case 2. On the other hand, as we mentioned from the total energy point of view, it is unlikely that Al will dissolve in the next due to the high dissolution potential (i.e., 574.83 V) (case 3). Accordingly, it seems that there is a large attraction between the alloying element and the surrounding Mg atoms compared to the atoms that are not in direct contact with the Al atom.
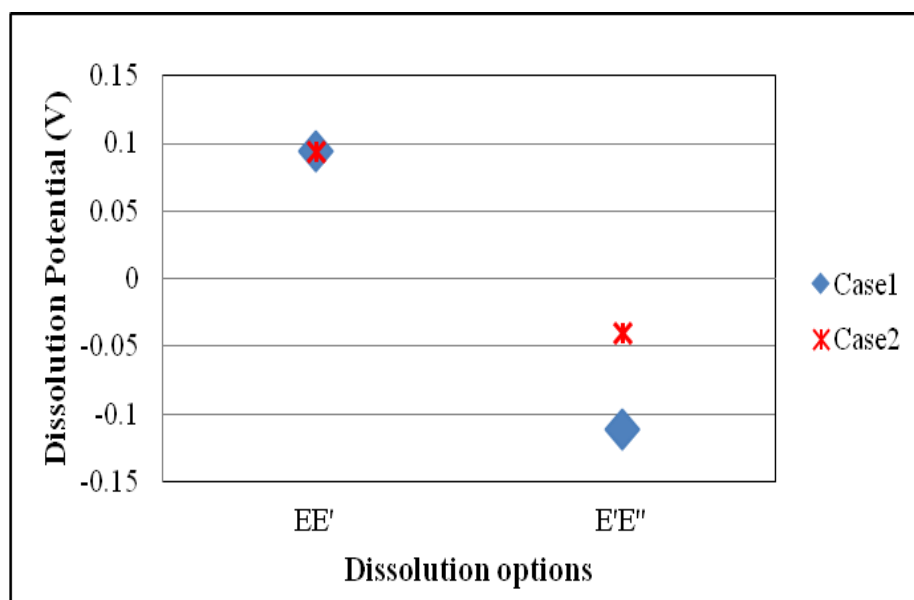
Fig.4. 13 Dissolution potential of 3x3x2 Mg-Al alloy

To verify the difference between case 1 and case 2 from the previous calculation, another set of DFT computations was performed for a larger system (4x4x2 systems as displayed in Fig4.14). As seen in the schematic images of Fig.4.14, the first, second, and third nearest neighbors of the Al atom were removed in separate computations. The total energies of these systems have been compared in Fig.4.15. The results show that dissolution of the first atomic neighbor of Al atom has the highest total energy, followed by third and then second atomic neighbors. Dissolution of the second atom is the easiest cases because the system is more stable after removing this atom compared with the other two cases. Also, the higher total energy of the system after removing the first neighbor indicates that the dissolution of this atom is not favorable. Comparing the dissolution potential of these three systems in Fig.4.16 shows that the dissolution potential difference for the first neighbor is highest, followed by the third neighbor and the second neighbor. The reason for this in thought to be the smaller size of the alloying atom. Here, the Al atom has a small ionic radius that can cause a distortion in the surface atoms as it is

schematically illustrated in Fig.4.17; the first nearest neighbors will move toward the Al atom, and due to this movement of atoms the first atomic neighbors have strong attraction with the Al atom. On the other hand, the distortion and movement of first neighbors produces a larger space between the first neighbors and the second neighbors, which will in turn results in the instability of the second neighbors. Although it is thought that the third neighbors will also be influenced by these larger spaces, but assuming the periodicity of the system, the first neighbors that are adjacent to the second nearest neighbors will produces a larger gap. Therefore, dissolution of the second neighbors would be easier compared to the third neighbors.
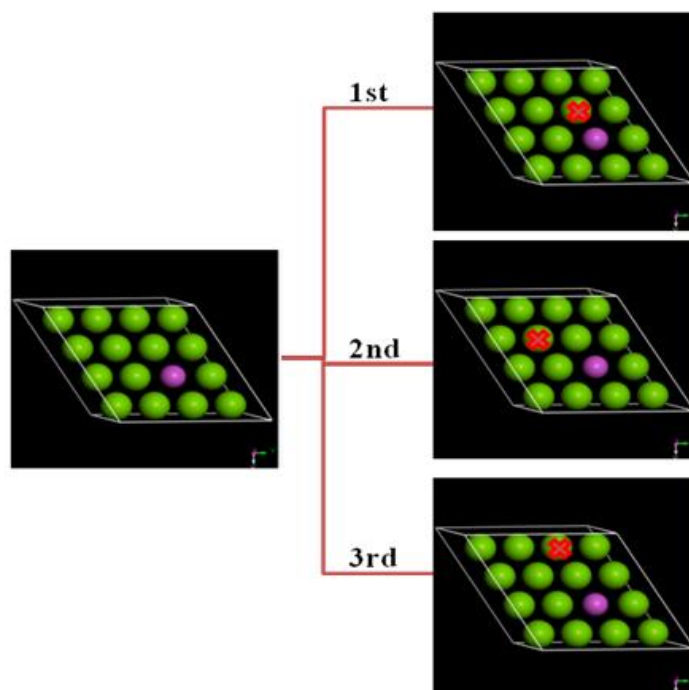
Fig.4. 14 Dissolution sites 4x4x2 Mg-Al alloy
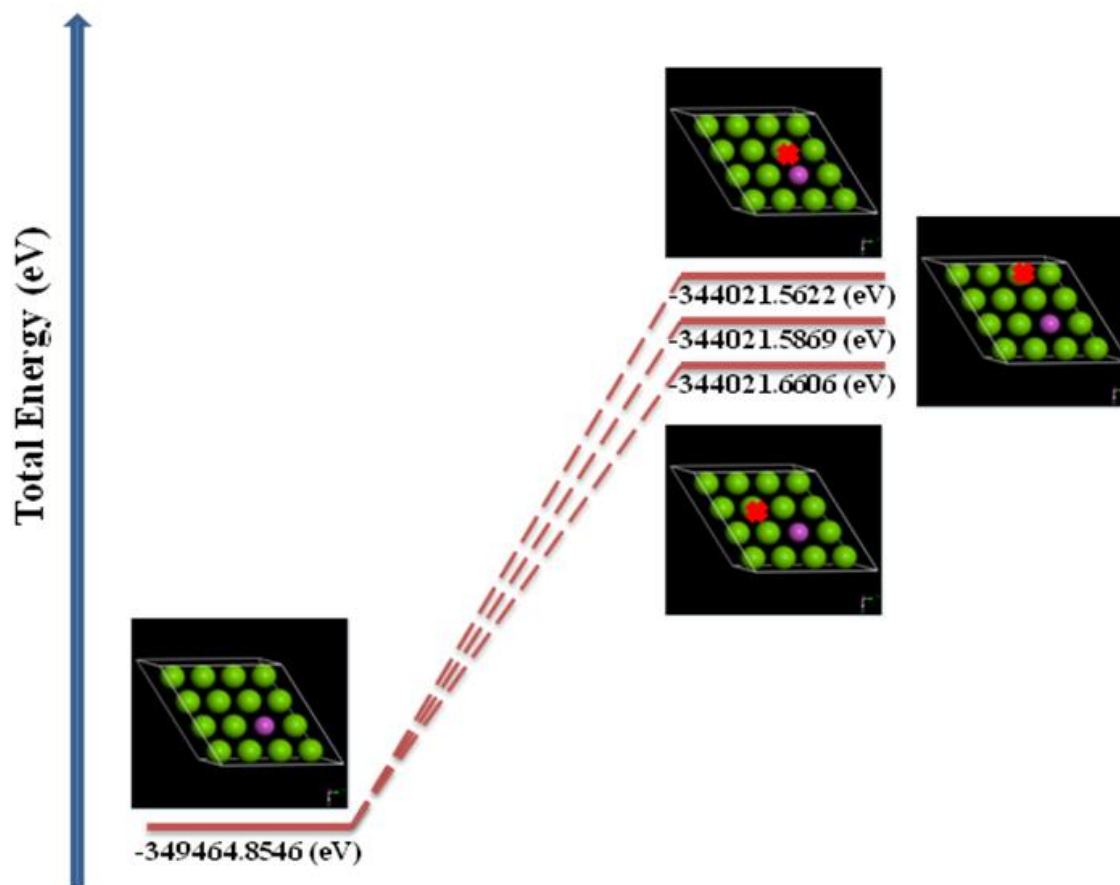
Fig.4. 15 Dissolution of first, second and third neighbors of the Al atom
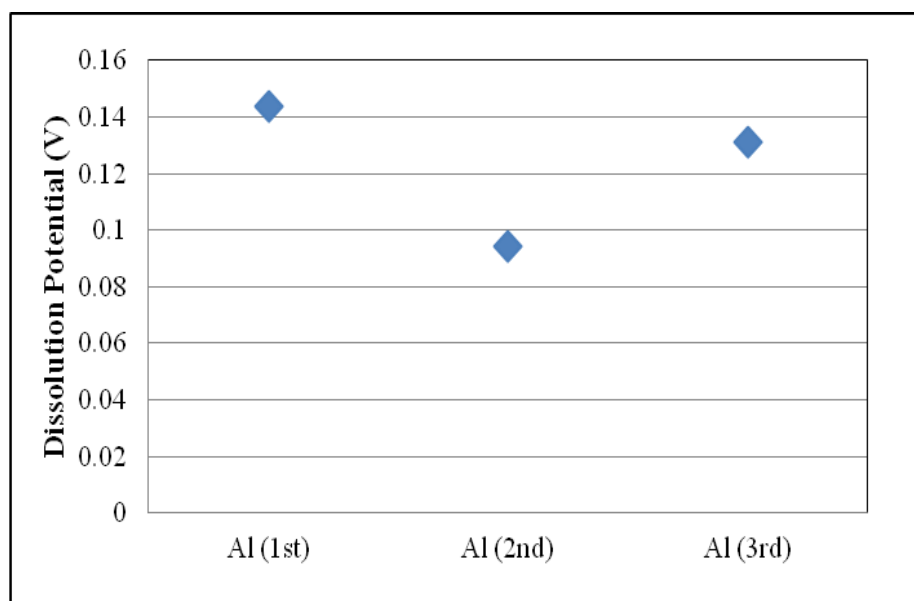
Fig.4. 16 Dissolution potential of 4x4x2 Mg-Al alloy
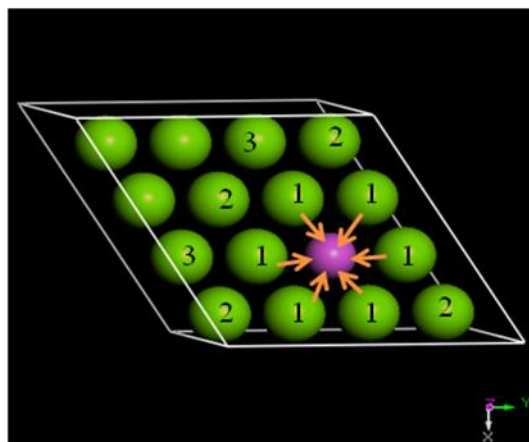
Fig.4. 17 Distortion of atoms due to presence of Al atom in the Mg surface

3. Adsorption energy

A critical step to study the hydrolysis process of materials is to understand the interaction of the surface with the water molecule. The attraction or repulsion of the molecule by the surface illuminates if the surface is ammoniated ageist corrosion. Our calculations are performed by comparison between the energies of the individual reactants and the final products (i.e., combined configuration). The reactants were pure Mg containing a vacuum slab with 30 Å height and one isolated water molecule in a box with the same size as the pure metal slab. To avoid the complication of comparing the water-water and water-surface interactions, only one water molecule was considered in the system. Vertical position of water molecule with different distances for the oxygen atoms from the metal surface was optimized. The adsorption energy was calculated from Eq.4.1. In this equation, E_{ads} is the adsorption energy, E_{total} is the total energy and E_{water} is the energy of isolated water molecule, respectively. In this formula, E_{slab} shows the energy of the slab.

$$E_{ads} = E_{total} - E_{water} - E_{slab} \qquad \text{Eq.4. 13}$$

In the DFT computation, the total energy of the system is dependent upon the initial position of the water molecule. In other words, depending on the accuracy of the first estimation, the total energy calculation for the system is converged toward the equilibrium case. Therefore, the final position of the oxygen atom and accordingly the water molecule and the adsorption energy of the system are determined from a function of the initial position of the water molecule. Also, depending on the initial position of the water molecule, the attraction or repulsion may be favorable.

3.1 Water adsorption on pure Mg surface

Since the basal plane is considered as the most stable plane and it is one of the habit crystallographic planes, the water adsorption phenomena prediction was primarily based on the DFT total energy calculations for slab systems with basal planes. One of the critical parameters to estimate the water adsorption behavior of the material is the position of the water molecule compared to the surface. Depending on this position, the surface may attract or repel the molecule. To find the equilibrium position of water molecule to the surface, two sets of computations were performed. The first computation concentrates on the vertical position of the water molecule and the distance of the water molecule from the metallic surface, and the second one is based on the in-plane position (i.e., x- and y-positions) of the molecule. A vertical V shape configuration for the water molecule was considered, and the atomic position of oxygen (O atom) as the closest atom to the surface was used as the reference to find the equilibrium position of the molecule.

For calculating the vertical equilibrium distance, the initial distances for the O atom and the surface were chosen to be 0.5, 1, 2, 3 and 6 Å. According to Table 4.3 and extrapolating the result in Fig.4.18, there is a critical distance from the surface of the Mg.

If the water molecule approaches to the surface (closer than the equilibrium distance with the lowest energy), due to the repulsion from the nucleus, the relative energy rises to high positive values resulting in instability of the system, which in turn pushes the molecule away. On the other hand, maintaining large distance from the surface neutralizes the repulsion and attraction between the surface and water, causing a zero relative energy (i.e., no interaction for the molecule and the surface). In between these two cases, there is an equilibrium distance which has the lowest possible relative energy. From the graph of Fig.4.18, it is considered that the equilibrium distance for the water molecule from the surface is about 1.33 Å. In other words, if the water molecule takes a Z position close enough to 1.33 Å from the Mg surface the most stable position and the highest adsorption tendency would be reached. For Z coordinates less than this value, for instance 0.5 Å, the surfaces repels the water molecule, and on the other hand, if the Z distance is large enough, for example about 20Å, the surface does not interact with the water molecule and the relative energy becomes zero which is similar to the case that the water molecule and the surface are in isolated condition with no effect on each other.

Table 4.3 Initial and final position and the adsorption energy of the water molecule on the Mg surface

Initial Z	Final Z	E_{ads} (eV)
6	5.30042132	-0.11096818
3	2.79226747	-0.146642141
2	1.47583231	-0.474893048
1	1.3300611	-0.486049715
0.5	1.3408082	-0.468500074
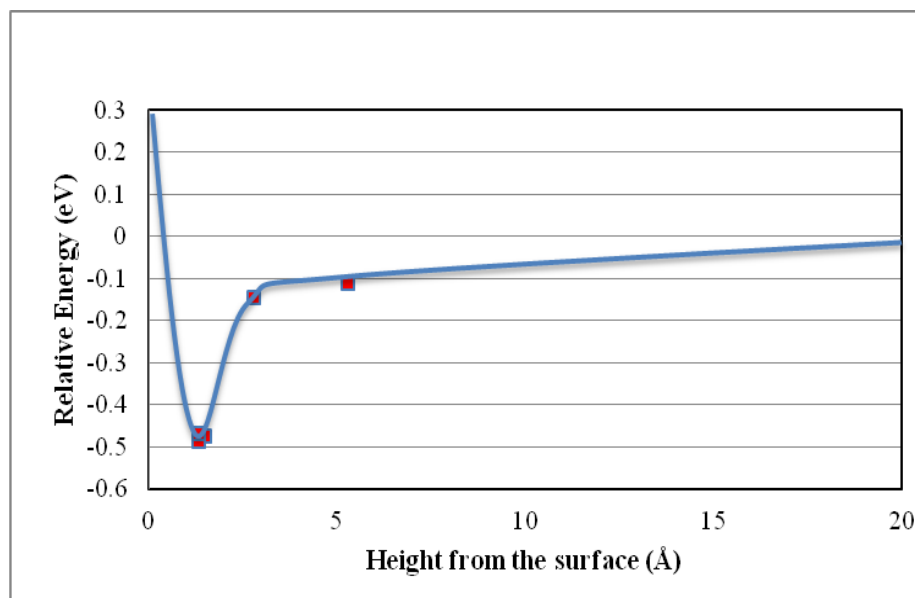
Fig.4. 18 Adsorption energy for Mg surface and water molecule

Next, we examined the changes of the Density of States (DOS) for the water adsorption computations. The blue line in Fig.4.19 represents the distribution of the energy of the electrons in isolated water molecule. The distribution of energy for electrons contains a wide range of energies but the density of electrons per unit energy is not high, with numerical values less than 200 electrons/Ha. On the other hand, the electrons in the pure Mg show a narrow range of energies with higher density of electrons up to 500 electron /Ha. The data for pure Mg is marked with red color in the same graph. These two pure systems have been combined to study the effect of adsorption on DOS, and the results for two different Z positions (2.79 Å in blue color and 1.36 Å in red color) have been reported in Fig.4.20.
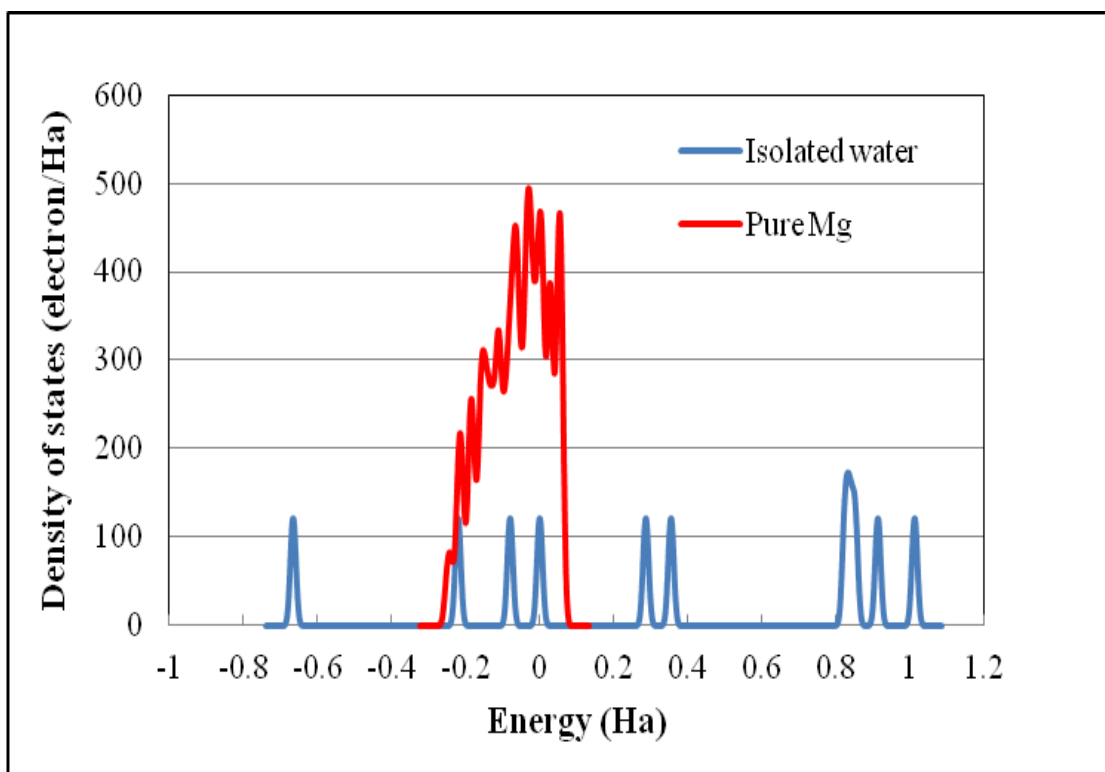
Fig.4. 19 DOS of isolated water molecule and pure Mg
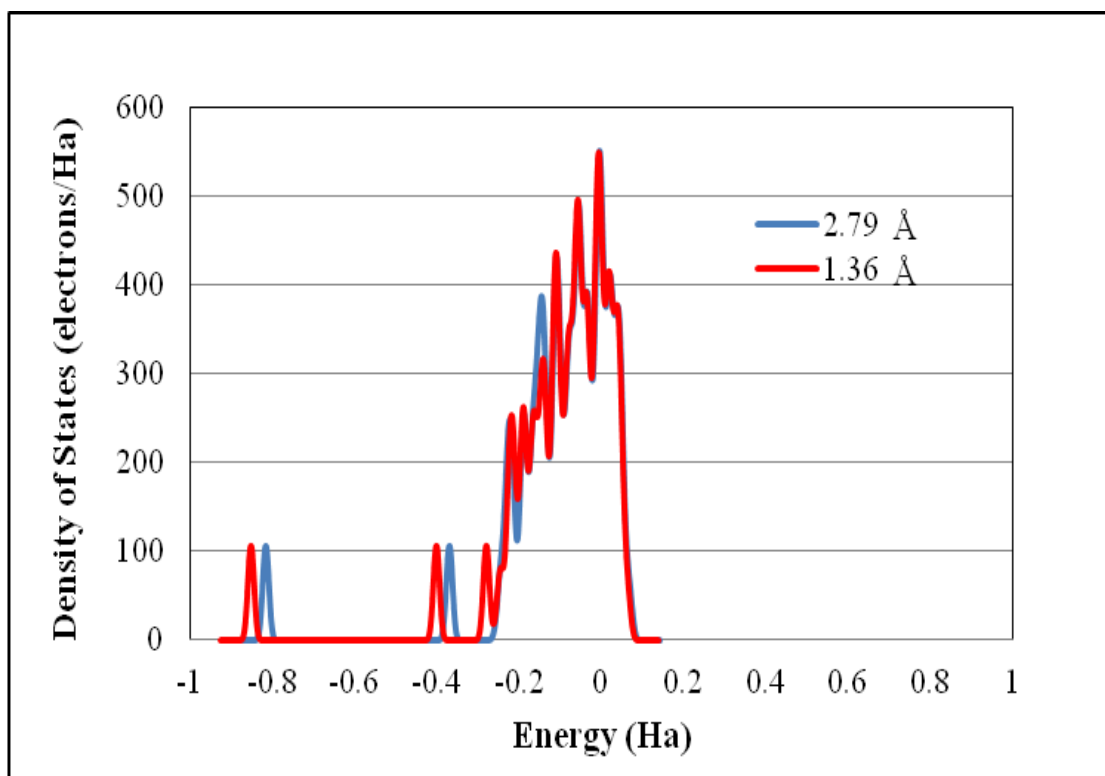
Fig.4. 20 DOS of the water adsorption after interaction

Comparison of Fig.4.19 and Fig.4.20 clarifies that after mixing water and Mg, high energy peaks from the isolated water molecule disappear. Interaction of the water molecule and the metallic surface also eliminates the peaks from electrons with high energies by sending those electrons to lower energy states and increasing the density of electrons in lower energy levels. Such changes in DOS confirm the tendency for adsorbing the water molecule.

As shown in Fig.4.20, when the molecule position gets close to the equilibrium position, the energy distribution of electrons exhibit the combined behavior of peaks from the isolated water molecule and the dry metallic surface. This graph also shows a slight shift for the peaks toward lower energy states for the water molecule when it is positioned closer to the surface. Therefore, it is thought that when the water molecule gets close to the surface (1.36 Å); the configuration becomes more favorable compared to the isolated case, as a result of number of electrons with low energies states. Presence of more peaks in low energy regions for the Z position of 1.39 Å compared to 2.79 Å supports this explanation as well.

3.2 Water adsorption on Mg alloys

As it was mentioned before, the vertical position of the water molecule compared with the metallic surface is a critical parameter to estimate the behavior of the system. The optimized vertical position of the water molecule was discussed in the previous sections. In this sub-section, we compare the horizontal movement of the water molecule on top of the surface and describe the influence of alloying elements in these interactions. Starting from the equilibrium vertical distance as constant (Z=1.33 Å), the water molecule was located on top of one Mg atom on the surface named as position 1 and also

in a site in between the alloying atom and two Mg atoms called as position 2. The positions of water molecule atoms, for these two cases have been presented in Table4.4 and Fig.4.21 shows the top view for these positions.
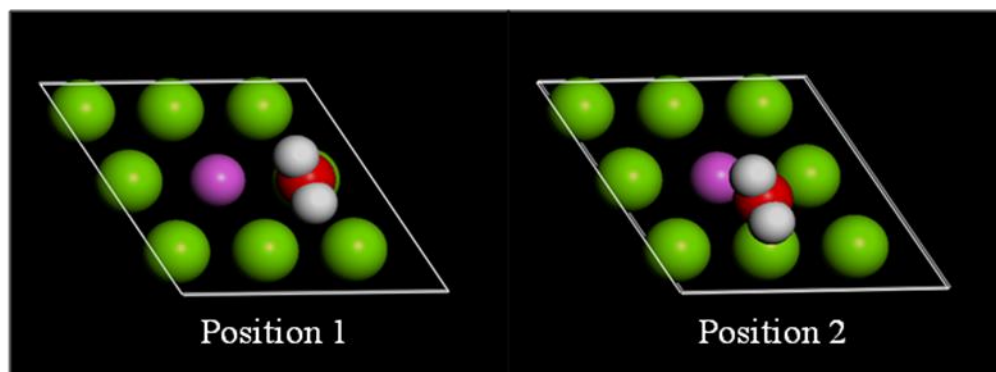
Fig.4. 21 top view for position of water molecule for an adsorption process

Table 4. 4 Position of water molecule for adsorption process

	Position 1			Position 2		
	Oxygen	Hydrogen 1	Hydrogen 2	Oxygen	Hydrogen 1	Hydrogen 2
x	2.0079	1.85706	2.22174	3.72	3.5696	3.9343
y	3.1611	2.26626	4.04182	3.045	2.1498	3.9253
z	1.33	1.96923	1.97086	1.33	1.9692	1.9709

Results presented in Fig.4.22 show that, comparing the energy for the pure Mg when the water molecule is in position 1 and position 2, the degrees of attraction from the surface for the water molecule are different. The water molecule prefers position 2 for adsorption rather than position 1 because the energy of the system is lower when it is located at position 2. For the pure Mg system, adsorption of water molecule is more probable when the molecule is located in the area between atoms. The reason for this may

be the difference in the electronegativity of Mg and the oxygen atom that is equal to 2.2. As a result of such large difference in the electronegativity, the water molecule may be adsorbed if it is close enough to the surface atoms. Comparing position 1 and 2 shows that when the water molecule (O atom) is located in a site similar to position 2, the O atom is under attraction of three atoms, while in position 1, only one surface atom is close to the O atom to attract it. Consequently, in position 2 there is more attraction for the water molecule compare to position 1.

When there is an alloying element on the surface of the metal, adsorption energy is influenced by the nature of doped atom. Comparing the trend of results for position 1 in Fig. 4.22 with the surface energy from Fig.4.4 confirms the relationship between the surface energy and the water adsorption; surfaces with higher stability show less attraction for the water molecule and vice versa. In this condition, the surface with Y doping has the highest attraction for the water molecule with relative energy equal to -0.38 eV. The surface containing Al shows relatively high attraction for the water molecule as well due to its instability. In contrast, the Zn and Ca atoms cause negligible attraction on the surface for the water molecule. As it was mentioned, the reason for this difference in the adsorption behavior of the alloys is related to the same valance number of the alloying atom with Mg and the resultant stability of the surface. Although the trend seems to be the same for the Mg alloy systems irrespective of the water molecule positions, the values of relative energy are different from case by case depending on the positions of the water molecule.

As the second case, we studied a position in between the alloying atom and the two Mg atoms (position 2). The results are given in the bottom of Fig.4.22. The behavior

of alloys follows the same order as previous case (position 1), but at this time, the attraction has increased considerably due to the shift of energies toward more negative values. This means that the tendency for water molecule adsorption becomes stronger if we locate the molecule in between three atoms, regardless of the alloying element type. Therefore, it is considered that this position (position 2) is more stable location of the water molecule for the adsorption process. The differences in the behaviors of water molecule in these two positions indicate that the interaction of the water molecule and the surface is sensitive to the site of adsorption, and the position 2 is more favorable for the water molecule adsorption due to the stronger influence of three metallic atoms compared to one metallic atom for position 1.
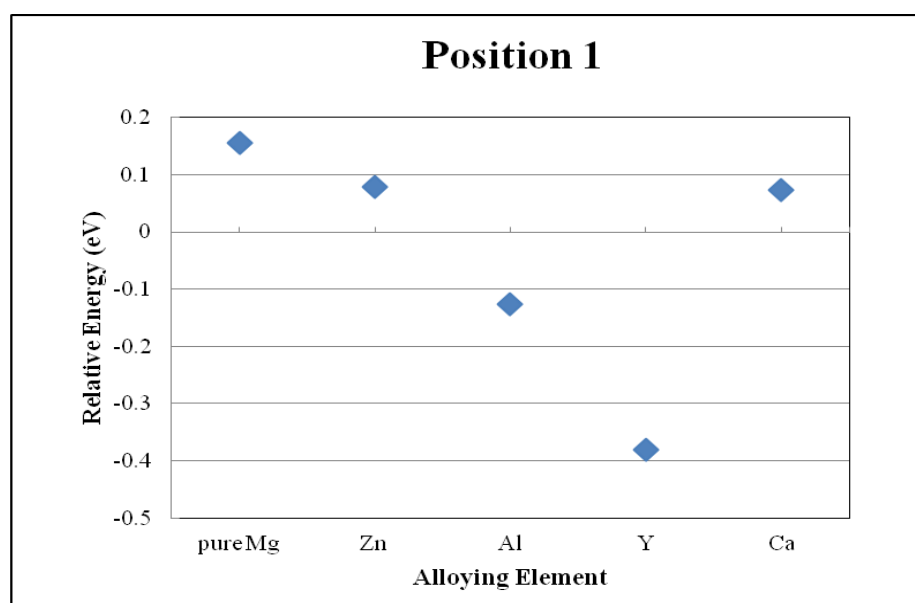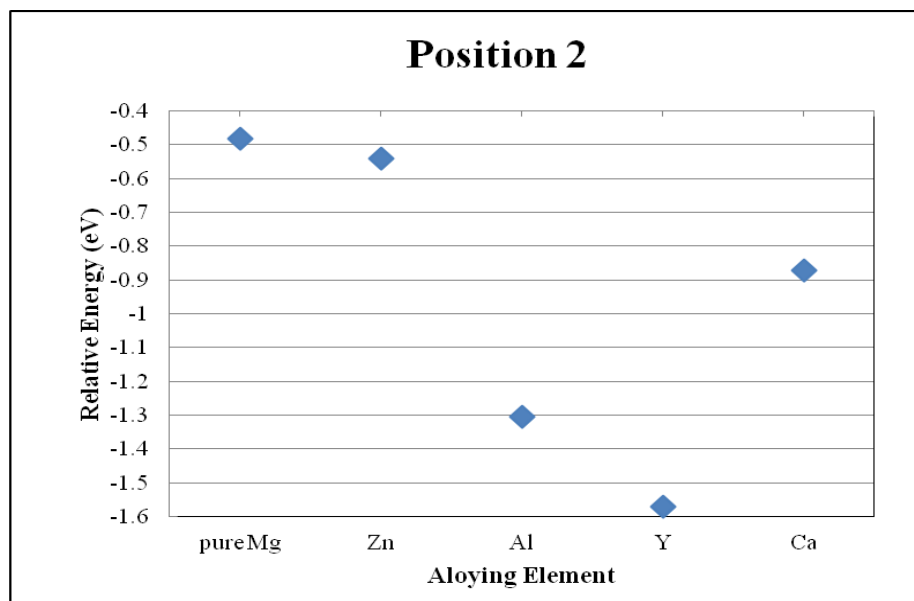
Fig.4. 22 Adsorption energy for Mg alloys with different water molecule positions

3.3 Water adsorption on different crystallographic planes

As a final set of computations, we tested the impacts of crystallographic orientations on the water adsorption. From the surface energy computations, it was found that the crystallographic orientation of the surface has an important role in stability of the system. The slab models in this case were 3x3x2 supercells cleaved to contain basal and prism planes with a 30Å vacuum slab. A water molecule was located in position 2 as Table4.4 (in-between the Mg and alloy atoms) to study the behavior of the surfaces in presence of water molecule. Fig.4.23 shows the result of these calculations. From this figure, it is seen that the basal plane with higher stability has lower tendency to absorb the water molecule, while the loosely packed prism plane more strongly attracts the water molecule toward itself. Thus, it is clear that the adsorption energy has a reverse relationship with the surface energy of the system; the basal plane has lower surface energy and a high stability that results in a weaker attraction for the water molecule, and consequently, lower hydrogen evolution and lower corrosion rate compared to the prism

plane. This result also has agreement with experimental work by Song et al. (128) that reported lower hydrogen evolution for the densely packed plane. Note that the impact of surface orientation on the adsorption energy is not as high as that of Y or Al, but it is comparable to the effect of Ca (see Fig.4.22 position 2 case).
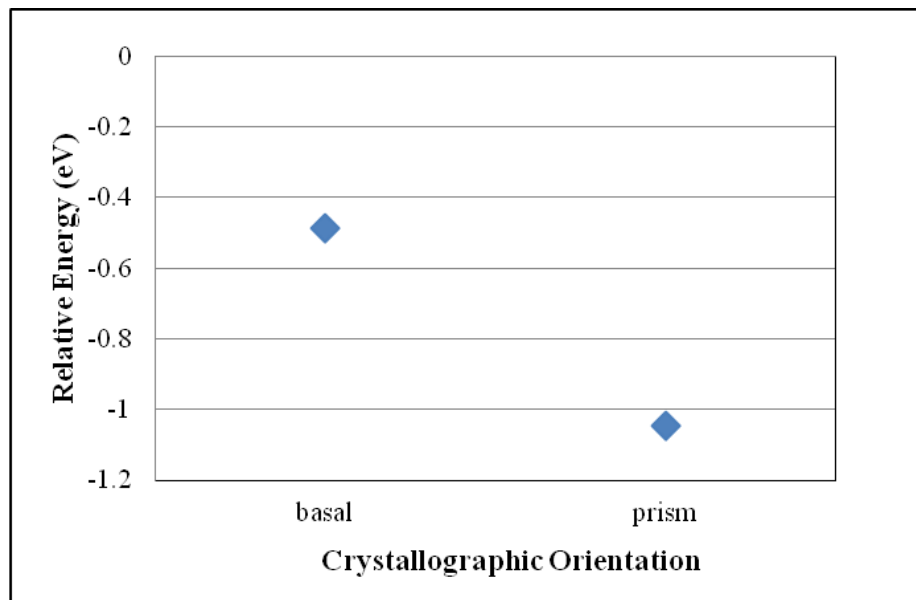
Fig.4. 23 Water adsorption energies from the Mg systems with different crystallographic orientations

Chapter 5: Summary

In the current thesis, we address the corrosion and/or degradation rate of biodegradable Mg-based medical devices in biological environment as the main limitation for their biomedical applications. Especially, we focused on the development of the atomistic DFT computational model to study the initial hydrolysis of Mg/Mg alloys. It is widely recognized that the corrosion behavior of the Mg-based material is strongly influenced by the composition and the crystallography of the system. In this work, the impacts of these factors were studied using i) the surface energy, ii) the dissolution potential, and iii) the tendency of the surface for adsorbing the water molecule, since they are considered as one of the most important properties in the initial hydrolysis degradation behavior.

The surface crystallographic orientations of the Mg/Mg alloy system were chosen to be basal (0001), prism $(10\bar{1}0)$, and pyramidal $(\bar{1}01\bar{1})$ planes as they represent the most common indices in the hexagonal structures. The model indicated a positive relationship between the density of atoms on the surface and the stability of the system; for example, the surface energy of the basal plane with the highest atomic density was found to be the smallest value, resulting in the highest stability for this plane. The prism and the pyramidal planes showed relatively lower stability due to their smaller number of atoms on the surface. By comparing the surface energy results from the computational model and the previous experimental observations, the ranges of proportionality coefficient in the Tafel equation were extrapolated. It was also found that the presence of alloying elements on the surface layer of pure Mg influences the surface energy, the dissolution

behavior, and also the interaction of the surface with the water molecule. Mg alloy systems containing Al, Zn, Ca, and Y were tested in our study as they are the most commonly applied alloying elements in Mg systems for biomedical applications. It was explained that the surface energies of these alloy systems can be dependent on the valency, the ionic radius, and also the surface energy of the alloying elements. It is thought that the atoms with different valency from the Mg ions cause instability in the surface of Mg, and the ionic radius of the alloying atom and their elemental surface energies are other parameters influencing the stability.

The results from water adsorption process indicated that the more stable surfaces have fewer tendencies to absorb the water molecule. By introducing a water molecule on the metal surface, the energies of the system were lowered with the order of Y, Al, Ca, and Zn. From the water molecule adsorption calculations, the lowest energy configurations of all of the alloy systems with a water molecule were identified. For all of the Mg-based systems examined in our work, it was observed that there is a reverse relationship between the surface stability and the water adsorption tendency. It seems that surfaces with lower stabilities approach the equilibrium by adsorbing the water molecule. It was explained that due to the relatively large differences between the electronegativity of the oxygen atom and the metallic atoms, it is likely that the stronger attraction will occur between the water molecule and the surface atoms. It was found that the presence of oxygen atom of the water molecule on top of three metallic atom on the surface magnifies the attracting forces and this results in stronger water adsorption compared to a position that has only on metallic atom close to the oxygen atom. Therefore, for position of the water molecule on the metal surface seems to be an important parameter.

It was also found that although the surface containing Al exhibits relatively higher surface energy compared with Ca and Y, it was calculated that the dissolution potential of Mg-Al systems is the highest, which means that removing the atoms from the surface of this alloy is more difficult compared to the other cases. The reason for this resistance may be the small ionic radius of Al. In other words, due to the small size of the Al atom, its first nearest neighbors on the surface will move toward it, and such a positive distortion gives rise to the displacement of atoms closer to each other that causes less tendency of these atoms for dissolution. From these findings, it is thought that the surface energy cannot solely determine the dissolution behaviors of Mg alloys.

The developed model is only applicable for the small systems due to the general limitation of DFT computational technique for the size of the system. The model does not consider the formation of hydroxide layer, and the model only focuses on the initial mechanism of hydrolysis. Further, there is a need to develop a more comprehensive model to include the pitting and/or galvanic corrosion phenomena in addition to hydrolysis. As a future work, we will conduct a more advanced study on the combination effect of different alloying elements and also the effect of combining the alloying elements with crystallographic orientation. It is expected that the theory that includes the interaction of the water molecule and the proteins present in the body along with the hydroxide layer formation on the surface of the metal also can lead to better understanding of the corrosion behavior of Mg alloys and to find the optimized composition for the Mg alloy. Finally, we also plan to develop a larger scale model (i.e., meso-scale model) or multi-scale model to integrate the two major mechanisms of Mg degradation, hydrolysis and galvanic corrosion.

The findings, limitations, and future work of the current thesis are summarized as follows.

<u>Findings</u>

1. Surface energy and Mg corrosion/dissolution

- The basal plane shows the lowest surface energy in Mg systems.

- The proportionality coefficient in the Tafel expression is in the range of 0.007 and 0.049.

- The Mg alloy systems containing Al and Y show higher surface energies than pure Mg materials, and the Mg alloys incorporating Zn show lower surface energy.

- When the contents of alloying element is sufficiently low (i.e., less than 5 at.%) and the proportionality coefficient in the Tafel expression is assumed as a constant, the impact of surface orientation on the dissolution behavior is higher than that of alloying element.

2. Dissolution potential and Mg corrosion/dissolution

- Mg-Al alloy shows the highest dissolution potential difference compared to the pure Mg while this difference for Mg-Y system is the lowest; addition of Ca and Zn do not cause considerable changes on dissolution potential from the pure Mg system.

- In the Mg alloy system containing Al, dissolution of Mg atoms is much easier compared to that of the alloying atom (Al).

- In the Mg-Al system, the first nearest neighbors of the alloying atom are the most difficult atoms to remove, followed by the third and then the second nearest neighbors on the alloy surface.

3. Water adsorption and Mg corrosion/dissolution

- The trend of water adsorption behavior is consistent with the surface energy changes in the Mg-alloy systems. The lowest water adsorption energy was expected in the system (i.e., Mg-Y system) with the highest surface energy, and vice versa.

- There is an equilibrium height for the water molecule from the metallic surface equal to 1.33Å (when the in-plane position of water molecule is fixed as the center of the surface Mg atom) that results in the lowest energy of -0.48 eV for the system considered in our work.

- If the water molecule is located in a height more than 20 Å from the surface the water molecule and the metallic surface show no interaction with each other.

- There is a lower tendency of water adsorption when the water molecule is positioned on the top of surface Mg atom compared with the center of three surface atoms.

- The basal plane adsorbs the water molecule less than the prism plane.

Limitations

- The model is limited to small systems due to the general nature of DFT calculations.

- The model does not address the effects of multi-element alloying.

- The formation of hydroxides has not been considered in the computations.

- The model is not useful to describe more complicated forms of corrosion mechanisms such as pitting and galvanic corrosion

Future work

- Develop a model to study the combination effect of multi-element alloying and also the combination effect of crystallographic orientation and alloying elements.

- Study the behavior of the Mg surface after the formation of the various types of hydroxide layer.

- Develop a multi-scale model that considers the effect of both hydrolysis and galvanic corrosion mechanisms.

- Study the interaction of the surface with more complicated proteins (i.e., protein adsorption) existing in the adequate physiological environment.

References

1. Hermawan, Hendra. *Biodegradable Metals From Concept to Applications.* Bandung : Springer, 2012.

2. *Control of biodegredation of biocopmatable magnesium alloys.* Song, Guang Ling. Brisbane : Corrosion Science, 2007, Vol. 49, pp. 1696-1701.

3. *Corrosion Mechanisms of Magnesum Alloys.* Song, Guang Ling and Atrens, Andrej. s.l. : Advanced Engineering Meterials, 1999, Vol. 1, pp. 11-33. 1.

4. *Magnesium and its alloys as orthopedic biomaterials: A review.* Staiger, Mark p., et al. s.l. : Biomaterials, 2006, Vol. 27, pp. 1728-1734.

5. *A new mode of arresting nasal and uterine hamorrhage.* Huse, Edward C. Rockford : The Chicago medical journal and examiner, 1878, Vol. 37, pp. 171-172.

6. *The history of biodegradable magnesium implants: A review.* Witte, Frank. Hannover : Acta Biomaterialia, 2010, Vol. 6, pp. 1680-1692.

7. *The resorbing metallic alloy 'Ostenthezit' as material for fastening broken bone.* VV, Troitskii and Tsitrin, DN. s.l. : Khirurgiia, 1944, Vol. 8, pp. 41-44.

8. *In vivo corrosion of four magnesium alloys and the associated bone response.* Witte, F., et al. s.l. : Biomaterials, 2005, Vol. 26, pp. 3557-3563.

9. *A survey of bio-corrosion rates of magnesium alloys.* Kirkland, N. T., et al. s.l. : Corrosion Science, 2010, Vol. 52, pp. 287-291.

10. *Degradable biomaterials based on magnesium corrosion.* Witte, Frank, et al. s.l. : Current opinion in solid state and materials science, 2008, Vol. 12, pp. 63-72.

11. *Preparation and properties of high purity Mg-Y biomaterials.* Peng, Quiming, et al. s.l. : Biomaterials, 2010, Vol. 31, pp. 398-403.

12. *In vitro corrosion and biocompatibility of binary magnesium alloys.* Gu, Xuenan, et al. s.l. : Biomaterials, 2009, Vol. 30, pp. 484-498.

13. *Corrosion mechanism applicable to biodegradable magnesium implants.* Atrens, Andrej, Liu, Ming and Nor Ishida, Zainal Abidin. s.l. : Materials Science and Engineering B, 2011.

14. *In Vitro biodegrdation behavior of magnesium and magnesium alloy.* Wang, Hao and Shi, Zhiming. s.l. : Journal of biomedical materials research B: Applied biomaterials, 2010, Vol. 98B, pp. 203-209.

15. *Ion release from magneium materials in physiological solutions under different oxygen tensions.* Feyerabend, Frank, et al. s.l. : J of Mater Med, 2012, Vol. 23, pp. 9-24.

16. Schneck, DJ. *The niomedical engineering handbook.* s.l. : CRC press LLC, 2000.

17. Black, J. *Biological performance of materials.* s.l. : Plenum Press.

18. Niinomi, M. *metals for biomedical engineering hand book.* Cambridge : Woodhead Publishing, 2010.

19. *Buffer-regulated biocorrosion of pure magnesium.* Kirkland, Nicholas T., et al. s.l. : Journal of material science, 2012, Vol. 23, pp. 283-291.

20. *Coronary-Artery Stents.* Serruys, Patrick W., Kutryk, Michael J. B. and Ong, Andrew T. L. s.l. : The new England Journal of Medicine, 2006, pp. 483-495.

21. *Temporary scaffolding of coronary arteries with bioabsorbable magnesium stents: a prospective, non-randomised multicentre trial.* Erbel, Raimund, et al. s.l. : The lancet, 2007, Vol. 369, pp. 1869-1875.

22. *Safty and Effecacy of Bioansorbable Magnesium Alloy Stent in Porcine Coronary Arteries.* Waksman, Ron, et al. s.l. : Catheterization and Cardiovascular Interventions, 2006, Vol. 68, pp. 607-617.

23. *Drug-Eluting Bioabsorbable Magnesium Stent.* Di Mario, Carlo, et al. s.l. : Journal of Interventional Cardiology, 2004, Vol. 17, pp. 391-395. 6.

24. *Biocorrosion of magnesium alloys: a new principle in cardiovascular implant technology.* Heublein, B., et al. s.l. : Magnesium alloys for cardiovascular implants, 2003, pp. 651-656.

25. *Promise and challenges of bioabsorbable stents.* Waksman, Ron. s.l. : Catheterization and Cardiovascular Interventions, 2007, Vol. 70, pp. 407-414.

26. *Intracoronary stenting anticoagulation accomplishe with intravascular ultrasound guidance.* Colombo, Antonio, et al. s.l. : Circulation, 1995.

27. *Long-term biocompatibility of a corrodible perpheral iron stent in the porcine descending aorta.* Peuster, Matthias, et al. s.l. : Biomaterials , 2006, Vol. 27.

28. *Short-Term Effect of Biocorrodible Iron Stents in Porcine Coronary Arteries.* Waksman, Ron, et al. s.l. : Journal of Interventional Cardiology, 2007, Vol. 21.

29. *Temporary scaffolding of coronary arteries with bioabsorbable magnesium stents: a prospective, non-randomised multicentre trail.* Erbel, Raimund, et al. Essen : The lancet, 2007, Vol. 369, pp. 1869-1875.

30. *Tissue biocompatibility of new biodegradable drug-eluting stent materials.* Uurto, Ilka, et al. s.l. : Journal of material science, 2007, Vol. 18, pp. 1543-1547.

31. *Influence of surface texture and charge on the biocompatibility of endovascular stents.* Hehrlein, C, et al. 7, s.l. : Coron Artery, 1995, Vol. 6, pp. 581-586.

32. *Coronary stents: A materials prospective.* Mani, Gopinath, et al. s.l. : Biomaterials, 2007, Vol. 28, pp. 1689-1710.

33. *Effect of pH on the in vitro corrosion rate of magnesium degradable implant material.* Ng, W. F., Chiu, K. Y. and Cheng, F. T. s.l. : Materials science and engineering C, 2010, Vol. 30, pp. 898-903.

34. *Comparative study of fluoride conversion coatings formed on biodegradable powder metallurgy Mg: The effect of chlorides at physiological level.* Pereda, M. D., et al. s.l. : MAterials Science and Engineering C, 2011, Vol. 31, pp. 858-865.

35. *http://www.indiamart.com/saliuspharma/medical-devices.html.*

36. *Corrosion of magnesium alloy AZ31 screws is dependent on the implantation site.* Willbold, E., et al. s.l. : Materials Science and engineering, 2011, Vol. 176, pp. 1835-1840.

37. *Electrochemical deposition and evaluation of electrically conductive polymer coating on biodegradable magnesium implants for neural applications.* Sebaa, Meriam A., Dhillon, Shan and Liu, Huinan. s.l. : Journal of material science, 2012, Vol. 24, pp. 307-316.

38. *Understanding magnesium corrosion a framework for improved alloy performance.* Song, Guangling and Atrens, Andrej. 12, s.l. : Advance Engineering Materials, 2003, Vol. 5, pp. 837-858.

39. *Corrosion behavior of AZ21, AZ501, and AZ91 in sodium chloride.* Song, Guangling, et al. 10, s.l. : Corrosion science, 1998, Vol. 40, pp. 1769-1791.

40. Corrosion resistance of magnesium alloys. *ASM Handbook.* s.l. : ASM International, 2003, Vol. 13A.

41. *Hydrogen embrittlement of magnesium and magnesium alloys: A review.* Kappes, Mariano, Iannuzzi, Mariano and Carranza, Richardo M. 4, s.l. : Journal of Electrochemica; Society, 2013, Vol. 160, pp. 168-178.

42. *The potential-pH diagram of the magnesium water system.* Perrault, G. G. 1, s.l. : Journal of electroanalytical chemistry, 1974, Vol. 51, pp. 107-119.

43. *The anodic dissolution of magnesium in chloride and sulphate solutions.* Song, G., et al. 10, s.l. : Corrosion Science, 1997, Vol. 39, pp. 1981-2004.

44. *Chemical surface alteration of biodegradable magnesium exposed to corrosion media.* Willumeit, Regine, et al. s.l. : Acta Biomaterialia, 2011, Vol. 7, pp. 2704-2715.

45. Katarzyna, Braszczynska-Malika. Precipitates of γ-Mg17Al12 Phase in AZ91 Alloy. [book auth.] Frank Czerwinski. *Magnesium alloys- Design, Properties.* s.l. : In Tech, 2011.

46. *The negative difference effect of magnesium and of the AZ91 alloy in chloride and stannate-containing solutions.* Thomaz, T. R., et al. s.l. : Corrosion science, 2010, Vol. 52, pp. 2235-2243.

47. *A new theory for the negative difference effect in magnesium corrosion.* Bender, S., et al. 8, s.l. : Materials and corrosion, 2012, Vol. 63, pp. 707-712.

48. *The negative-Difference Effect during the Localized Corrosion of Magnesium and the AZ91HP Alloy.* Weber, Cristina R., Knornschild, Gerhard and Dick, Luis F. P. 4, s.l. : J. Braz. Chem. Soc, 2003, Vol. 14, pp. 584-593.

49. *Influence of microstructure onthe corrosion of diecast AZ91D.* Song, G. L., Atrens, A. and Dargusch, M. 2, s.l. : Corrosion Science, 1999, Vol. 41, pp. 249-273.

50. *The Y-doped MgZnCa alloys with ultrahigh specific strength and good corrosion resistance in simulated body fluid.* Wang, J. F., et al. s.l. : Materials Letters, 2012, Vol. 81, pp. 112-114.

51. *Investigation of the mechanical properties and the corrosion behavior of low alloyed magnesium-calcium alloys for use as absorbable biomaterial in the implant technique.* Hassel, TH, et al. Montreal, Quebec, Canada : Magnesium technology in the global age, 45th annual conference of metallurgists of CIM, 2006. pp. 359-370.

52. *In-vitro dissolution of magnesium-calcium binary alloys: Clarifying the unique role of calcium additions in bioresorbable magnesium implant alloys.* Kirkland, N. T., et al. 1, s.l. : Journal of biomedical materials research B: Applied biomaterials, 2010, Vol. 95B, pp. 91-100.

53. *In vitro degradation and cytotoxicity of Mg/Ca composites produced by powder metallurgy.* Zheng, Y. F., et al. s.l. : Acta biomaterialia, 2010, Vol. 6, pp. 1783-1791.

54. *Influence of Ca on the corrosion properties of magnesium for biomaterials.* Kim, Woo-Cheol, et al. s.l. : Materials Letters, 2008, Vol. 62, pp. 4146-4148.

55. *Mechanical properties, degradation performance and cytotoxicity of Mg-Zn-Ca biomedical alloys with different compositions.* Zhang, Baoping, et al. s.l. : Materials science and engineering C, 2011, Vol. 31, pp. 1667-1673.

56. *Rapid degradation of biomedical magnesium induced by zinc ion implantation.* Wu, Guosong, et al. s.l. : MAterials Letters, 2011, Vol. 65, pp. 661-663.

57. *First-principles studies on alloying and simplified thermodynamic aqueous chemical stability of calcium-, zinc-, aluminum-, yttrium-, and iron-doped magnesium alloys.* Velikokhatnyi, Oleg I and Kumta, Prashant N. s.l. : Acta Biomaterialia, 2010, Vol. 6, pp. 1698-1704.

58. Avedesian, M. M. and Baker, H. *ASM Specialty handbook, Magnesium and magnesium alloy.* s.l. : ASM International, 1999.

59. *Growth of zinc phosphate coating on AZ91D magnesium alloy.* Li, G. Y., et al. s.l. : Surface & Coating technology, 2006, Vol. 201, pp. 1814-1820.

60. *Microstructure, mechanical and corrosion properties and biocompatibility of Mg-Zn-Mn alloys for biomedical application.* Zhang, Erlin, et al. s.l. : Materials Science and Engineering C, 2009, Vol. 29, pp. 987-993.

61. *Phosphate coating on magnesium alloy AM60 part 1: study of the formation and the growth of zinc phospate films.* Kouisni, L., et al. 1, s.l. : Surface coating technology, 2004, Vol. 185, pp. 58-67.

62. *Preparation and characterization of a new biomedical Mg-Zn0Ca alloy.* Sun, Yu, et al. s.l. : Materials and Design, 2012, Vol. 34, pp. 58-64.

63. *Corrosion resistance of agesd die cast magnesium alloy AZ91D.* Song, Guangling, Bowles, Amanda L. and StJohn, David H. s.l. : Materials Sceince and Engineering, 2004, Vol. A366.

64. *Understanding magnesium corrosion A framework for improved alloy performance.* Song, Guangling and Atrens, Andrej. 12, s.l. : Advance Engineering Materials, 2003, Vol. 5, pp. 837-858.

65. *Bio-corrosion characterization of Mg-Zn-X (X=Ca, Mn, Si) alloys for biomedical applications.* Rosalbino, F., et al. s.l. : Journal of materials science, 2010 йил, Vol. 21, pp. 1091-1098.

66. *The influence of yttrium (Y) on the corrosion of Mg-Y binary alloys.* Liu, Ming, et al. s.l. : Corrosion science, 2010, Vol. 52, pp. 3687-3701.

67. *Corrosion behavior of rapidly solidified MgNd and MgY.* Krishnamutrhy, S., et al. 1-2, s.l. : Materials Science and Engineering, 1988, Vol. 99, pp. 507-511.

68. *Passivity behavior of melt-spun Mg-Y alloys.* Yao, H. B., Li, Y. and Wee, A. T. S. 28, s.l. : Electrochimica acta, 2003, Vol. 48, pp. 4197-4204.

69. *The role of microstructure in localized corrosion of magnesium alloys.* Singh Raman, R. K. s.l. : Metallurgical and materials transactions A, 2004, Vol. 35A, pp. 2525-2531.

70. Song, Guang-Ling, Mishra, Raja and Xu, ZhenQing. *Crystallographic orientation and electrochemical activity of AZ31 Mg alloy.* s.l. : Electrochemistry Communications, 2010. pp. 1009-1012.

71. *Effect of mischmetal on the corrosion properties of Mg-5Al alloy.* Nam, N. D., et al. s.l. : Corrosion Science, 2009, pp. 2942-2949.

72. *Influence of texture on corrosion rate of AZ31 Mg alloy in 3.5 wt% NaCl.* Xin, Renlong, et al. s.l. : Materials and Design, 2011 йил, Vol. 32, pp. 4548-4552.

73. *The effect of crystallographic orientaion on the active corrosion of pure magnesium.* Liu, Ming, et al. s.l. : Scripta Materialia, 2008, Vol. 58, pp. 421-424.

74. *Texture effect on corrosion behavior of AZ31 Mg alloy in simulated physiological environment.* Xin, Renlong, et al. s.l. : Materials Letters, 2012, Vol. 72, pp. 1-4.

75. *Nitrogen adsorption and thin surface nitrides on Cu (111) from firdt-principles.* Soon, Aloysius, et al. s.l. : Surface Science, 2007, Vol. 601, pp. 4775-4785.

76. *Characterization and corrosion studies of fluride conversion coating on degradable Mg implants.* Chiu, K. Y., et al. s.l. : Surface & Coating Technology, 2007, Vol. 202, pp. 590-598.

77. *Corrosion behaviour of AZ and ZA magnesium alloys in alkaline chloride media.* Oteyaka, Mustafa. O, Ghali, Edward and Tremblay, Real. s.l. : International journal of corrosion, 2012.

78. *Impact of microgalvanic corrosion on the degradation morphology of WE43 and pure magnesium under exposure to simulated body fluid.* Kalb, H., Rzany, A. and Hensel, B. s.l. : Corrosion Science, 2012, Vol. 57, pp. 122-130.

79. *Comparative study on corrosion behaviour of pure Mg and WE43 alloy in static, stirring and flowing Hank's solution.* Li, N., et al. s.l. : Corrosion engineering, Science and technology, 2002, Vol. 47, pp. 346-351.

80. *Corrosion behavior of Mg, AZ31, and AZ91 alloys in dilute NaCl solutions.* Wang, Lei, Shinohara, Tadashi and Zhang, Bo-Ping. s.l. : Journal of solid state electrochem, 2010, Vol. 14, pp. 1897-1907.

81. *Continuum damage model for bioresorbable magnesium alloy devices-Application to coronary stents.* Gastaldi, D., et al. s.l. : Journal of the mechanical behavior of biomedical materials, 2011, Vol. 4, pp. 352-365.

82. *The effect of pre-processing and grain structure on the bio-corrosion and fatigue resistance of magnesium alloy AZ31.* Wang, Hao, et al. s.l. : Advanced engineering materials, 2007, Vol. 9, pp. 967-972. 11.

83. *Effect of calcium content on the microstructure hardness and in vitro corrosion behavior of biodegradable Mg-Ca binary alloy.* Eslami Harandi, Shervin, et al. 1, s.l. : Materials research, 2013, Vol. 16, pp. 11-18.

84. *Development and biocompatibility of a novel corrodible fluoride-coated magnesium-calcium alloy with improved degradation kinetics and adequate mechanical properties for cardiovascular applications.* Drynda, Andreas, et al. 2, s.l. : Journal of biomedical materials research partA, 2009, Vol. 39A, pp. 763-775.

85. *Biomecanical testing and degradation analysis of MgCa0.8 alloy screw: A comparative in vivo study in rabbits.* Erdmann, Nina, et al. 3, s.l. : Acta biomaterialia, 2011, Vol. 7, pp. 1421-1428.

86. *Properties of porous magnesium preoared by powder metallurgy.* Capek, Jaroslav and Vojtech, Dalibor. s.l. : Materials science and engineering C, 2013, Vol. 33, pp. 564-569.

87. *Biodegradable magnesium scaffolds: Part I: Appropriate inflammatory response.* Witte, F., et al. 3, s.l. : journal of biomedical materials research part A, 2007, Vol. 81A, pp. 748-756.

88. *Innovative processing of lotus-type porous magnesium through thermal decomposition of wood.* Mohammadi Zahrani, M., Meratian, M. and Kabiri, Y. s.l. : Materials Letters, 2012, Vol. 85, pp. 14-17.

89. *Degradation and cytotoxicity of lotus-type porous pure magnsium as potential tissue engineering scaffold material.* Gu, X. N., et al. s.l. : Materials Letters, 2010, Vol. 64, pp. 1871-1874.

90. *MGZNCA glasses without clinically observable hydrogen evolution for biodegradable implants.* Zberg, Bruno, Uggowitzer J., Peter and Loffler F., Jorg. s.l. : Nature materials, 2009, pp. 887-891.

91. *Corrosion of, and cellular responses to Mg-Zn-Ca bulk metallic glasses.* Gu, Xuenan, et al. s.l. : Biomaterials, 2010, Vol. 31, pp. 1093-1103.

92. *Surface modification of magnesium alloys developed for bioabsorbable orthopedic implants: A general review.* Wang, Jiali, et al. 6, s.l. : Journal of biomedical materials research. Part B, Applied biomaterials, 2012, Vol. 100, pp. 1691-1701.

93. *Influence of surface modification on the in vitro corrosion rate of magnesium alloy AZ31.* Gray-Munro, Joy E., Seguin, Christine and Strong, Michael. 1, s.l. : Journal of biomedical materials research part A, 2008, Vol. 91A, pp. 221-230.

94. *Effect of acidic etching and fluoride treatment on corrosion performance in Mg alloy AZ91D (MgAlZn).* Turhan, Metehan C., et al. s.l. : Electrochimica Acta, 2009, Vol. 55, pp. 250-257.

95. *Biodegradable poly(lactide-co-glycolide) coating on magnesium alloys for orthopedic applications.* Ostrowski, Nicole J., et al. s.l. : Journal of materials science, 2013, Vol. 24, pp. 85-96.

96. *Fabrication and properties of porous scafold of magnesium phosphate/polycaprolactone biocomposite for bone tissue engineering.* Wu, Fan, et al. 19, s.l. : Applied surface science, 2012, Vol. 258, pp. 7589-7595.

97. *Microstructure of hydroxyapatite-coated magnesium prepared in aqueous solution.* tomozawa, Massanari, Hiromoto, Sachiko and Harada, Yoshitomo. 20, s.l. : Surface coatings technology, 2010, Vol. 204, pp. 3243-3247.

98. Sholl, David S. and Steckel, Janice A. *Density functional theory.* New Jersey : John Wiley & Sons, Inc, 2009.

99. *Density functional calculations of molecular bond energies.* Becke, A. D. s.l. : Journal of chemical physics, 1986, Vol. 84.

100. Szabo, Attila and Ostlund, Neil S. *Modern quantum chemistry introduction to advanced electronic structure theory.* New York : McGraw-Hill, 1989.

101. *Inhomogeneous electron gas.* Hohenberg, P. and Kohn, W. 3B, s.l. : Physical review, 1964, Vol. 136, pp. 864-871.

102. *An all-electron numerical method for solving the local density functional for polyatomic molecules.* Delly, B. 1, s.l. : The journal of chemical physics, 1990, Vol. 92, pp. 508-517.

103. *Generalized Gradient Approximation made simple.* Perdew, John P., Burke, Kieron and Ernzehof, Matthias. s.l. : Physical review, 1996, Vol. 77, pp. 3865-3868. 18.

104. *Self-Consistent equatuion including exchange and correlation effects.* Hikn, W. and Sham, L. J. 4A, s.l. : Physical review, 1965, Vol. 140, pp. 1133-1138.

105. *Self-consistent equations including exchange and correlation effects.* Kohn, W. and Sham, L. J. 4A, s.l. : Physical review, 1965, Vol. 140.

106. *Atoms, moleculs, solids and surfaces: Applications of the generalized gradient approximation for exchange and correlation.* Perdew, John P., et al. 11, s.l. : Physical review B, 1992, Vol. 46, pp. 6671-6687.

107. *Accurate and simple density for the electronic exchange energy: Generalized gradient approximation.* Perdew, John P. and Yue, Wang. 12, s.l. : physical review B, 1986, Vol. 33.

108. *Density functional theory.* Orio, Maylis, Pantazis, Dimitrios A. and Neese, Frank. s.l. : photosynth Res, 2009, Vol. 102, pp. 443-453.

109. *Semiempirical hybrid density functional with perturbation second-order correlation .* Grimme, Stefan. s.l. : The journal of chemical physics, 2006, Vol. 124.

110. *Semiempirical GGA-type density functional constructed with a long-range dispersion correction.* Grimme, Stefan. 15, s.l. : Journal of computational chemistry, 2006, Vol. 27.

111. Sholl, David S. and Steckel, Jnice A. *Density functional theory a practical introduction.* s.l. : John Wiley & Sons, Inc., 2009.

112. *Tight-binding description of the quasipaticle dispersion of graphite and few-layer graphene.* Gruneis, A., et al. s.l. : Physical review B, 2008, Vol. 78.

113. *Interference and k point sampling in the supercell approach to phase coherent transport.* Thygesen, K. S. and Jacobsen, K. W. s.l. : Physical review, 2005, Vol. 72.

114. *Electronic structure, properties and phase stability of inorganic crystals: A pseudopotential plane-wave study.* Milman, V., et al. s.l. : International journal of quantum chemistry, 1999.

115. *Ab initio molecular dynamics of metal surfaces.* Walker, B. G., Molteni, C. and Marzari, N. s.l. : Journal of physics: Condenced matter, 2004.

116. Fiolhais, C., Nogueira, F. and Marques, M. *A primer in density functional theory.* Coimbra : Springer, 2002.

117. *Geometry optimization.* Bernhard Schlegel, H. s.l. : WIREs computational molecular science, 2011.

118. *A computationally feasible DFT/CCSD(T) correction scheme for the description of weakly interacting systems.* Rubs, Miroslav, et al. s.l. : The open chemical physics journal, 2008, Vol. 1, pp. 1-11.

119. *A density functional study on the adsorption of methanethiolate on the (111) surfaces of noble metals.* Akinaga, Yoshinobu, Nakajima, Takahito and Hirao, Kimihiko. 19, s.l. : Journal of chemical physics, 2001, Vol. 114, pp. 8555-8564.

120. *Is CO chemisorbed on Pt anomalous compared with Ni and Pd?An example of surface chemistry dominated by relativistic effects.* Pacchioni, Gianfranco, et al. s.l. : Surface Science, 1997, Vol. 392, pp. 173-184.

121. *Understanding the interaction of water with anatase TiO2 (101) surface from density functional theory calculations.* Zhao, Zongyan, Li, Zhaosheng and Zou, Zhigang. s.l. : Physical letters A, 2011, Vol. 375, pp. 2939-2945.

122. *A theoritical study of water adsorption and decomposition on the low-index stoichiometric anatase TiO2 surface.* Zhao, Zongyan, Li, Zhaosheng and Zou, Zhigang. s.l. : The journal of physical chemistry C, 2012, pp. 7430-7441.

123. *DFT study on surface properties and dissolution trends of Al (100) surfaces doped with Zn, Ga, In, Sn and Pb.* Liu, Jiancai, et al. s.l. : Applied surface science, 2011, Vol. 257, pp. 4004-4009.

124. *Density functional theory predictions of second-order hyperpolarizabilities of metallocenes.* Matsuzawa, Nobuyuki, Seto, Jun'etsu and Dixon, David A. s.l. : Journal of physical chemistry, 1997, Vol. 101, pp. 9391-9398.

125. *Lattice constants and Vrillouin zone overlap in dilute magnesium alloys.* Von Batchelder, F. W. and Raeuchle, R. F. 1, s.l. : Physical review, 1957, Vol. 105, pp. 59-61.

126. *The effect of crystallographic orientation on the active corrosion of pure magnesium.* Liu, Ming, et al. s.l. : Scripta materialia, 2008, Vol. 58, pp. 421-424.

127. De Boer, F. R., et al. *Cohesion in metals transition metal alloys.* s.l. : North-Holand Physics Publishing, 1988. Vol. 1.

128. *Crystallographic orientation and electrochemical activity of AZ31 Mg alloy.* Song, Guang-Ling, Mishra, Raja and Xu, ZhenQing. s.l. : Electrochemistry Communications, 2010, pp. 1009-1012.

129. Chiang, Yet Ming, Birnie, Dunbar and Kingery, David. *Physical ceramics principles for ceramic science and engineering.* s.l. : John Wiley & Sons, Inc., 1997.

130. *A thermdynamic theory of dissolution potential and further tests of the theory.* Rastogi, R. P. and Kahn, S. A. s.l. : Journal of electrochemistry society: Electrochemical science and technology, 1980, Vol. 127.

131. *L'utilisasion du magnesium comme material perdu dans l'osteosynthese.* A, Lambotte. s.l. : Bull Mem Soc Nat Chir, 1932, Vol. 28, pp. 1325-1334.

132. *Trend in biomedical engineering: focus on Smart Bio-materials and Drug Delivery.* Tanzi, Maria Cristina, et al. s.l. : Journal of Applied Biomaterials Biomechanic, 2011, Vol. 9, pp. 87-97. 2.

133. *Effect of impurities and electrolyte thickness on degradation of pure magnesium:A finite element study.* Montoya, R., Escudero, M. L. and Garcia-Alonso, M. C. s.l. : Materials Science and Engineering B, 2011, Vol. 176, pp. 1807-1811.

134. *Absorbable metal in bone surgery.* McBride, Earl D. Oklahama city : Journal of the American Medical Association, 1938, pp. 2464-2467.

135. *Update on bioabsorbable stents: From bench to clinical.* Waksman, R. s.l. : Journal compilation.

136. *Temporary scaffolding of coronary arteries with bioabsorbable magnesium stents: a prospective, non-randomised multicentre trail.* Erbel, Raimund, et al. Essen : The lancet, 2007, Vol. 369, pp. 1869-1875.

137. *Biocorrosion of magnesium alloys: a new principle in cardiovascular implant technology?* Heublein, B, et al. s.l. : Heart, 2003, Vol. 89, pp. 651-656.

138. *Environmentall behavior of magnesium and magnesium alloys.* Alves, H., et al. 2, s.l. : Materials Technology, 2001, Vol. 16, pp. 110-126.

139. *American Society for metals, Binary Alloy Phase Diagram.* Metals Park, OH : American Society for Metals, 1986. p. 130. Vol. 1.

140. *Teh corrosion of magnesium in aqueous solution containing chloride ions.* Tunold, R., et al. s.l. : Corrosion Science, 1977, Vol. 17, p. 353.

141. *The negative difference effect and unipositive Mg^+.* Atrens, Andrej and Wolfgang, Dietzel. 4, s.l. : Advanced engineering materials, 2007, Vol. 9, pp. 292-297.

142. *Kinetics and mechanism of the magnesium electrode reaction in molten magnesium chloride.* Kisza, A., et al. s.l. : Journal of applied electrochemistry, 1995, Vol. 25, pp. 940-946.

143. *Research activities of biomedical magnesium alloys in china.* Zheng, Yufeng and Gu, Xuenam. 4, s.l. : Biomedical Applications of Magnesium, 2011, Vol. 63, pp. 105-108.

144. *PHB, crystalline and amorphous magnesium alloys: Promising candidates for bioresorbable osteosynthesis implants?* Celarek, Anna, et al. s.l. : Materials Science and Engineering C, 2012, Vol. 32, pp. 1503-1510.

145. *Ultrafine-grained surface layer on Mg_Al_Zn alloy produced by cryogenic burnishing for enhanced corrosion resistance.* Pu, Z., et al. s.l. : Scripta Materialia, 2011 йил, Vol. 65, pp. 520-523.

146. Zhang, E., Chu, P. K. and Liu, X. *Biomaterials and surface modification.* Kerala : Research signpost, 2007. p. 27.

147. Helsen, J. A. and Breme, H. J. *Metals as biomaterials.* s.l. : John Wiley & sons, 1998. p. 23.

148. *In vitro and in vivo corrosion measurements of magnesium alloys.* Witte, Frank, et al. s.l. : Biomaterials, 2006, Vol. 27, pp. 1013-1018.

149. Hans, Seiler and Sigel, G. *Handbook on toxicity of inorganic compound.* s.l. : Maecel Dekker Inc, 1988.

150. *In vitro and in vivo studies on a Mg-Sr binary alloy system developed as a new kind of biodegradable metal.* Gu, X. N., et al. s.l. : Acta Biomaterialia, 2012, Vol. 8, pp. 2360-2374.

151. *Biological evaluation of medical devices part 5: tests for cytotoxicity: in vitro methods.* Arlington, VA: ANSI/AAMI : International organization for standardaziation. ISO-10993-5, 1999.

152. *Cytotoxicity evaluation of 43 metal salts using murine fibroblasts and osteoblastic cells.* Yamamoto, A., Honma, R. and Sumita, M. 2, s.l. : Journal of biomedical materials research, 1998, Vol. 39.

153. *Magnesium alloys as implant materials - Principles of property design for Mg-RE alloys.* Hort, N., et al. s.l. : Acta biomaterialia, 2010, Vol. 6, pp. 1714-1725.

154. *Improved mechanical performance and delayed corrosion phenomena in biodegradable Mg-Zn-Ca alloys through Pd-alloying.* Gonzalez, S., et al. s.l. : Journal of the mechanical behavior of biomedical materials, 2012, Vol. 6, pp. 53-62.

155. *Comparative study on corrosion behaviour of pure Mg and WE43 alloy in static, stirring and flowing Hank's solution.* Li, N., et al. s.l. : Corrosion engineering, Science and technology, 202, Vol. 47, pp. 346-351.

156. *In vivo corrosion and corrosion protection of magnsium alloy LAE442.* Witte, F., et al. s.l. : Acta biomaterialia, 2010, Vol. 6, pp. 1792-1799.

157. *Biodegradation and biocompatibility of PLA and PLGA microspheres.* Anderson, James M. and Shive, Mattew S. s.l. : Advanced drug delivery reviews, 2012, Vol. 64, pp. 72-82.

158. *Corrosion of magnesium and its alloys.* Liu, L. J. and Schlesinger, M. s.l. : Corrosion science, 2009, Vol. 51, pp. 1733-1737.

159. *Validated numerical modeling of galvanic corrosion for couple: Magnesium alloy (AEE44)-mild steel and AE44-aluminum alloy (AA6063) in braine solution.* Deshpande, Kiran B. s.l. : Corrosion Science, 2010, Vol. 52, pp. 3514-3522.

160. *Galvanic corrosion of magnesium alloy AZ91D in contact with an aluminium alloy, steel and zinc.* Song, Guangling, et al. s.l. : Corrosion Science, 2004, Vol. 46, pp. 955-977.

161. *DFT study on surface properties and dissolution trends of Al (100) surfaces doped with Zn, Ga, In, Sn and Pb.* Liu, Jiancai, et al. s.l. : Apploed surface science, 2011, Vol. 257, pp. 4004-4009.

162. *Accurate and simple density for the electronic exchange energy: Generalized gradient approximation.* Perdew, John P. and Yue, Wang. 12, 1986, Vol. 33.